# Time-dependent density functional theory for extremely nonlinear interactions of light with dielectrics

Shunsuke A. Sato
Doctoral Program in Physics

Submitted to the Graduate School of
Pure and Applied Sciences
in Partial Fulfillment of the Requirements
for the Degree of Doctor of Philosophy in
Science

at the
University of Tsukuba

# Abstract

Interactions of intense ultra-short laser pulses with solids have been attracting much interest from both fundamental and technological points of view. The laser pulses induce nonlinear electron dynamics in solids, and can be employed to control material properties such as optical and magnetic properties, in a femtosecond time scale. Once the intensity of the laser pulses exceeds a critical threshold of materials, the pulses bring an irreversible change to the materials. The irreversible change induced by ultra-short laser pulses can be used for non-thermal laser-processing.

We have developed theoretical methods based on the time-dependent density functional theory (TDDFT) in order to study nonlinear interactions of light with solids. They provide first-principles descriptions for laser-solid interactions in two different schemes. One is to explore electron dynamics in a unit cell of crystalline solids under given external electric fields. We call it the *single-cell* simulation. The other is to investigate coupled dynamics of electrons in solids and macroscopic electromagnetic fields, where feedback from the electron dynamics to the fields is treated consistently. We call it the *multi-scale* simulation. The single-cell simulation is suitable to investigate the microscopic mechanism of laser-induced nonlinear phenomena in a femtosecond time scale. The multi-scale simulation is suitable to investigate propagation effects of laser pulses and spatial distribution of electronic excitation in a micrometer scale.

In order to improve accuracy and reliability of the above simulations, we have developed theoretical and numerical methods to calculate electron dynamics based on the TDDFT employing a modern exchange-correlation potential that well reproduces optical band gap of dielectrics; a meta generalized gradient approximation (meta-GGA) proposed by Tran and Blaha [Phys. Rev. Lett. 102, 226401 (2009)]. The optical band gap is a crucial quantity to quantitatively investigate nonlinear electron dynamics induced by intense laser pulses since it is directly related to the order of perturbation that permits electronic excitations in the multi-photon picture. We have found that it is indispensable to adopt the predictor-corrector procedure for a stable time evolution when the meta-GGA potential is employed in the simulations. We have developed a method to evaluate electronic excitation energy without referring to the energy functional which is unknown for the meta-GGA potential. Thanks to the improvement of accuracy and reliability of the simulations, one may quantitatively investigate interactions of light with dielectrics in both linear and nonlinear regimes.

We have developed a computational code by ourselves to conduct the above simulations pragmatically. The name of the code is *Ab-initio Real-Time Electron Dynamics simulator; ARTED*. In ARTED, parallel computing has been implemented with the Message Passing Interface (MPI) and OpenMP. Therefore, ARTED can be used with both the Flat-MPI and the MPI+OpenMP hybrid parallelization. The multi-scale simulation requires a huge amount of computational cost since it consists of a large number of simulations for electron dynamics. Thus, it is necessary to use large-scale supercomputers like the K computer at RIKEN in order to conduct the multi-scale simulation. We have optimized ARTED for massively parallel computing to employ the large-scale supercomputers.

It shows good parallel efficiency and effective performance, even if several tens of thousands of cores are employed for parallel computing.

Modulation of optical properties of materials induced by intense ultra-short laser pulses is an important subject of light science and has been extensively studied in recent experiments. We have applied the single-cell simulation to investigate optical properties of dielectrics under intense ultra-short laser pulses. Immediately after intense laser irradiation, only electrons are excited, while atoms locate at their positions in the ground state because of their slow motion. We call it the electronic non-equilibrium phase. After some tens of femtosecond, electrons are thermalized and become hot-carriers, while lattice stays in much lower temperature. We call this phase the electronic thermal-equilibrium phase. To investigate optical properties of the electronic non-equilibrium phase, we have developed *numerical pump-probe experiments* in which *experimental* pump-probe technique is mimicked by the simulation. To investigate the electronic thermal-equilibrium phase, we employed a linear response calculation for the finite electron-temperature system described with Fermi-Dirac function for electronic occupation factors. We have calculated dielectric functions by employing these two methods and have found that the laser-excited dielectrics show a metallic response in the both phases. We also found that the imaginary part of the dielectric function shows complex behaviors. The imaginary part in the non-equilibrium phase shows negative components at several frequencies, reflecting the non-equilibrium distribution of excited electrons. On the other hand, the imaginary part in the electronically thermalized phase does not show the negative component, and can be well described by a Drude-like model. By the Drude model analysis, we have found that the Drude damping time of hot-carriers depends on the electron temperature. The damping time can be short (about 1fs), which is shorter than the time-scale of electron-electron and electron-phonon collisions (several tens of fs to several ps). The short damping time could be caused by elastic scattering from ions.

Intense laser pulses induce an irreversible change in materials if the intensity of the laser pulses exceeds a critical threshold. If the intensity is close to but below the threshold, induced phenomena would be extremely nonlinear as well as reversible. We have applied the multi-scale simulation to investigate such reversible nonlinear phenomena and compared the simulation results with recent experimental ones. The multi-scale simulation enables us to directly investigate properties of propagated laser pulses through micrometer-scale samples. We have applied it to simulate femtosecond laser irradiation on a thin $SiO_2$ ($\alpha$-quartz) film for various laser intensities and obtained transmitted pulses from the thin film. The transmitted laser pulses from the sample have also been measured in experiments. We have found good agreement between the theoretical and the experimental transmitted laser pulses. Furthermore, we have evaluated nonlinear polarization and energy transfer in the sample as functions of time. It is also possible to experimentally extract the nonlinear polarization and the energy transfer under some assumptions. We found that our theoretical results show good agreement with experimental ones. Therefore, the assumptions in the experimental extractions have been validated. We have further investigated the origin of the nonlinear polarization in $SiO_2$ based on microscopic electron dynamics and found that the nonlinear polarization mainly comes from the electronic motion around oxygen atoms.

Femtosecond laser pulses whose intensity exceeds the critical threshold bring an irreversible change to materials through a non-equilibrium phase where the electron temperature is much higher than the lattice temperature. This irreversible change can be applied to the non-thermal laser-processing and has attracted much attention in recent years. We have applied the multi-scale simulation to investigate the initial process of non-thermal laser-processing and estimated damage threshold and ablation depth. First, we have simulated fs-laser irradiation on a $SiO_2$ ($\alpha$-quartz) surface and evaluated the spatial

distribution of transferred energy from the laser pulse to the solid. We have employed the laser pulse whose mean photon energy is 1.55 eV in the simulation. Since the optical gap of $\alpha$-quartz is about 9 eV, there is no energy transfer for the weak laser pulse. Once the intensity of the laser pulse becomes sufficiently strong, energy transfer can take place because of nonlinear light-matter interactions such as multi-photon and tunneling excitation processes. We have found that a large amount of energy is deposited near the surface when the intensity of the laser pulse is strong. Then, we have estimated the damage and ablation thresholds and the ablation depth by comparing the transferred energy distribution with melting and cohesive energies of $\alpha$-quartz. The estimated damage threshold shows the reasonable agreement with the experimental results. Also, the ablation depth fairly reproduces the experimental one. However, the ablation threshold is higher than the experiment results, suggesting a nonthermal mechanism for the surface ablation.

In conclusion, we have developed theoretical and numerical methods as well as a computational code to investigate interactions of highly-intense ultra-short laser pulses with solids based on the TDDFT in the time domain. We have developed methods to employ the modern exchange-correlation potential in the TDDFT simulation in order to improve accuracy and reliability of the theoretical investigation. Then, we have parallelized the computational code with MPI and OpenMP for the hybrid parallel computing and optimized it for the massively parallel computing. We have applied the TDDFT simulation to study optical properties of dielectrics after intense ultra-short laser irradiation in the electronic non-equilibrium phase and the electronic thermalized phase. We have also investigated nonlinear polarization and energy transfer in dielectrics in the time domain. Finally, we have applied the TDDFT simulation to investigate the femtosecond-laser-induced laser-damage-phenomena from a first-principles level. Our theoretical results for the above phenomena show good agreement with recent experimental data, and microscopic understanding of these phenomena has been grown.

# Contents

# List of Figures

# List of Tables

# Chapter 1

# Introduction

## 1.1 Ultrafast intense laser science

The interaction of light with matter is one of the most important subjects in current sciences and technologies from both fundamental and applicational points of view. By a curious coincidence, the year 2015, when I am writing this thesis, has been proclaimed as the International Year of Light and Light-based Technologies (IYL 2015) by United Nations [1]. In the resolution of the IYL 2015 [1], "the importance of light and light-based technologies in the lives of the citizens of the world and for the future development of global society on many levels" has been recognized. Indeed, our lives have been benefitting from many applications of light-based technologies such as light emitting diode (LED) [2,3], solar cell [4,5], X-ray photography [6], etc.

In the recent optical science, laser technologies have been rapidly developing and have enabled us to observe novel phenomena and even to control properties of materials. Especially, two directions of the developments have been remarkable. One is to generate high-intensity laser pulses, and the other is to generate ultra-short laser pulses. The high-intensity laser pulses can be employed to induce nonlinear phenomena in materials, and the ultra-short laser pulses can be employed to observe ultrafast phenomena and even to control ultrafast motion of electrons and nuclei.

Figure 1.1 shows the maximum laser intensity available at each year. The available intensities of laser pulses have been rapidly increasing. Nowadays, laser pulses of $10^{22}$ W/cm$^2$ as the maximum focused intensity have been available [7–9]. Intense laser pulses can induce nonlinear phenomena in materials. Nonlinear optical phenomena have been observed for the first time by Franken, *et al*, in 1961 [10]. They have measured the second order optical harmonics. Since the first observation of nonlinear optical phenomena, nonlinear optics has been tremendously developed [11–14]. In the conventional nonlinear optics, nonlinear responses of electrons for intense laser fields are treated by using perturbative expansions in terms of strength of the laser fields: A linear response of electrons is described by a dielectric function or a linear susceptibility, while the second, the third and higher orders nonlinear electronic responses are described by corresponding nonlinear susceptibilities. For example, the above second-harmonic generation is related to the second-order susceptibility. The third-order susceptibility characterizes the optical Kerr effect, which is modulation of refractive index induced by optical electric fields. Nowadays, the optical Kerr effect is widely used in many optical devices [11,14].

Once field strength of laser pulses becomes close to the strength of the force acting on electrons in materials, the nonlinearity of electron dynamics grows larger. In such a strongly nonlinear regime, the
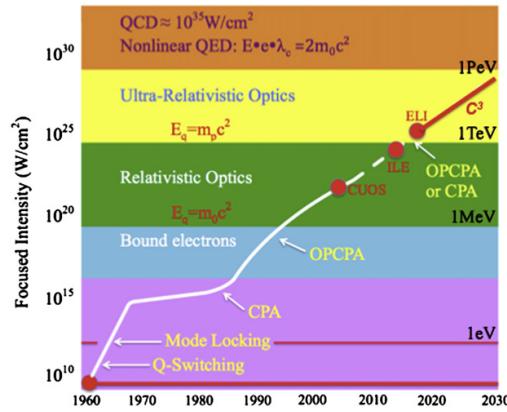
Figure 1.1: Evolution of laser intensity. This figure is taken from reference [15].

perturbative expansion for the nonlinear responses becomes difficult and sometimes even impossible. In order to describe the extremely nonlinear phenomena, nonlinear electron dynamics in materials must be directly/explicitly treated without any perturbative expansions. One of the most important phenomena in this strongly (non-perturbative) nonlinear regime is the high-order harmonic generation (HHG) from atoms [16–19]. Experimentally, generation of harmonics of more than 100th-order has been observed [20, 21]. The microscopic mechanism of the HHG from atoms has been established based on semi-classical [22–24] and quantum mechanical [25] models. The HHG is an important phenomenon not only from a fundamental point of view but also a technological point of view. The HHG from atoms has drastically developed the technology to generate ultra-short laser pulses [26, 27]. Very recently, the HHG from solids has been observed in several experiments [28–30] and has been attracting much interest to develop future laser technologies. However, the microscopic mechanism of the HHG from solids is still under discussion [31–34].

One important application of high-intensity laser pulses is the laser-processing. Extremely intense laser pulses have potential ability to bring an irreversible change to materials. Thus, attempts to process materials with such intense laser pulses have been extensively investigated [35–37]. Nowadays, the laser-processing is one of the important technique of material machining in industry. In the current frontier of the laser-processing technique, formation of periodic structure [38–40] and *non-thermal laser-processing* [36, 41], which will be described later, have been intensively studied. Furthermore, application to the optical memory has also been attracting much interest [42, 43].

Various phenomena in various time-scales have been studied in optical science. Figure 1.2 shows several phenomena in different time-scales. The time scale of atomic motions in molecules and solids, such as molecular vibration and phonons, is typically a hundred femtoseconds. The motion of valence-electron is a femtosecond time-scale while that of core-electron is an attosecond time-scale. For example, the period of electron motion in the Bohr orbital in a hydrogen atom is 152 attoseconds. In nuclei, the motion of nucleons is a zeptosecond time-scale. Generally speaking, spatially small phenomena have shorter time-scales.

Ultrashort light pulses enable us to observe various phenomena in real-time with the pump-probe technique, where two pulses are employed: One is the *pump* pulse to drive dynamics, and the other is the *probe* pulse to observe the driven dynamics. The first pump-probe experiment has been conducted by Toepler in 1864 [44]. He has visualized shock waves for the first time by the pump-probe technique.
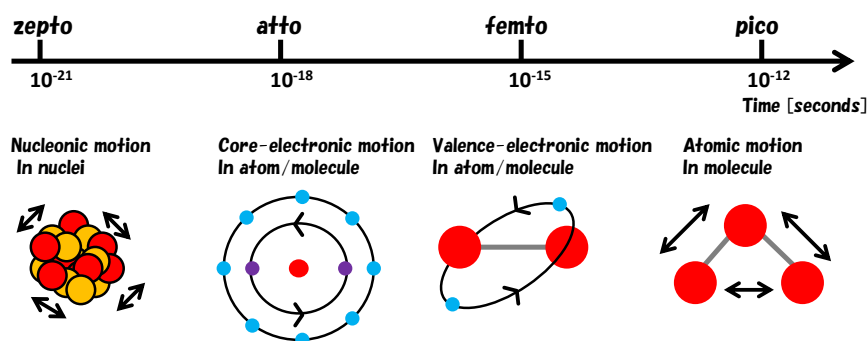
Figure 1.2: Time scales of various phenomena. Atomic motion is a sub-picosecond time-scale phenomenon, motions of electrons are femtosecond and attosecond, and motion of nucleon in nuclei is a zeptosecond.

Figure 1.3 shows the evolution of technologies for the real-time observation. As seen from the figure, the technology of real-time observation has been rapidly developing in the last few decades. In the end of the twentieth century, the real-time observation of atomic motions in molecules by the femtosecond spectroscopy has been drastically developed [45–48]. The pioneer of the field, Ahmed Zewail, has received the Novel Prize in Chemistry 1999.

At the current frontier of generation of ultrashort laser pulses, a 67 attosecond laser pulse is available [49]. This frontier is known as the attosecond science [27,50,51]. Since the electron dynamics in materials is a femtosecond time-scale, the attosecond laser pulses have enough resolution to observe electron dynamics in real-time. Recently, several experiments of the real-time observation of electron dynamics have been reported [52,53].

Thanks to these developments to generate both high-intensity and ultrashort laser pulses, it has been possible to employ laser pulses whose intensity is around $10^{13}$-$10^{15}$ W/cm$^2$ and whose pulse-width is around 10 femtoseconds. We shall call this kind of pulses *high-intensity ultrashort laser pulses*. The field strength of the laser pulses is close to the attracting force on electrons in materials, and the pulse length is comparable to the time scale of the electron dynamics. Thus, the high-intensity ultrashort laser pulses are suitable to control the motion of electrons in materials. Interactions of high-intensity ultrashort laser pulses with solids have been attracting much interest from fundamental and technological points of view [11,35,37,41,54].

If the intensity of a laser pulse exceeds a critical threshold of materials, irreversible phenomena are induced and permanent structural modification can be left on materials. As mentioned above, this kind of phenomena can be applied to the laser-processing. The energy transfer from laser-excited electrons to lattice systems is a picosecond time-scale phenomenon. Therefore, if an intense femtosecond laser pulse is irradiated on solids, the laser pulse goes away before the energy transfer from excited electronic systems to lattice systems and creates a nonequilibrium phase where the electron temperature is much higher than the lattice temperature. If the transferred energy from femtosecond laser pulses to solids is large enough, the permanent structural modification is induced through the nonequilibrium phase. This can be applied to *non-thermal laser-processing*. Figure 1.4 shows a material surface after intense
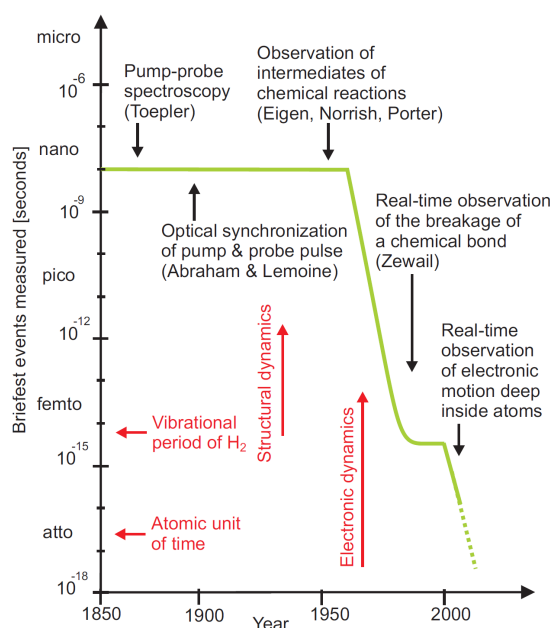
Figure 1.3: Evolution of technology for the real-time observation. This figure is taken from reference [27].

laser irradiation as an example of the non-thermal laser-processing. The panel (a) shows a permanent irreversible structure modification, which is called *laser damage*, induced by an intense laser pulse. If the intensity of laser pulses is much higher than the damage threshold of materials, atoms can be removed from the material surface. This phenomenon is called *laser ablation*. The panel (b) shows a crater created by the laser ablation. As seen from the both panels, the structures created by the intense laser pulses are a micrometer scale. It would be possible to finely machine the material by the non-thermal laser-processing. The non-thermal laser-processing has been attracting much interest as a novel processing technique for future applications, and its microscopic mechanism has been intensively investigated.

If the laser intensity is close to but slightly below the damage thresholds, extremely-nonlinear ultrafast phenomena may be induced in materials without the permanent damage. In such conditions, the materials return to the original state after the laser field ends. These phenomena have potential to provide novel mechanism for future applications of optoelectronic devices since the phenomena may be repeatedly induced without any damage. For example, the high-intensity ultrashort laser pulses can induce ultrafast charge-transfer even in insulators through the nonlinear light-matter interactions [56]. In this reversible regime, the ultrafast nonlinear phenomena can be observed in real-time by the pump-probe technique since the phenomena are reversible and the repeated measurements are applicable. Indeed, by employing the pump-probe technique with intense femtosecond pump-pulses and attosecond probe-pulses, ultrafast phenomena in femtosecond time scale such as modulation of optical properties [53] and band-gap dynamics [57] have been observed in real-time.
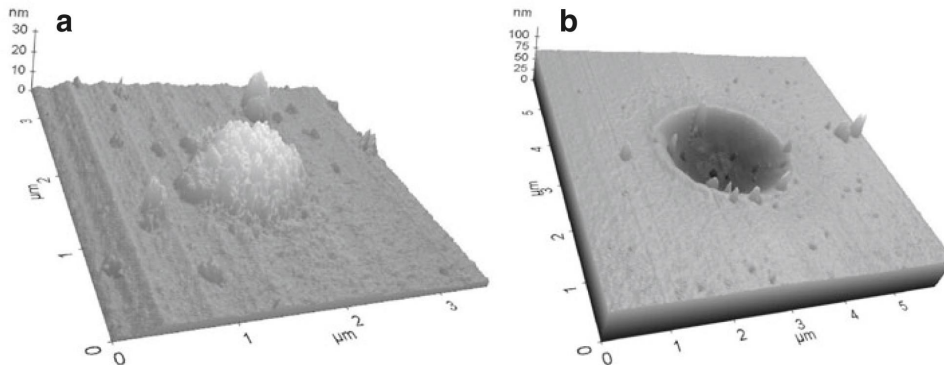
Figure 1.4: Example of laser-processing. This figure is taken from reference [55]. Both panels show the material surface after laser irradiation. The panel (a) shows an irreversible structure modification caused by an intense laser pulse. The panel (b) shows a crater created by a more intense laser pulse.

## 1.2 First-principles theories for light-matter interactions

Theoretical description of electronic structure and electron dynamics in materials is necessary to understand interactions of light with matter since the electron dynamics is induced as the initial process of the light-matter interactions. The description of electronic systems in the matter can be categorized in the many-body problem of quantum systems, which is one of the most important fundamental problems in the theoretical physics. In principle, one can describe such quantum many-body systems by solving the Schrödinger equation, which provides complete descriptions for quantum systems in the non-relativistic limit. However, in practice, it is impossible to directly/explicitly solve the Schrödinger equation for many-electron systems except a few simple systems since its dimension can be easily too huge to solve. Therefore, various methods to treat quantum many-body systems have been developed for a long period: For static problems, the Hartree-Fick method, the configuration interaction method, the coupled-cluster method [58], the $GW$ method [59, 60], etc. have been developed. For time-dependent problems or excitation properties, the time-dependent Hartree-Fock (TDHF), the multi-configuration TDHF [61, 62], the time-dependent complete-active-space self-consistent-field [63], the $GW$ plus Bethe-Salpeter equation approach [64, 65], etc. have been developed.

One of the most successful methods to describe the ground state of quantum many-body systems is the density functional theory (DFT), which have been proposed by Hohenberg and Kohn in 1964 [66]. They have proven two theorems: One is about the one-to-one correspondence between an external potential and the electron density of the ground state under the potential. The other is about a variational principle for the ground state energy based on electron density. Thanks to these theorems, one may investigate properties of the ground state of quantum many-electron systems based on the electron density without referring to the many-body wavefunction. Kohn and Sham have proposed a scheme in order to apply the DFT to practical problems in 1965 [67]. It is known as the Kohn-Sham scheme. In the Kohn-Sham scheme, single-particle Schrödinger-like equations are solved in order to obtain the ground-state energy and the ground-state electron density of many-electron systems. Therefore, thanks to the DFT with the Kohn-Sham scheme, quantum many-body problems for the ground state can be reduced to a quantum one-body problem, and quantum many-body systems such as atoms, molecules, clusters and solids can be theoretically investigated from the first-principles level

with moderate computational costs. The founder of the DFT, Walter Kohn, has received the Novel Prize in Chemistry 1998 with John A. Pople. Nowadays, the DFT has been employed in various fields such as physics, chemistry, device [68–70], bioscience [71, 72], and energy & environmental sciences [73–75].

The DFT is applicable only to the ground state of quantum many-body systems. Therefore, an alternative theory is required to investigate quantum electron dynamics induced by light. Runge and Gross have formulated the time-dependent density functional theory (TDDFT), which is an extension of the DFT so as to describe time-dependent quantum systems and excited states in 1984 [76]. They have proven the one-to-one correspondence between a time-dependent external potential and the time-dependent electron density under the potential and derived the time-dependent Kohn-Sham equation, which is similar to a single-particle time-dependent Schrödinger equation. In order to apply the TDDFT to practical problems, a single-particle potential in the time-dependent Kohn-Sham equation, which is called an exchange-correlation potential, has to be approximated since the *exact* exchange-correlation potential is not known. The quality of the TDDFT calculation depends on approximations to the exchange-correlation potential. The approximations have been extensively studied, and the quality of the TDDFT calculation has been drastically improved [77–81]. Nowadays, the TDDFT is one of the standard methods to investigate excitation properties of materials such as oscillator strength of molecules and dielectric function of solids.

To investigate the reaction of materials to external fields based on the TDDFT, several approaches have been formulated with perturbative expansions for the fields in the frequency domain [82, 83]; Sternheimer method [84–87] and Cashida method [88]. Although these perturbative methods in the frequency domain have been succeeded to investigate the linear and low-order nonlinear properties of materials, they have difficulty to study strongly nonlinear responses such as electron dynamics induced by an intense ultrashort laser pulse since a large number of perturbative expansions could be required. As for extremely (non-perturbatively) nonlinear dynamics, the perturbative expansions in the frequency domain are no more applicable.

One strong point of the TDDFT is its applicability to describe electron dynamics in the time domain for three-dimensional realistic systems with moderate computational costs. We shall call it the *real-time* simulation. In the real-time simulation, the quantum dynamics is described by solving equations of motion for *effective/virtual* single-particle orbitals in the time domain without any perturbative expansions. Therefore, the real-time simulation is applicable to dynamics under both weak and strong fields, and it is a unique choice to investigate nonlinear electron dynamics induced by intense ultrashort laser pulses. Moreover, this kind of methods is useful to simulate experiments that are conducted in the time domain since the simulation provides physical quantities in the time domain and intelligible insights of microscopic electron dynamics. Up to here, we discussed the real-time simulation for electron dynamics in materials. However, the real-time simulation is also applicable to other kinds of quantum dynamics as well as electron dynamics. For example, one can apply the real-time simulation to a motion of nucleons in nuclei.

Historically, early stages of the real-time simulation of quantum systems have been developed in nuclear physics. Bonche, Koonin and Negele have applied the TDHF method to reaction phenomena of nuclear systems for the first time, solving the TDHF equations in the time domain in 1976 [89]. Then Flocard, Koonin and Weiss have applied the method to realistic three-dimensional systems in 1978 [90]. Figure 1.5 shows snapshots of $^{16}$O and $^{16}$O collision in the three-dimensional TDHF calculation. As seen from the figure, the nuclei are fused after the collision.

Yabana and Bertsch have applied the real-time simulation to electronic systems for the first time
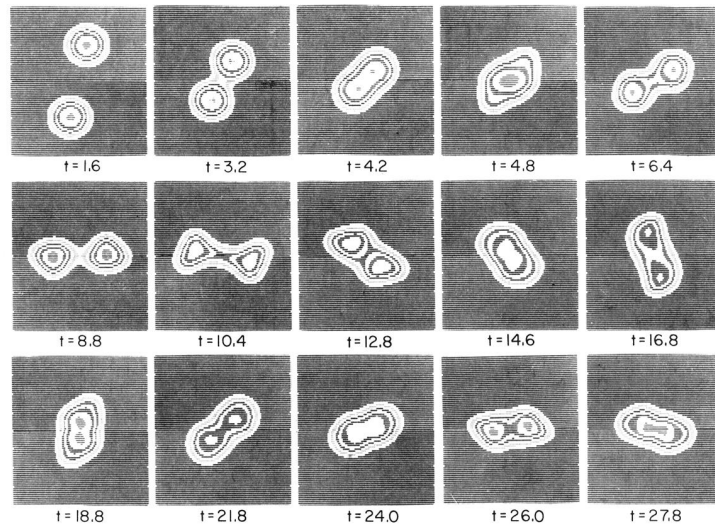
Figure 1.5: Example of real-time time-dependent Hartree-Fock calculation for nuclear collision. This figure is taken from reference [90]. This figure shows an $^{16}$O and $^{16}$O collision.

in 1996 [91]. They have examined optical responses of metallic clusters and the $C_{60}$ molecule in both time and frequency domains. In consequence, nonlinear interactions of intense ultrashort laser pulses with isolated systems such as atoms, molecules and clusters have been widely investigated by the real-time simulation [92,93,93–95]. Bertsch, *et al*, have extended the real-time TDDFT simulation so as to apply it to solid-state systems in 2000 [96]. Then, they have applied the method to nonlinear phenomena in solids induced by intense ultrashort laser pulses such as dielectric breakdown [97] and coherent phonon generation [98,99]. Figure 1.6 shows an example of electron dynamics in crystalline silicon under an high-intensity ultrashort laser pulse. The system is in the ground state at $t = 0.0$ fs. Then, the electron dynamics is induced by the laser field. One may see that chemical bonds, which are red color regions in the ground state, oscillate during the laser irradiation (see $t = 2.1$, 3.5 and 5.0 fs). After the laser irradiation, the chemical bonds are broken due to the strong electronic excitation (see $t = 6.2$ and 8.1 fs). The real-time TDDFT simulation for solids provides microscopic insight of nonlinear electron dynamics in a nanometer spatial-scale and a femtosecond time-scale. Yabana, *et al*, have further developed the real-time TDDFT simulation by coupling with the macroscopic Maxwell's equation in order to describe propagation effects of macroscopic electromagnetic fields in 2012 [100].

## 1.3 Aim of this work

In this work, we theoretically study the interactions of high-intensity ultrashort laser pulses with dielectrics based on the time-dependent density functional theory (TDDFT). Especially, we focus on three topics; (a) optical properties of highly laser-excited dielectrics, (b) nonlinear polarization induced by high-intensity ultrashort laser pulses in the time domain, and (c) initial stage of the non-thermal laser processing.

(a) Optical properties of highly laser-excited dielectrics: An intense laser pulse brings a change
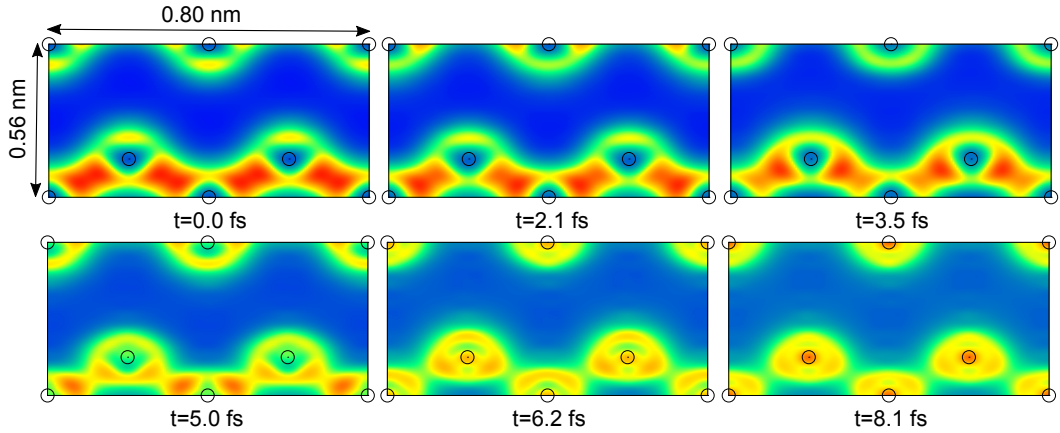
Figure 1.6: Example of real-time TDDFT simulation for electron dynamics in silicon induced by a high-intensity ultrashort laser pulse. Red shows high electron density region and blue shows low electron density region.

of the optical properties in laser-excited dielectrics after the laser-solid interaction. The change has been extensively investigated by many experiments [53,101,102]. Highly laser-excited dielectrics show metallic behavior since electron-hole pairs induced by the laser pulses behave as free-carriers. Therefore, the Drude model, which is a free-carrier model, has been often employed to investigate and to extract the properties of laser-excited solids. One of the aims of this work is to clarify the adequacy and the accuracy of the Drude analysis for laser-excited dielectrics based on the real TDDFT simulation. We expect that this theoretical study will support the validity of the Drude analysis and clarify the limitation of the analysis. Furthermore, we expect to find new features of laser-excited dielectrics beyond those of the Drude model.

(b) Nonlinear polarization induced by high-intensity ultrashort laser pulses in the time domain: High-intensity ultra-short laser pulses may induce extremely nonlinear phenomena without any permanent damage on materials if the intensity is close to but slightly below the damage threshold. To understand the nonlinear light-matter interactions, one of the most fundamental quantities is the nonlinear polarization. One of the aims of this work is to investigate the nonlinear polarization induced by the extremely nonlinear light-matter interactions in the reversible regime and to clarify the microscopic origin of the nonlinear polarization. For this purpose, we apply the TDDFT to simulate femtosecond laser irradiation on a thin $SiO_2$ ($\alpha$-quartz) film for various laser intensities. We will evaluate the nonlinear polarization and the energy transfer from the laser to the solid in the time domain and then compare the simulated results with recent experimental data. We will investigate the induced electron dynamics in a nanometer scale to elucidate the microscopic mechanism of the nonlinear polarization.

(c) Initial stage of the non-thermal laser processing: If a femtosecond laser pulse whose intensity exceeds the critical threshold, the laser pulse brings an irreversible change to materials through the nonequilibrium phase. This can be applied to the non-thermal laser processing. So far, most theoretical investigations of the laser-processing phenomena have relied on phenomenological models with empirical parameters, especially for energy transfer from laser pulses to materials. One of the aims of this work is to investigate the initial stage of the non-thermal laser-processing based on the first-

principles theoretical framework, the TDDFT, without any empirical parameters. We will simulate fs-laser irradiation on a $SiO_2$ ($\alpha$-quartz) surface and evaluate the spatial distribution of transferred energy from the laser pulse to the sample. We expect that the spatial distribution of the transferred energy is useful to predict the damage threshold and the ablation depth. We will compare the theoretical results with experimental data and develop a microscopic understanding of the phenomena.

In the real-time TDDFT simulations for solids, the adiabatic local density approximation (LDA) has only been employed so far. The adiabatic LDA sometimes causes severe problems: optical gaps of various materials are substantially underestimated by the approximation. Due to the underestimation, quantitative investigations based on the real-time TDDFT simulation with the adiabatic LDA is difficult. Sometimes, it provides even qualitatively wrong results. In order to quantitatively investigate the above three topics (a-c), we develop theoretical and numerical methods to employ a modern exchange-correlation potential beyond the LDA in the real-time TDDFT simulation. We employ a meta generalized gradient approximation (meta-GGA) potential proposed by Tran and Blaha [103] to overcome the optical gap problem.

We develop a computational code by ourselves to practically conduct the above simulations. The name of the code is *Ab-initio Real-Time Electron Dynamics simulator; ARTED*. The real-time TDDFT simulations are computationally demanding. Sometimes, it is necessary to employ massively-parallel supercomputers like the K computer at RIKEN. Therefore, we parallelize and optimize ARTED for massively parallel supercomputing.

The construction of the thesis is as follows. In Chap. 2, we describe the theoretical frameworks of the DFT and the TDDFT used in this study. In Chap. 3, we show the numerical aspects of this work including numerical implementation, parallelization and computing performance of our code. In Chap. 4, we develop methods to employ the modern exchange-correlation potential in the TDDFT simulations in the time domain and illustrate the electron dynamics calculations within both linear and nonlinear regimes. In Chap. 5, we investigate the optical properties of highly laser-excited dielectrics. In Chap. 6, we investigate the nonlinear polarization induced by high-intensity ultrashort laser pulses in the time domain. In Chap. 7, we investigate the initial stage of the non-thermal laser processing. Our findings are summarized in Chap. 8.

# Chapter 2

# Theoretical framework

## 2.1 Density functional theory

The density functional theory (DFT) has been a great successful method to describe ground state structure of solids [104, 105]. Nowadays, the DFT has been applied to various problems in vast fields such as physics, chemistry, device [68–70], bioscience [71, 72], and energy & environmental sciences [73–75]. In order to investigate light-matter interactions, we employ the DFT calculation to prepare the initial condition of subsequent calculations for electron dynamics induced by light fields. In this section, we briefly explain the DFT.

### 2.1.1 Hohenberg-Kohn theorems

In the DFT, electron density of ground states $n(\boldsymbol{r})$ is one of the most important physical quantities. Hohenberg and Kohn have proven that electron density of a ground state is related to an external potential with a one-to-one correspondence, which is known as the first Hohenberg-Kohn theorem [66]. Thanks to the theorem, any physical properties can be calculated in principle, once the electron density of the ground state is obtained, because the electron density determines the Hamiltonian of the system.

The proof of the first Hohenberg-Kohn theorem is as follows: First, we introduce a Hamiltonian of an electronic system containing $N$ electrons,

$$\hat{H} = \hat{T} + \hat{V} + \hat{V}_{ee}. \tag{2.1}$$

The kinetic energy operator $\hat{T}$, the external potential operator $\hat{V}$, and the Coulomb interaction operator $\hat{V}_{ee}$ are defined using the field operator $\hat{\psi}_s(\boldsymbol{r})$ as,

$$\hat{T} = \sum_s \int d\boldsymbol{r} \hat{\psi}_s^\dagger(\boldsymbol{r}) \frac{-\nabla^2}{2m} \hat{\psi}_s(\boldsymbol{r}), \tag{2.2}$$

$$\hat{V} = \sum_s \int d\boldsymbol{r} \hat{\psi}_s^\dagger(\boldsymbol{r}) v(\boldsymbol{r}) \hat{\psi}_s(\boldsymbol{r}), \tag{2.3}$$

$$\hat{V}_{ee} = \frac{1}{2} \sum_{ss'} \int d\boldsymbol{r} d\boldsymbol{r}' \hat{\psi}_s^\dagger(\boldsymbol{r}) \hat{\psi}_{s'}^\dagger(\boldsymbol{r}') \frac{e^2}{|\boldsymbol{r} - \boldsymbol{r}'|} \hat{\psi}_{s'}(\boldsymbol{r}') \hat{\psi}_s(\boldsymbol{r}), \tag{2.4}$$

where $v(\boldsymbol{r})$ is an external potential. For the electronic system, once species and positions of atoms are given, the external potential and the Hamiltonian are uniquely determined. In a conventional methodology, one can obtain the ground state of the system by solving the time-independent Schrödinger equation,

$$\hat{H}|\Psi_{GS}\rangle = E_{GS}|\Psi_{GS}\rangle, \tag{2.5}$$

where $|\Psi_{GS}\rangle$ is the ground-state wavefunction of the system and $E_{GS}$ is its energy. By using the field operator $\hat{\psi}_s(\boldsymbol{r})$, the electron density of the ground state is described by $n(\boldsymbol{r}) = \sum_s \langle \Psi_{GS}|\hat{\psi}_s^\dagger(\boldsymbol{r})\psi_s(\boldsymbol{r})|\Psi_{GS}\rangle$. Thus, the external potential uniquely defines the electron density of the ground state, $n(\boldsymbol{r})$, through the Schrödinger equation (2.5).

We next prove that the electron density of the ground state uniquely defines the external potential. Here, we employ contradiction for the proof: We assume existence of two different external potentials $v(\boldsymbol{r})$ and $v'(\boldsymbol{r})$ that give the same electron density $n(\boldsymbol{r})$ in the ground states. These potentials, $v(\boldsymbol{r})$ and $v'(\boldsymbol{r})$, provide the Hamiltonians, $\hat{H}$ and $\hat{H}'$, and the ground states, $|\Psi_{GS}\rangle$ and $|\Psi'_{GS}\rangle$, respectively.

By the variational principles for $\hat{H}$, we obtain the following relation:

$$\begin{aligned}
E_0 &= \langle \Psi_{GS}|\hat{H}|\Psi_{GS}\rangle < \langle \Psi'_{GS}|\hat{H}|\Psi'_{GS}\rangle \\
&= \langle \Psi'_{GS}|\hat{H}'|\Psi'_{GS}\rangle + \langle \Psi'_{GS}|\hat{H} - \hat{H}'|\Psi'_{GS}\rangle \\
&= E'_0 + \int d\boldsymbol{r} n(\boldsymbol{r}) \left[ v(\boldsymbol{r}) - v'(\boldsymbol{r}) \right],
\end{aligned} \tag{2.6}$$

where $E_0$ and $E'_0$ are the ground state energies of each Hamiltonian. Similarly, we also obtain the following relation:

$$\begin{aligned}
E'_0 &= \langle \Psi'_{GS}|\hat{H}'|\Psi'_{GS}\rangle < \langle \Psi_{GS}|\hat{H}'|\Psi_{GS}\rangle \\
&= \langle \Psi_{GS}|\hat{H}|\Psi_{GS}\rangle + \langle \Psi_{GS}|\hat{H}' - \hat{H}|\Psi_{GS}\rangle \\
&= E_0 - \int d\boldsymbol{r} n(\boldsymbol{r}) \left[ v(\boldsymbol{r}) - v'(\boldsymbol{r}) \right].
\end{aligned} \tag{2.7}$$

We thus obtain the following contradiction:

$$E_0 + E'_0 < E_0 + E'_0. \tag{2.8}$$

By the contradiction, two different external potentials that give the same electron density in the ground states cannot exist. Therefore, an external potential and its ground-state electron-density are related with the one-to-one correspondence. As mentioned above, this one-to-one correspondence is known as the first Hohenberg-Kohn theorem.

Thanks to the theorem, we may describe ground-state energy as a functional of electron density,

$$E[n] = T[n] + +V_{ee}[n] + \int d\boldsymbol{r} n(\boldsymbol{r}) v_{ext}(\boldsymbol{r}), \tag{2.9}$$

where $E[n]$ is functional of the total energy, $T[n]$ is that of the kinetic energy, and $V_{ee}[n]$ is that of the electron-electron interaction.

Furthermore, Hohenberg and Kohn have proven the following relation,

$$E_{GS} \leq E[\tilde{n}(\boldsymbol{r})], \tag{2.10}$$

where $\tilde{n}(\boldsymbol{r})$ is arbitrary electron density satisfying $\tilde{n}(\boldsymbol{r}) \geq 0$ and $\int d\boldsymbol{r}\tilde{n}(\boldsymbol{r}) = N$. This relation is known as the second Hohenberg-Kohn theorem [66]. This theorem allows us to investigate the ground state by using the following variational principle,

$$\delta\left\{E[n] - \mu\left[\int d\boldsymbol{r}n(\boldsymbol{r}) - N\right]\right\} = 0. \tag{2.11}$$

## 2.1.2 Kohn-Sham Scheme

In the variational principle of Eq. (2.11), there is no many-body wavefunction needed, but only electron density. Since the dimension of the wavefunction is $3N$ and that of the electron density is only 3, Eq.(2.11) could derive more convenient methods to investigate ground states than the conventional Schrödinger equation for many-body systems.

Kohn and Sham have proposed a useful scheme to evaluate the energy functional $E[n]$, introducing single particle orbitals $\phi_i(\boldsymbol{r})$ of a non-interacting *virtual* system: The single-particle orbitals and the non-interacting system are called Kohn-Sham orbitals and Kohn-Sham system, respectively. The Kohn-Sham orbitals are solutions of the following single-particle Schrödinger-like equation:

$$\left[-\frac{1}{2}\nabla^2 + v_s(\boldsymbol{r})\right]\phi_i(\boldsymbol{r}) = \epsilon_i\phi_i(\boldsymbol{r}), \tag{2.12}$$

where $v_s(\boldsymbol{r})$ is a local potential of the Kohn-Sham system. In this method, the local potential is chosen so that the electron density of the many-body system is reconstructed by the Kohn-Sham orbitals,

$$n(\boldsymbol{r}) = \sum_s \langle\Psi_{GS}|\hat{\psi}_s^\dagger(\boldsymbol{r})\psi_s(\boldsymbol{r})|\Psi_{GS}\rangle = \sum_i |\phi_i(\boldsymbol{r})|^2. \tag{2.13}$$

By using the Kohn-Sham orbitals, we rewrite the energy functional of Eq. (2.9) as follows:

$$E[n] = T_{KS}[n] + \int d\boldsymbol{r}n(\boldsymbol{r})v_{ext}(\boldsymbol{r}) + \frac{1}{2}\int d\boldsymbol{r}d\boldsymbol{r}'\frac{n(\boldsymbol{r})n(\boldsymbol{r}')}{|\boldsymbol{r} - \boldsymbol{r}'|} + E_{xc}[n], \tag{2.14}$$

where the first term $T_{KS}$ is the kinetic energy of the Kohn-Sham system,

$$T_{KS} = \sum_i \int d\boldsymbol{r}\phi_i^*(\boldsymbol{r})\frac{-1}{2}\nabla^2\phi_i(\boldsymbol{r}), \tag{2.15}$$

and the second term is the energy from the external potential. The third term is classical Coulomb energy of electrons, so-called Hartree energy, and the last term $E_{ex}$ is the all other contributions, so-called exchange-correlation energy, defined as

$$E_{xc}[n] = T[n] - T_{KS} + V_{ee}[n] - \frac{1}{2}\int d\boldsymbol{r}d\boldsymbol{r}'\frac{n(\boldsymbol{r})n(\boldsymbol{r}')}{|\boldsymbol{r} - \boldsymbol{r}'|}. \tag{2.16}$$

In order to define the local potential $v_s(\boldsymbol{r})$, we rewrite the variational principle of Eq. (2.11) based on the Kohn-Sham orbitals. First, we introduce the following quantity:

$$L = E[n] - \sum_{i,j}^N \epsilon_{ij}(\int d\boldsymbol{r}\phi_i^*(\boldsymbol{r})\phi_j(\boldsymbol{r}) - \delta_{ij}). \tag{2.17}$$

Then, we apply the variational principle,

$$\frac{\delta L}{\delta \phi_i^*(\boldsymbol{r})} = 0,  \tag{2.18}$$

and obtain the equation of motion for the Kohn-Sham orbitals,

$$\hat{h}_{KS}\phi_i(\boldsymbol{r}) = \sum_j \epsilon_{ij}\phi_j(\boldsymbol{r}),  \tag{2.19}$$

where $\hat{h}_{KS}$ is the Kohn-Sham Hamiltonian defined by

$$\hat{h}_{KS} = -\frac{1}{2}\nabla^2 + v_{ext}(\boldsymbol{r}) + \int d\boldsymbol{r}' \frac{n(\boldsymbol{r}')}{|\boldsymbol{r} - \boldsymbol{r}'|} + \frac{\delta E_{xc}[n]}{\delta n(\boldsymbol{r})}.  \tag{2.20}$$

We can choose the Kohn-Sham orbitals so as to diagonalize the Kohn-Sham Hamiltonian by a unitary transformation and then obtain the following Kohn-Sham equation,

$$\hat{h}_{KS}\phi_i(\boldsymbol{r}) = \epsilon_i\phi_i(\boldsymbol{r}).  \tag{2.21}$$

By comparing Eqs.(2.12) and (2.21), we obtain the following relation for the single particle potential,

$$v_s(\boldsymbol{r}) = v_{ext}(\boldsymbol{r}) + \int d\boldsymbol{r}' \frac{n(\boldsymbol{r}')}{|\boldsymbol{r} - \boldsymbol{r}'|} + \frac{\delta E_{xc}[n]}{\delta n(\boldsymbol{r})},  \tag{2.22}$$

where the first term is the external potential, the second term is the Hartree potential, and the last term is an exchange-correlation potential.

The Kohn-Sham equation (2.21) is similar to the single-particle Schrödinger equation under effective single-particle potential $v_s(\boldsymbol{r})$. Nevertheless, it may give the exact electron density and the total energy of the system, if we employ the *exact* exchange-correlation functional $E_{xc}[n]$. The exact exchange-correlation functional, however, have not been constructed yet for three-dimensional realistic systems. We thus have to approximate exchange-correlation functionals or potentials when we apply the Kohn-Sham equation to practical problems. Many functionals have been developed for various aims so far. In this work, we employ a local density approximation (LDA) [106] for first-principles treatment and a meta generalized gradient approximation (meta-GGA) [103] proposed by Tran and Blaha in order to reproduce energy band gaps of materials. The details of the functionals will be shown in Sec 2.4.

## 2.2 Time dependent density functional theory

We next explain the time-dependent density functional theory (TDDFT), which is an extension of the DFT so as to describe excited states. Although the DFT is a successful method to investigate properties of ground states of materials, it is not applicable to describe electronic excited states and electron dynamics. In order to investigate properties of excited states, Runge and Gross have developed the TDDFT [76].

### 2.2.1 Runge-Gross theorem

While Kohn and Sham have proven the one-to-one correspondence between an external potential and the electron density in the ground state under the potential, Runge and Gross have proven the one-to-one correspondence between a time-dependent external potential and the time-dependent electron density under the potential [76]. This theorem is known as the Runge-Gross theorem.

The proof of the Runge-Gross theorem is as follows: We consider time propagation of a $N$-electron system under an external potential $v(\boldsymbol{r}, t)$. The time propagation of the system is described by the following time-dependent Schrödinger equation for the many-electron system:

$$i\frac{\partial}{\partial t}|\Psi(t)\rangle = \hat{H}(t)|\Psi(t)\rangle = \left[\hat{T} + \hat{V}_{ee} + \hat{V}(t)\right]|\Psi(t)\rangle, \tag{2.23}$$

where $\hat{T}$ is the kinetic-energy operator, $\hat{V}_{ee}$ is the Coulomb repulsion operator. The external potential operator $\hat{V}(t)$ is defined by using the field operators $\hat{\psi}_s(\boldsymbol{r})$ as follows:

$$\hat{V}(t) = \sum_s \int d\boldsymbol{r}\hat{\psi}_s^\dagger(\boldsymbol{r})v(\boldsymbol{r}, t)\hat{\psi}_s(\boldsymbol{r}). \tag{2.24}$$

A mapping from one external potential to one time-dependent density, $v \to n$, is defined by the time-dependent Schrödinger equation (2.23) since the time-dependent density $n(\boldsymbol{r}, t)$ is defined by the wavefunction as,

$$n(\boldsymbol{r}, t) = \langle\Psi(t)|\hat{n}(\boldsymbol{r})|\Psi(t)\rangle, \tag{2.25}$$

where $\hat{n}$ is the density operator defined by $\hat{n}(\boldsymbol{r}) = \sum_s \int d\boldsymbol{r}'\hat{\psi}_s^\dagger(\boldsymbol{r}')\delta(\boldsymbol{r} - \boldsymbol{r}')\hat{\psi}_s(\boldsymbol{r}')$.

We next investigate whether this mapping $n \to v$ is invertible. Here we employ two relations: One is the relation between an external potential and a current density. The other is that between an electron density and a current density.

We consider two different external potentials $v(\boldsymbol{r}, t)$ and $v'(\boldsymbol{r}, t)$. The difference of these potentials is not only a spatially-uniform, time-dependent constant, $c(t)$:

$$v(\boldsymbol{r}, t) - v'(\boldsymbol{r}, t) \neq c(t). \tag{2.26}$$

If these external potentials, $v(\boldsymbol{r}, t)$ and $v'(\boldsymbol{r}, t)$, can be expanded as Taylor series, there must be a certain integer $k > 0$ that satisfies the following relation,

$$\frac{\partial^k}{\partial t^k}[v(\boldsymbol{r}, t) - v'(\boldsymbol{r}, t)]|_{t=t_0} \neq 0. \tag{2.27}$$

We then introduce two wavefunctions $|\Psi(t)\rangle$ and $|\Psi'(t)\rangle$ that are propagated under the external potentials $v(\boldsymbol{r}, t)$ and $v'(\boldsymbol{r}, t)$ from the same initial condition $|\Psi_0\rangle$ at time $t = t_0$. According to conventional manner, current density is defined as:

$$\boldsymbol{j}(\boldsymbol{r}, t) = \langle\Psi(t)|\hat{\boldsymbol{j}}|\Psi(t)\rangle, \tag{2.28}$$

$$\boldsymbol{j}'(\boldsymbol{r}, t) = \langle\Psi'(t)|\hat{\boldsymbol{j}}|\Psi'(t)\rangle, \tag{2.29}$$

where $\hat{\boldsymbol{j}}$ is a current operator,

$$\hat{\boldsymbol{j}} = \frac{1}{2i}\sum_s \left[\{\nabla\hat{\psi}_s^\dagger(\boldsymbol{r})\}\hat{\psi}_s(\boldsymbol{r}) - \hat{\psi}_s^\dagger(\boldsymbol{r})\{\nabla\hat{\psi}_s(\boldsymbol{r})\}\right]. \tag{2.30}$$

The equation of motion of the current density is as follows:

$$i\frac{\partial}{\partial t}\boldsymbol{j}(\boldsymbol{r},t) = \langle\Psi(t)|[\hat{\boldsymbol{j}}(\boldsymbol{r}),\hat{H}(t)]|\Psi(t)\rangle. \tag{2.31}$$

Here, we consider the time derivative of the current-density difference, $\boldsymbol{j}(\boldsymbol{r},t) - \boldsymbol{j}'(\boldsymbol{r},t)$. The derivative satisfies the following relation at $t = t_0$,

$$
\begin{aligned}
\frac{\partial}{\partial t}[\boldsymbol{j}(\boldsymbol{r},t) - \boldsymbol{j}'(\boldsymbol{r},t)]|_{t=t_0} &= -i\langle\Psi_0|[\hat{\boldsymbol{j}}(\boldsymbol{r}),\hat{V}(t_0) - \hat{V}'(t_0)]|\Psi_0\rangle \\
&= -n(\boldsymbol{r},t_0)\boldsymbol{\nabla}[v(\boldsymbol{r},t_0) - v'(\boldsymbol{r},t_0)],
\end{aligned}
\tag{2.32}
$$

where $n(\boldsymbol{r},t_0)$ is the electron density corresponding to the initial wavefunction $|\Psi_0\rangle$. Furthermore, by taking $k$-th order time-derivative of this equation, one can derive the following relation,

$$\frac{\partial^{k+1}}{\partial t^{k+1}}[j(\boldsymbol{r},t) - \boldsymbol{j}'(\boldsymbol{r},t)]|_{t=t_0} = -n(\boldsymbol{r},t_0)\boldsymbol{\nabla}\left\{\frac{\partial^k}{\partial t^k}[v(\boldsymbol{r},t_0) - v'(\boldsymbol{r},t_0)]\right\}. \tag{2.33}$$

In terms of the equation of continuity, we have the following relation,

$$\frac{\partial}{\partial t}\left[n(\boldsymbol{r},t) - n'(\boldsymbol{r},t)\right] = -\boldsymbol{\nabla}\cdot\left[\boldsymbol{j}(\boldsymbol{r},t) - \boldsymbol{j}'(\boldsymbol{r},t)\right], \tag{2.34}$$

where $n(\boldsymbol{r},t)$ and $n'(\boldsymbol{r},t)$ are electron densities of $|\Psi(t)\rangle$ and $|\Psi'(t)\rangle$, respectively. By taking $(k+1)$th order derivative of this equation, the following equation is derived,

$$\frac{\partial^{k+2}}{\partial t^{k+2}}\left[n(\boldsymbol{r},t) - n'(\boldsymbol{r},t)\right]|_{t=t_0} = -\boldsymbol{\nabla}\cdot\frac{\partial^{k+1}}{\partial t^{k+1}}\left[\boldsymbol{j}(\boldsymbol{r},t) - \boldsymbol{j}'(\boldsymbol{r},t)\right]|_{t=t_0}. \tag{2.35}$$

We obtained the two relation so far. One is the relation between $\boldsymbol{j}(\boldsymbol{r},t)$ and $v(\boldsymbol{r},t)$, which is Eq.(2.33). The other is the relation between $n(\boldsymbol{r},t)$ and $\boldsymbol{j}(\boldsymbol{r},t)$, which is Eq.(2.35). By comparing these relations, we obtain:

$$
\begin{aligned}
\frac{\partial^{k+2}}{\partial t^{k+2}}\left[n(\boldsymbol{r},t) - n'(\boldsymbol{r},t)\right]|_{t=t_0} &= \boldsymbol{\nabla}\cdot n(\boldsymbol{r},t_0)\boldsymbol{\nabla}\left\{\frac{\partial^k}{\partial t^k}\left[v(\boldsymbol{r},t) - v'(\boldsymbol{r},t)\right]|_{t=t_0}\right\} \\
&= \boldsymbol{\nabla}\cdot n(\boldsymbol{r},t_0)\boldsymbol{\nabla}w_k(\boldsymbol{r}),
\end{aligned}
\tag{2.36}
$$

where $w_k(\boldsymbol{r})$ is a function that is introduced to make the equation simple. The right hand side of Eq. (2.36) can be proven not to be zero, if the potentials $v(\boldsymbol{r},t)$ and $v'(\boldsymbol{r},t)$ satisfy Eq. (2.27). The proof is as follows: We consider the following integral:

$$
\begin{aligned}
\int d^3\boldsymbol{r}\, n(\boldsymbol{r},t_0)|\boldsymbol{\nabla}w_k(\boldsymbol{r})|^2 &= -\int d^3\boldsymbol{r}\, w_k(\boldsymbol{r})\boldsymbol{\nabla}\cdot[n(\boldsymbol{r},t_0)\boldsymbol{\nabla}w_k(\boldsymbol{r})] \\
&+ \int d\boldsymbol{S}\cdot[n(\boldsymbol{r},t_0)w_k(\boldsymbol{r})\boldsymbol{\nabla}w_k(\boldsymbol{r})].
\end{aligned}
\tag{2.37}
$$

The second term of the right hand side is a surface integral. If the integral region is sufficiently large, the surface integral vanishes. The integral of the left hand side must be positive for reasonable problems. Therefore, the first term of the right hand side must be positive, and a part of integrand, $\boldsymbol{\nabla}\cdot n(\boldsymbol{r},t_0)\boldsymbol{\nabla}w_k(\boldsymbol{r})$, cannot be zero everywhere. Finally, it has been proven that the right hand side of

Eq. (2.36) cannot be zero, and two *different* external potentials must give different electron densities. Therefore, the mapping $v \to n$ is invertible. The one-to-one correspondence between an external potential and density has been proven.

Analogously to the ground-state case, we introduce a non-interacting Fermionic system $|\Phi_{KS}(t)\rangle$ described by a set of time-dependent single-particle orbitals $\{\phi_i(\boldsymbol{r}, t)\}$: The system is called time-dependent Kohn-Sham system, and the orbitals are called time-dependent Kohn-Sham orbitals. The time-dependent Kohn-Sham system is defined so that its time-dependent electron density reconstructs the exact electron-density of the many-electron system,

$$n(\boldsymbol{r}, t) = \langle \Psi(t) | \hat{n}(\boldsymbol{r}) | \Psi(t) \rangle = \langle \Phi_{KS}(t) | \hat{n}(\boldsymbol{r}) | \Phi_{KS}(t) \rangle = \sum_i^N |\phi_i(\boldsymbol{r}, t)|^2, \qquad (2.38)$$

and the time-dependent Kohn-Sham orbitals satisfy the time-dependent Kohn-Sham equation,

$$i\frac{\partial}{\partial t}\phi_n(\boldsymbol{r}, t) = \hat{h}_{KS}(t)\phi_n(\boldsymbol{r}, t), \qquad (2.39)$$

$$\hat{h}_{KS}(t) = -\frac{1}{2}\nabla^2 + v_s[n(\boldsymbol{r}, t), |\Psi(t = t_0)\rangle](\boldsymbol{r}, t), \qquad (2.40)$$

where $v_s(\boldsymbol{r}, t)$ is the time-dependent Kohn-Sham potential. Because of the Runge-Gross theorem for the time-dependent Kohn-Sham system, the time-dependent Kohn-Sham potential $v_s(\boldsymbol{r}, t)$ is uniquely defined, once the time-dependent electron density $n(\boldsymbol{r}, t)$ is given.

Referring to the Kohn-Sham potential of Eq. (2.22) in the ground state, the time-dependent Kohn-Sham potential can be written as

$$v_s(\boldsymbol{r}, t) = v_{ext}(\boldsymbol{r}, t) + \int d\boldsymbol{r}' \frac{n(\boldsymbol{r}', t)}{|\boldsymbol{r} - \boldsymbol{r}'|} + v_{xc}(\boldsymbol{r}, t), \qquad (2.41)$$

where the second term is the time-dependent Hartree potential, and the third term is a time-dependent exchange-correlation potential. If one could employ the *exact* time-dependent exchange-correlation potential, the Kohn-Sham system would give the same electron density as the many-electron system. However, the exact time-dependent exchange-correlation potential has not been constructed for three-dimensional realistic system. Therefore, we need to approximate a time-dependent exchange-correlation potential when we apply the TDDFT to practical problems.

### 2.2.2 Time-dependent Kohn-Sham equation for crystalline solids

In order to describe electron dynamics in crystalline solids under laser fields, we introduce the time-dependent Kohn-Sham equation for solids. Typical wave-length of laser fields is a micrometer scale, the length scale of electron dynamics is subnanometer. Thanks to the large difference of spatial-scales between laser-fields and electron dynamics, we treat laser-fields as a spatially-uniform, time-varying electric field $\boldsymbol{E}(t)$ in a unit cell of crystalline solids. This is a dipole approximation for interactions of light with electrons. Within the dipole approximation, electron dynamics in a crystalline solids under a laser fields can be described by the following time-dependent Kohn-Sham equation:

$$i\frac{\partial}{\partial t}\phi_n(\boldsymbol{r}, t) = \left[-\frac{1}{2}\nabla^2 + v_{ion}(\boldsymbol{r}) + v_H(\boldsymbol{r}, t) + v_{xc}(\boldsymbol{r}, t) + e\boldsymbol{E}(t) \cdot \boldsymbol{r}\right]\phi_n(\boldsymbol{r}, t),$$

$$(2.42)$$

where $v_{ion}(\boldsymbol{r})$ is an ionic potential, $v_H(\boldsymbol{r})$ is the time-dependent Hartree potential, and $v_{xc}(\boldsymbol{r})$ is a time-dependent exchange-correlation potential. The interaction with the laser field is also included as a scalar potential, $e\boldsymbol{E}(t)\cdot\boldsymbol{r}$.

Here, we apply a gauge transformation to the Kohn-Sham orbitals, $\phi_n(\boldsymbol{r},t) = e^{-i\boldsymbol{A}(t)\cdot\boldsymbol{r}}\tilde{\phi}_n(\boldsymbol{r},t)$, and we then rewrite the time-dependent Kohn-Sham equation as follows:

$$i\frac{\partial}{\partial t}\tilde{\phi}_n(\boldsymbol{r},t) = \left[\frac{1}{2}\left(-i\nabla + \frac{e}{c}\boldsymbol{A}(t)\right)^2 + v_{ion}(\boldsymbol{r}) + v_H(\boldsymbol{r},t) + v_{xc}(\boldsymbol{r},t)\right]\tilde{\phi}_n(\boldsymbol{r},t),$$
(2.43)

where the spatially-uniform, time-varying vector potential $\boldsymbol{A}(t)$ is related to the electric field $\boldsymbol{E}(t)$ as

$$\boldsymbol{E}(t) = -\frac{1}{c}\frac{\partial}{\partial t}\boldsymbol{A}(t).$$
(2.44)

The Kohn-Sham Hamiltonian of Eq.(2.43) has the same spatial periodicity as the crystal at each time. Therefore, we may apply the time-dependent Bloch theorem to the equation and rewrite it as:

$$i\frac{\partial}{\partial t}u_{b\boldsymbol{k}}(\boldsymbol{r},t) = \left[\frac{1}{2}\left(-i\nabla + \boldsymbol{k} + \frac{e}{c}\boldsymbol{A}(t)\right)^2 + v_{ion}(\boldsymbol{r}) + v_H(\boldsymbol{r},t) + v_{xc}(\boldsymbol{r},t)\right]u_{b\boldsymbol{k}}(\boldsymbol{r},t),$$
(2.45)

where $u_{b\boldsymbol{k}}(\boldsymbol{r},t)$ is a time-dependent Bloch orbital, which is related to the Kohn-Sham orbital as $\tilde{\phi}_n(\boldsymbol{r},t) = e^{i\boldsymbol{k}\cdot\boldsymbol{r}}u_{b\boldsymbol{k}}(\boldsymbol{r},t)$. The orbital index $n$ is replaced by the band index $b$ and the Bloch wave vector $\boldsymbol{k}$. We note that the Bloch function has the same periodicity as the crystal, $u_{b\boldsymbol{k}}(\boldsymbol{r}+\boldsymbol{a},t) = u_{b\boldsymbol{k}}(\boldsymbol{r},t)$.

So far, we assumed that the ionic potential $v_{ion}(\boldsymbol{r})$ is a spatially local operator. However, it may include nonlocal operator in space because of pseudopotential methods. In that case, we should write the ionic potential as the nonlocal potential $\hat{v}_{ion}$,

$$\hat{v}_{ion}\phi_n(\boldsymbol{r},t) = \int d\boldsymbol{r}' v_{ion}(\boldsymbol{r},\boldsymbol{r}')\phi_n(\boldsymbol{r}',t).$$
(2.46)

Even if the ionic potential includes non-local parts, we may apply the gauge transformation to the Kohn-Sham equation (2.42), and then we may utilize the time-dependent Bloch theorem.

Finally, we obtain the time-dependent Kohn-Sham equation for Bloch functions as follows:

$$i\frac{\partial}{\partial t}u_{b\boldsymbol{k}}(\boldsymbol{r},t) = \hat{h}_{KS}(t)u_{b\boldsymbol{k}}(\boldsymbol{r},t),$$
(2.47)

where the Kohn-Sham Hamiltonian $\hat{h}_{KS}(t)$ may include the non-local ionic potential. The Hamiltonian is defined by

$$\hat{h}_{KS}(t) = \frac{1}{2}\left(-i\nabla + \boldsymbol{k} + \frac{e}{c}\boldsymbol{A}(t)\right)^2 + \hat{v}_{ion}^{\boldsymbol{k}+e\boldsymbol{A}(t)/c} + v_H(\boldsymbol{r},t) + v_{xc}(\boldsymbol{r},t),$$
(2.48)

$$\hat{v}_{ion}^{\boldsymbol{k}+e\boldsymbol{A}(t)/c}u_{b\boldsymbol{k}}(\boldsymbol{r},t) = \int d\boldsymbol{r}' e^{-i(\boldsymbol{k}+e\boldsymbol{A}(t)/c)\cdot\boldsymbol{r}}v_{ion}(\boldsymbol{r},\boldsymbol{r}')e^{-i(\boldsymbol{k}+e\boldsymbol{A}(t)/c)\cdot\boldsymbol{r}'}u_{b\boldsymbol{k}}(\boldsymbol{r}',t).$$
.
(2.49)

In this work, we calculate dynamics only for valence electrons, employing norm conserving pseudopotentials [107] with separable approximation [108] for ionic-core. We thus use the time-dependent Kohn-Sham equation (2.47) including the non-local ionic potential to describe electron dynamics.

From the time-dependent Bloch orbitals $u_{b\bm{k}}(\bm{r},t)$, several physical quantities can be calculated in real-time. For later calculations, here we define a matter current density of electrons $\bm{j}(\bm{r},t)$,

$$\bm{j}(\bm{r},t) = \frac{1}{m_e} \sum_{b\bm{k}} n_{b\bm{k}} \Re \left[ u_{b\bm{k}}^*(\bm{r},t) \left\{ -i\hbar\bm{\nabla} + \hbar\bm{k} + \frac{e}{c}\bm{A}(t) \right\} u_{b\bm{k}}(\bm{r},t) \right], \tag{2.50}$$

where the occupation number $n_{b\bm{k}}$ satisfies $\sum_{b\bm{k}} n_{b\bm{k}} = N$. We also define spatially-averaged electric current density $\bm{J}(t)$,

$$\bm{J}(t) = -\frac{e}{\Omega} \int_\Omega d^3\bm{r}\,\bm{j}(\bm{r},t) + \bm{J}_{NL}(t), \tag{2.51}$$

where $\Omega$ is a volume of the unit cell. $\bm{J}_{NL}(t)$ is a contribution from the nonlocal part of the ionic pseudopotential given by:

$$\bm{J}_{NL}(t) = -\frac{e}{\Omega m_e} \sum_{b\bm{k}} n_{b\bm{k}} \int_\Omega d^3\bm{r}\,u_{b\bm{k}}^*(\bm{r},t)\frac{[\bm{r}, v^{\bm{k}+e\bm{A}(t)/c}]}{i\hbar} u_{b\bm{k}}(\bm{r},t). \tag{2.52}$$

## 2.3 TDDFT coupled with Maxwell's equation

So far, we have explained the theoretical methods to treat electron dynamics in a unit cell of crystalline solids induced by external electric fields. In order to describe extremely-nonlinear light-matter interactions, we need to treat feedback from electron dynamics to propagation of electromagnetic fields. For this purpose, a coupled theoretical framework of the TDDFT and the Maxwell's equation has been developed [100]. We call it *Maxwell + TDDFT Multi-scale simulation*. In this section, we explain this coupled method.

Typical wavelength of laser fields is a micrometer scale, while typical length scale of electron dynamics is subnanometer. Thanks to the spatial-scale difference, laser-solid interactions can be divided into two kinds of problems: One is propagation of electromagnetic fields, and the other is induced electron dynamics in solids. In order to describe these two problems in different spatial scale, we introduce two kinds of spatial coordinates with different spatial scales.

We first introduce macroscopic coordinates, $\bm{R}$, in order to describe macroscopic propagation of electromagnetic fields, $\bm{A}_{\bm{R}}(t)$ and $\phi_{\bm{R}}(t)$. Taking a specific gauge condition in which the scalar potential is always zero, $\phi_{\bm{R}}(t) = 0$, propagation of electromagnetic fields is described by the following macroscopic Maxwell's equation,

$$-\frac{1}{c}\bm{\nabla}_{\bm{R}} \cdot \bm{A}_{\bm{R}}(t) = 4\pi \rho_{c,\bm{R}}(t), \tag{2.53}$$

$$\frac{1}{c^2}\frac{\partial^2}{\partial t^2}\bm{A}_{\bm{R}}(t) - \nabla_{\bm{R}}^2 \bm{A}_{\bm{R}}(t) + \bm{\nabla}_{\bm{R}}\left[\bm{\nabla}_{\bm{R}} \cdot \bm{A}_{\bm{R}}(t)\right] = -\frac{4\pi}{c}\bm{J}_{\bm{R}}(t), \tag{2.54}$$

where $\rho_{c,\bm{R}}(t)$ is macroscopic charge density, and $\bm{J}_{\bm{R}}(t)$ is macroscopic current density. The macroscopic current density is given from a microscopic electron dynamics part which will be described

later. By assuming the charge neutrality in macroscopic coordinates, $\rho_{c,\boldsymbol{R}}(t) = 0$, we may simplify Eq. (2.54) as

$$\frac{1}{c^2}\frac{\partial^2}{\partial t^2}\boldsymbol{A_R}(t) - \nabla_{\boldsymbol{R}}^2\boldsymbol{A_R}(t) = -\frac{4\pi}{c}\boldsymbol{J_R}(t). \tag{2.55}$$

This is the basic equation of motion for macroscopic propagation of electromagnetic fields.

We next consider Bloch orbitals, $u_{bk\boldsymbol{R}}(\boldsymbol{r}, t)$, at each macroscopic point $\boldsymbol{R}$ in order to describe the microscopic electron dynamics induced by the macroscopic electromagnetic field, $\boldsymbol{A_R}(t)$. We shall call the spatial coordinates for the Bloch orbital, $\boldsymbol{r}$, microscopic coordinates. We describe the time-evolution of the Bloch orbitals based on the following time-dependent Kohn-Sham equation,

$$i\frac{\partial}{\partial t}u_{nk\boldsymbol{R}}(\boldsymbol{r}, t) = \hat{h}_{KS,\boldsymbol{kR}}(t)u_{nk\boldsymbol{R}}(\boldsymbol{r}, t), \tag{2.56}$$

$$\hat{h}_{KS,\boldsymbol{kR}}(t) = \frac{1}{2}\left(-i\nabla + \boldsymbol{k} + \frac{e}{c}\boldsymbol{A_R}(t)\right)^2 + \hat{v}_{ion,\boldsymbol{R}}^{\boldsymbol{k}+e\boldsymbol{A_R}(t)/c} + v_{H,\boldsymbol{R}}(\boldsymbol{r}, t) + v_{xc,\boldsymbol{R}}(\boldsymbol{r}, t), \tag{2.57}$$

where vector, ionic, Hartree and exchange-correlation potentials depend on the macroscopic coordinates $\boldsymbol{R}$. The Kohn-Sham equation (2.56) is the basic equation of motion for microscopic electron dynamics induced by electromagnetic fields. Although the macroscopic vector potential $\boldsymbol{A_R}(t)$ is a spatially-varying quantity in the macroscopic coordinates, it is treated as a spatially-uniform, time-varying field in the microscopic coordinates because of the difference of the spatial-scales.

In order to describe the feedback from microscopic electron dynamics to macroscopic propagation of electromagnetic fields, we then define the macroscopic current $\boldsymbol{J_R}(t)$ based on the Bloch orbitals,

$$\boldsymbol{J_R}(t) = -\frac{e}{m\Omega}\sum_{b\boldsymbol{k}}\int_{\Omega}d\boldsymbol{r}u_{bk\boldsymbol{R}}^*(\boldsymbol{r}, t)\boldsymbol{\pi}_{\boldsymbol{kR}}(t)u_{bk\boldsymbol{R}}(\boldsymbol{r}, t), \tag{2.58}$$

where $\Omega$ is a volume of unit cell, and $\boldsymbol{\pi_k}(t)$ is the kinematic momentum operator defined by:

$$\begin{aligned}\boldsymbol{\pi}_{\boldsymbol{kR}}(t) &= \frac{\left[\boldsymbol{r}, \hat{h}_{KS,\boldsymbol{kR}}(t)\right]}{i\hbar} \\ &= \boldsymbol{p} + \hbar\boldsymbol{k} + \frac{e}{c}\boldsymbol{A_R}(t) + \frac{\left[\boldsymbol{r}, \hat{v}_{ion,\boldsymbol{R}}^{\boldsymbol{k}+e\boldsymbol{A_R}(t)/\hbar c}(t)\right]}{i\hbar}.\end{aligned} \tag{2.59}$$

We have obtained the macroscopic equation for electromagnetic fields of Eq. (2.55), and the microscopic equation for electrons of Eq. (2.56). These two equations are connected via the macroscopic current of Eq. (2.58). In order to describe laser-solid interactions, we solve these three equations, consistently.

## 2.4 Functionals and potentials

As mentioned above, we have to approximate exchange-correlation functionals or potentials in order to apply the DFT/TDDFT to practical problems. In this section, we explain density functionals and potentials that will be employed in this study: We will employ the local density approximation (LDA)

proposed by Perdew and Zunger [106], and the meta generalized gradient approximation (meta-GGA) proposed by Tran and Blaha [103]. Furthermore, we will employ the adiabatic approximation for exchange-correlation potentials, in which the exchange-correlation potential at each time is determined by the density (current density, and kinetic density if necessary) at the same time.

### 2.4.1 Local density approximation

First we introduce a LDA for a density functional. In this approximation, we assume that electron density locally contributes to the exchange-correlation energy in space. Thus, we assume the following form for $E_{xc}[n]$:

$$E_{xc}^{LDA}[n] = \int d\boldsymbol{r} \epsilon_{xc}^{LDA}(n(\boldsymbol{r})) n(\boldsymbol{r}). \tag{2.60}$$

This assumption would be valid for the homogeneous electron gas.

One can derive the exchange-correlation potential of the LDA, $v_{xc}^{LDA}$ as follows:

$$v_{xc}^{LDA}(\boldsymbol{r}) = \frac{\delta E_{xc}^{LDA}}{\delta n(\boldsymbol{r})} = \epsilon_{xc}^{LDA}(n(\boldsymbol{r})) + n(\boldsymbol{r}) \frac{\delta \epsilon_{xc}^{LDA}(n(\boldsymbol{r}))}{\delta n(\boldsymbol{r})}. \tag{2.61}$$

The exchange-correlation energy density $\epsilon_{xc}^{LDA}$ can be divided into two parts: One is the exchange part $\epsilon_x^{LDA}$ and the other is the correlation part $\epsilon_c^{LDA}$:

$$\epsilon_{xc}^{LDA} = \epsilon_x^{LDA} + \epsilon_c^{LDA}. \tag{2.62}$$

We utilize the exchange energy of the homogeneous electron gas to $\epsilon_x^{LDA}$:

$$\epsilon_x^{LDA} = -\frac{3}{4} \left(\frac{3}{\pi}\right)^{1/3} n^{1/3}(\boldsymbol{r}). \tag{2.63}$$

For the correlation part $\epsilon_c^{LDA}$, we employ the Perdew and Zunger correlation functional of unpolarized system [106]:

$$\epsilon_c^{LDA} = \begin{cases} \gamma/(1 + \beta_1\sqrt{r_s} + \beta_2 r_s) & (r_s \geq 1) \\ A \ln r_s B + C r_s \ln r_s + D r_s & (r_s < 1), \end{cases} \tag{2.64}$$

where $r_s$ is related to the electron density $n = (4\pi r_s^3/3)^{-1}$. Other parameters $\gamma, \beta_1, \beta_2, A, B, C$ and $D$ are defined in the table 2.1 in atomic unit.

Both exchange and correlation parts of the LDA are constructed so as to reproduce the energy of the homogeneous electron gas. Thus, the LDA would be suitable to describe metallic system, since electrons in metals behave as free-electrons. On the other hand, the LDA may not be suitable to describe semiconductors and insulators. In deed, the LDA tends to underestimate band gap energies of semiconductors and insulators: This is well known as the band-gap problem of LDA.

Based on the adiabatic approximation, we simply replace the electron density $n(\boldsymbol{r})$ to the time-dependent electron density $n(\boldsymbol{r}, t)$, if we apply the LDA in the time-dependent Kohn-Sham equation.

| Parameter | Value in a.u. |
|:---:|:---:|
| $\gamma$ | -0.1423 |
| $\beta_1$ | 1.0529 |
| $\beta_2$ | 0.3334 |
| $A$ | 0.0311 |
| $B$ | -0.048 |
| $C$ | 0.0020 |
| $D$ | -0.0116 |

Table 2.1: Parameters of the Perdew and Zunger's LDA correlation functional [106].

### 2.4.2 meta-GGA

A large number of functionals and potentials have been developed beyond the LDA for various aims. One of the simplest extensions of the LDA is a generalized gradient approximation (GGA). In the GGA, the energy functional is described as a function of the local density $n(\boldsymbol{r})$ and its gradient $|\boldsymbol{\nabla}n(\boldsymbol{r})|$. Thus, the GGA functional has the following form:

$$E_{xc}^{GGA} = \int d\boldsymbol{r}\epsilon(n(\boldsymbol{r}), |\nabla n(\boldsymbol{r})|)n(\boldsymbol{r}). \tag{2.65}$$

One of the most popular GGA functionals is the PBE functional [109].

A more generalized functional has been proposed. It is called the meta-GGA. The meta GGA includes not only the local density $n(\boldsymbol{r})$ and its gradient $|\nabla n(\boldsymbol{r})|$, but also its Laplacian $\nabla^2 n(\boldsymbol{r})$ and a kinetic energy density $\tau(\boldsymbol{r})$,

$$\tau(\boldsymbol{r}) = \sum_n |\nabla\phi_n(\boldsymbol{r})|^2. \tag{2.66}$$

Tran and Blaha have proposed a meta-GGA potential [103]. We abbreviate it the TB-mBJ potential. The TB-mBJ potential is a kind of modification of an exchange-correlation potential proposed by Becke and Johnson [110]. Both the TB-mBJ and Becke-Johnson potentials include a potential proposed by Becke and Roussel [111]. We note that the Becke-Roussel potential reproduces the proper asymptotic behavior of the exchange potential , $-1/r$, in isolated systems.

The TB-mBJ exchange potential is defined as follows,

$$v_x^{TB-mBJ}(\boldsymbol{r}) = c_m v_x^{BR}(\boldsymbol{r}) + (3c_m - 2)\frac{1}{\pi}\sqrt{\frac{5}{12}}\sqrt{\frac{\tau(\boldsymbol{r})}{n(\boldsymbol{r})}}, \tag{2.67}$$

where $v_x^{BR}(\boldsymbol{r})$ is the Becke-Roussel potential. In the original paper [103], the parameter $c_m$ is defined by,

$$c_m = \alpha + \beta \left( \frac{1}{V_{cell}} \int_{cell} \frac{|\nabla n(\boldsymbol{r})|}{n(\boldsymbol{r})} \right)^{1/2}, \tag{2.68}$$

where $\alpha = -0.012$ and $\beta = 1.023\text{bohr}^{1/2}$. Loller, Tran and Blaha have found that the band gap energies much depend on this $c_m$ parameter [112]. In this work, we thus choose the $c_m$-parameter so

that the Kohn-Sham gap coincides with the experimental band gap of the material. We note that even if we could employ the *exact* functional, the Kohn-Sham gap does not need to coincide with the experimental band gap due to the derivative discontinuity of the Kohn-Sham energy [113]. However, as will be shown later, optical gaps of dielectrics are well described if we choose the $c_m$-parameter so that the Kohn-Sham band gap coincides with the experimental gap.

The TB-mBJ potential in the adiabatic approximation has the following form:

$$v_x^{TB-mBJ}(\boldsymbol{r},t) = c_m v_x^{BR}(\boldsymbol{r},t) + (3c_m - 2)\frac{1}{\pi}\sqrt{\frac{5}{12}}\sqrt{\frac{\tau(\boldsymbol{r},t)}{n(\boldsymbol{r},t)}}, \tag{2.69}$$

where the time-dependent kinetic energy density $\tau(\boldsymbol{r},t)$ is given by

$$\tau(\boldsymbol{r},t) = \sum_n \left| \left\{ -i\nabla + \frac{e}{c}\boldsymbol{A}(t) \right\} \phi_n(\boldsymbol{r}) \right|^2. \tag{2.70}$$

The potential of Eq. (2.69) is not gauge invariant since the kinetic energy density of Eq. (2.70) is not [114–117]. To recover the gauge invariance, we replace the all kinetic energy density terms in the potential as

$$\tau(\boldsymbol{r},t) \rightarrow \tau(\boldsymbol{r},t) - \frac{\boldsymbol{j}^2(\boldsymbol{r},t)}{n(\boldsymbol{r},t)}, \tag{2.71}$$

where $\boldsymbol{j}(\boldsymbol{r},t)$ is the matter current density,

$$\boldsymbol{j}(\boldsymbol{r},t) = \frac{1}{m}\sum_i \Re\left[ \phi_i^*(\boldsymbol{r},t)\left\{ -i\boldsymbol{\nabla} + \frac{e}{c}\boldsymbol{A}(t)\phi_i(\boldsymbol{r},t) \right\} \right]. \tag{2.72}$$

Unlike the LDA potential, the TB-mBJ potential may cause some problems in the real-time TDDFT calculation. In Sec. 4.3, we will see that the TB-mBJ potential sometimes causes numerical instability in the real-time propagation. We find that a predictor-corrector procedure recovers the stability of the calculation. The TB-mBJ potential is directly defined as a potential without referring to any functionals. Functionals that derive the potential are unknown. Therefore, it is impossible to evaluate the total energy of electronic systems and electronic excitation energy using the energy functional. In Sec. 4.4, in order to evaluate the electronic excitation energy without referring to functoinals, we will develop a method in which the excitation energy is calculated as work done by external fields to systems.

# Chapter 3

# Numerical Aspects

## 3.1 Homemade computational code for electron dynamics in solids

We have been developing a computational code by ourselves in order to pragmatically conduct electron dynamics calculation based on the time-dependent density functional theory (TDDFT) introduced in Chap. 2. The name of the code is *Ab-initio Real-Time Electron Dynamics simulator; ARTED*. ARTED is applicable to two kinds of first-principles calculations. One is the calculation for electron dynamics in a unit cell of crystalline solids under given external electric fields, solving the time-dependent Kohn-Sham equation for crystalline solids (2.47). We call it the *single-cell* simulation. The other is the calculation for coupled dynamics of electrons and electromagnetic fields in medium, solving the coupled equation: The time-dependent Kohn-Sham equation for microscopic electron-dynamics (2.56) and the Maxwell's equation for macroscopic propagation of electromagnetic fields (2.55). We call it the *multi-scale* simulation. In both the single-cell and multi-scale simulations, we solve the time-dependent Kohn-Sham equation in real-time since the real-time simulation is suitable to investigate light-matter interactions in strongly nonlinear conditions.

Parallel computing is implemented with the Message Passing Interface (MPI) and OpenMP in ARTED since the real-time TDDFT calculations are computationally expensive. Particularly, the multi-scale simulation is much expensive because many real-time TDDFT calculations are required to be conducted simultaneously. Therefore, it is necessary to employ a large-scale supercomputer like the K computer at RIKEN in order to conduct the multi-scale simulation. We optimize ARTED for massively parallel computing with several tens of thousands of CPU cores.

In this chapter, we introduce numerical implementations of the single-cell and multi-scale simulations in ARTED. Then, we demonstrate parallel efficiency and computational performance of ARTED in massive parallel computing.

## 3.2 Numerical implementation of the single-cell simulation

In order to solve the time-dependent Kohn-Sham equation for solids (2.47), we employ real-space and real-time methods. The equation includes two kinds of independent variables: One is a spatial variable $r$ and the other is time $t$. We employ the real-space method to treat the spatial variable, and the real-time method to the time.

### 3.2.1   Real space method

The real-space method is a finite difference method in real-space $\boldsymbol{r}$. In this method, three dimensional Cartesian coordinates are discretized in uniform grids. By using the grids, the Bloch orbitals are described as follows:

$$u_{b\boldsymbol{k}}(\boldsymbol{r}, t) \rightarrow u_{b\boldsymbol{k}}(\boldsymbol{r}_i, t), \tag{3.1}$$

where an integer $i$ represents a serial number of spatial grids in a unit cell. Thus, the number $i$ corresponds to the three dimensional indices $(j, k, l)$ as follows:

$$\boldsymbol{r}_i = (x_j, y_k, z_l). \tag{3.2}$$

In the real-space method, operation of a general operator $\hat{O}$ to a Bloch orbital $u_{b\boldsymbol{k}}(\boldsymbol{r}, t)$ is described by

$$\left[\hat{O} u_{b\boldsymbol{k}}\right](\boldsymbol{r}_i, t) = \sum_j^{N_L} O_{ij} u_{b\boldsymbol{k}}(\boldsymbol{r}_j, t), \tag{3.3}$$

where $O_{ij}$ is a matrix representation of the operator $\hat{O}$ in the grid space. For example, matrix elements of spatially local operators have the form of $O_{ij} = O_i \delta_{ij}$, and those of spatial derivative operators are described by coefficients of finite-difference formulae. Therefore, the operation of the Kohn-Sham Hamiltonian is computed by

$$[h_{\boldsymbol{k}}(t) u_{b,\boldsymbol{k}}](\boldsymbol{r}_i, t) = \sum_j h_{ij} u_{b\boldsymbol{k}}(\boldsymbol{r}_j). \tag{3.4}$$

The Hamiltonian matrix $h_{ij}$ includes the following terms,

$$
\begin{aligned}
h_{ij} &= -\frac{1}{2} C_{ij} + i \left(\boldsymbol{k} + \frac{e}{c} \boldsymbol{A}(t)\right) \cdot \boldsymbol{g}_{ij} + v_{ion,ij}^{nonlocal} \\
&+ \delta_{ij} \left[-\left(\boldsymbol{k} + \frac{e}{c} \boldsymbol{A}(t)\right)^2 / 2 + v_{ion}^{local}(\boldsymbol{r}_i) + v_H(\boldsymbol{r}_i) + v_{xc}(\boldsymbol{r}_i)\right],
\end{aligned} \tag{3.5}
$$

where $C_{ij}$ and $\boldsymbol{g}_{ij}$ are coefficients of finite difference formulae for the Laplacian $\nabla^2$ and the gradient $\boldsymbol{\nabla}$, respectively. Here, $v_{ion}^{local}$ represents the local part of the ionic potential, and $v_{ion}^{nonlocal}$ represents the non-local part.

Moreover, an expectation value of the operator $\hat{O}$ is evaluated by summation in the grid space as follows:

$$\langle O \rangle = \Delta V \sum_{ij} u_{b\boldsymbol{k}}^*(\boldsymbol{r}_i) O_{ij} u_{b\boldsymbol{k}}(\boldsymbol{r}_j), \tag{3.6}$$

where $\Delta V$ is a volume of a discretized unit.

### 3.2.2   Real time method

In order to describe time-propagation of the Bloch orbitals $u_{b\boldsymbol{k}}(\boldsymbol{r}, t)$ solving the time-dependent Kohn-Sham equation (2.47), we employ the real-time method, which is the finite difference method in time.

In this method, the time-propagation is conducted by repeating time-propagation for a small time-step $\Delta t$ as follows:

$$
\begin{aligned}
u_{b\boldsymbol{k}}(\boldsymbol{r},t) &= U(t;t_0)u_{b\boldsymbol{k}}(\boldsymbol{r},t_0) \\
&= U(t;t-\Delta t)\cdots U(t_0+2\Delta t;t_0+\Delta t)U(t_0+\Delta t;t_0)u_{b\boldsymbol{k}}(\boldsymbol{r},t_0),
\end{aligned}
$$
(3.7)

where $U(t_2;t_1)$ is a time-propagation operator from $t_1$ to $t_2$. Assuming the change of the Hamiltonian in time is tiny during the small time step $\Delta t$, the time-propagation operator for the small time step can be approximated by

$$
U(t+\delta t;t) \approx \exp\left[-\frac{i\Delta t}{\hbar}h_{\boldsymbol{k}}(t+\Delta t/2)\right].
$$
(3.8)

For practical calculations, we expand the propagation operator in a Taylor series [90, 91]:

$$
\exp\left[-\frac{i\Delta t}{\hbar}h_{\boldsymbol{k}}(t+\Delta t/2)\right] \approx \sum_{k=0}^{N}\frac{\{-i\Delta t h_{\boldsymbol{k}}(t+\Delta t/2)\}^k}{k!}.
$$
(3.9)

The order of the truncation $N$ should be more than 2 for stable time evolution. If the operator is expanded in the first or second order

$$
e^{-ix} \approx 1-ix,
$$
$$
e^{-ix} \approx 1-ix-x^2/2,
$$

norm of these operators is always more than 1,

$$
|1-ix|^2 = 1+x^2 > 1,
$$
(3.10)
$$
|1-ix-x^2/2|^2 = (1-x^2/2)^2+x^2 = 1+x^4/4 > 1.
$$
(3.11)

Therefore, if we employ the first or second order expansions for the time-propagation operator, norm of the Bloch orbitals grows larger, and finally diverges. For stable time-evolution, we must expand the operator by more than the second order Taylor series, and must choose a sufficiently small time-step $\Delta t$. In this work, we fix the truncation number $N$ to 4.

In the above procedure, we need to guess the Hamiltonian at time $t+\Delta t/2$. In calculations using the local density approximation potential, we find that use of the Hamiltonian at time $t$, $h_{KS}(t+\Delta t/2) \sim h_{KS}(t)$, provides results with sufficient accuracy. However, we have found that the predictor-corrector procedure to approximately evaluate $h_{KS}(t+\Delta t/2)$ is indispensable for stable time-evolution when we employ the meta generalized gradient approximation potential proposed by Tran and Blaha [103]. The predictor-corrector procedure is usually carried out in the following steps [118]: We first calculate wave functions $\psi_i^{pred}(\boldsymbol{r},t+\Delta t)$ using the Hamiltonian at time $t$,

$$
\psi_i^{pred}(\boldsymbol{r},t+\Delta t) = \exp\left[\frac{h_{KS}(t)\Delta t}{i\hbar}\right]\psi_i(\boldsymbol{r},t).
$$
(3.12)

Using the Kohn-Sham orbitals $\psi_i^{pred}$, we next construct the Hartree potential $v_H^{pred}$ and the exchange correlation potential $v_{xc}^{pred}$ at time $t+\Delta t$. We then approximate the Hamiltonian at time $t+\Delta t/2$ by averaging the potentials at time $t$ and $t+\Delta t$ as follows:

$$
v_H(\boldsymbol{r},t+\frac{\Delta t}{2}) \approx \frac{v_H^{pred}(\boldsymbol{r},t+\Delta t)+v_H(\boldsymbol{r},t)}{2},
$$
(3.13)

$$v_{xc}(\boldsymbol{r}, t + \frac{\Delta t}{2}) \approx \frac{v_{xc}^{pred}(\boldsymbol{r}, t + \Delta t) + v_{xc}(\boldsymbol{r}, t)}{2}. \tag{3.14}$$

Finally, we calculate the Kohn-Sham orbitals at $t + \Delta t$ using the Hamiltonian at time $t + \Delta t/2$.

We will see the necessity of the predictor-corrector procedure in the real-time TDDFT calculation with the meta-GGA in Sec. 4.3.

## 3.3 Parallelization of the single-cell simulation

We have been developing ARTED code so as to use it on massively parallel supercomputers. ARTED can be used in parallel computing with both flat MPI and MPI + OpenMP hybrid parallelizations. Here, we describe how to parallelize the single-cell TDDFT simulation.

The most time-consuming part of the electron dynamics calculation is the operation of the Hamiltonian to each Bloch orbital. This procedure accounts for about 80% of total computational costs. We have several possibilities to parallelize the electron dynamics calculation in which the time-propagation of the Bloch orbitals $u_{b\boldsymbol{k}}(\boldsymbol{r}, t)$ are calculated. One possibility is parallelization for the $k$-points, $\boldsymbol{k}$. Another is for the band index, $b$. These two variables are orbital indices. The orbital indices are suitable for parallelization of the time-propagation because the operation of the Hamiltonian can be independently conducted for each orbital. The other possibility of the parallelization is for the real-space grids. The grid parallelization is one of the efficient parallelizations for spatially large systems [119]. However, we are interested in electron dynamics in crystalline solids, and the size of unit-cell has not been large so far. Therefore, we do not adopt the real-space parallelization. Thus, we employ the $k$-points and the band indices for the parallel computing.

Figure 3.1 shows a schematic picture of the parallelization for the electron dynamics calculation in ARTED. As mentioned above, we have the two kinds of orbital indices, the $k$-points $\boldsymbol{k}$ and the band indices $b$. Each index can be labeled with serial numbers. We thus describe the orbitals on a two-dimensional map as in Fig. 3.1 where the $k$-points are described as a horizontal coordinate and the band indices are described as vertical. In our implementation, the $k$-points can be parallelized with the MPI parallelization. Moreover, $k$-points and the band indices can be parallelized with the OpenMP parallelization. Therefore, ARTED can be used in the MPI + OpenMP hybrid parallelization.

For the MPI parallelization of the electron dynamics calculation, communication among MPI processes is necessary to construct the Kohn-Sham Hamiltonian at each time step since summation for all $k$-points and band indices are required to provide the electron density $n(\boldsymbol{r}, t)$, the kinetic energy density $\tau(\boldsymbol{r}, t)$, and the current density $\boldsymbol{j}(\boldsymbol{r}, t)$. We note that the cost of data-communication is relatively small, compared with whole computational costs. Therefore, as will be shown, ARTED shows good parallel efficiency for massively parallel calculations.

## 3.4 Computational performance of the single-cell simulation

In this section, we illustrate numerical performance of the single-cell TDDFT simulation with the ARTED code. We examined the performance at the K computer, employing crystalline silicon calculation. In the calculation, there are eight atoms in a cubic unit cell, and each atom has four valence electrons. Thus, we have 32 electrons and 16 Bloch orbitals in the unit cell because of spin-degeneration. The unit cell is discretized by $24^3$ uniform grid points, and the reciprocal lattice space is discretized by $32^3$ $k$-points.

Index of Bloch wave number $\boldsymbol{k}$

Index of bands $b$

| MPI-Rank 0 |
| OMP-Thread 0 |
| $(b, \boldsymbol{k}) = (1,1)$ |
| $(2,1)$ |

| OMP-Thread 1 |
| $(3,1)$ |
| $(4,1)$ |

| MPI-Rank 1 |
| OMP-Thread 0 |
| $(b, \boldsymbol{k}) = (1,2)$ |
| $(2,2)$ |

| OMP-Thread 1 |
| $(3,2)$ |
| $(4,2)$ |

$\bullet \bullet \bullet$
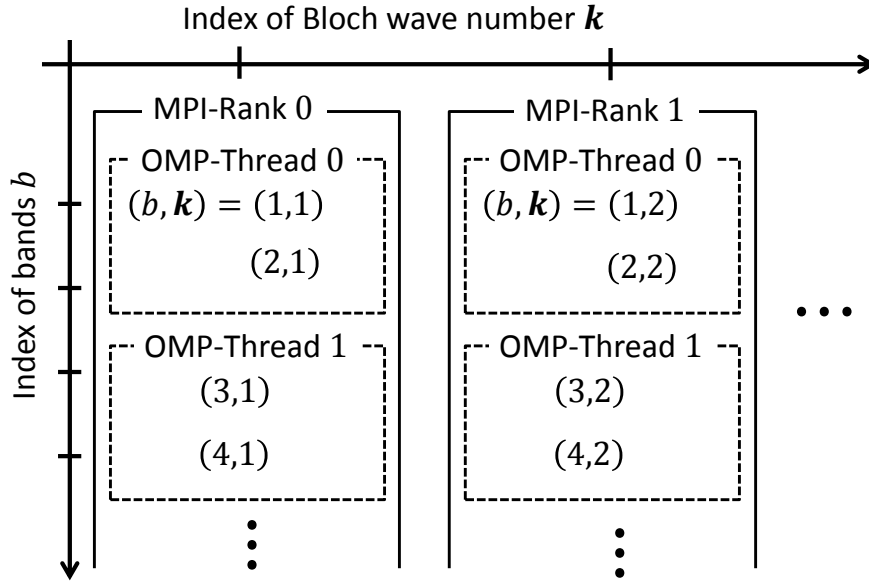
Figure 3.1: Schematic picture of parallelization for the electron dynamics calculation in crystalline solids. In our implementation, the $k$-points and the band indices are parallelized with MPI+OpenMP hybrid parallelizations.

Figure 3.2 shows a strong-scaling parallel efficiency of ARTED at the K-computer. When using 65536 cores, the calculation is conducted with 8192 MPI processes times 8 OpenMP threads hybrid parallelization, each thread taking care of 8 orbitals. As seen from Fig. 3.2, ARTED achieves high parallel efficiency more than 80 %, even if we employ more than 60000 cores.

Figure 3.3 shows an effective performance of ARTED at the K-computer. ARTED achieves high effective performance near 30 %, employing more than 8,000 cores. It shows good performance more than 20 %, even in massive parallel computing employing more than 60,000 cores.

We thus conclude that ARTED is much suitable for massive parallel calculation employing more than 60000 cores. Moreover, it shows good effective performance too, more than 20 % in the massive parallel computing.
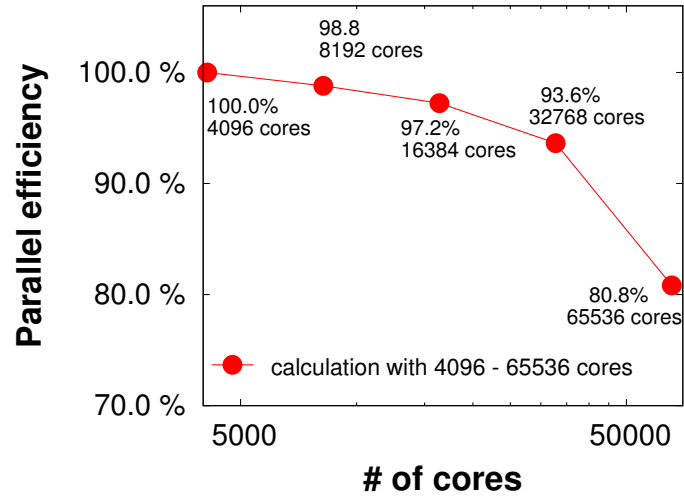
Figure 3.2: The strong-scaling parallel efficiency of the single-cell simulation with ARTED at the K-computer.
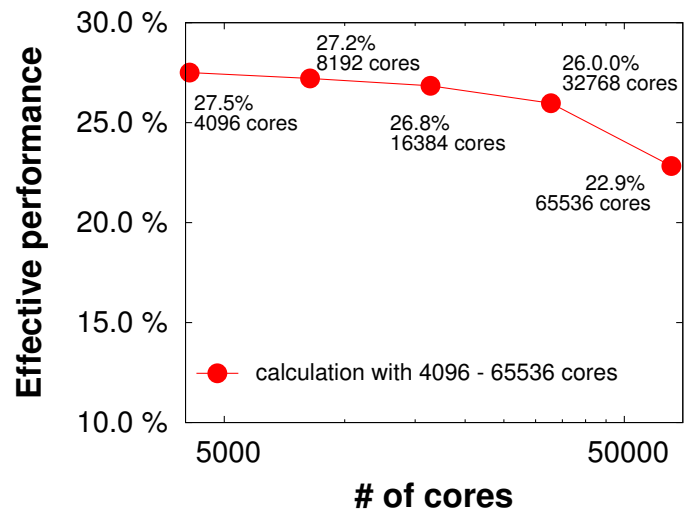


Figure 3.3: The effective performance of the single-cell simulation with ARTED at the K-computer.

## 3.5 Numerical implementation of the multi-scale simulation

We next describe the numerical implementation of the Maxwell + TDDFT multi-scale simulation solving the coupled equations of Eqs. (2.55), (2.56) and (2.58). Here, we only consider a simple case: a linearly polarized laser pulse normally irradiates on a bulk surface. Therefore, we only need to calculate one-dimensional propagation of electromagnetic fields in macroscopic coordinates, and take the propagation direction as $Z$-axis. A schematic picture of the implementation of the multi-scale simulation is shown in Fig. 3.4 where the surface of the bulk is taken to be at $Z = 0$.

As shown in the left hand side of Fig. 3.4, we first introduce macroscopic grid points in order to solve the macroscopic Maxwell's equation of Eq. (2.55). We simply solve the Maxwell's equation by using the three points formula of the finite difference method for both space and time:

$$
\begin{aligned}
\boldsymbol{A}_Z(t + \Delta t) &= 2\boldsymbol{A}_Z(t) - \boldsymbol{A}_Z(t - \Delta t) \\
&+ c^2 \Delta t^2 \frac{\boldsymbol{A}_{Z+\Delta Z} - 2\boldsymbol{A}_Z(t) + \boldsymbol{A}_{Z-\Delta Z}(t)}{\Delta Z^2} + 4\pi c \Delta t \boldsymbol{J}_Z(t),
\end{aligned}
\tag{3.15}
$$

where $\Delta t$ is the time step and $\Delta Z$ is the grid spacing. As seen from the formula, we need the vector potentials of time $t$ and $t - \Delta t$, and the electric current of time $t$ in order to compute the vector potential of time $t + \Delta t$. These two vector potentials are obtained from two previous iterations of the time-propagation, and the current is obtained from the following microscopic part. We note that the computational cost of this macroscopic propagation of electromagnetic fields is negligible, compared with the cost of the following microscopic electron dynamics calculation.
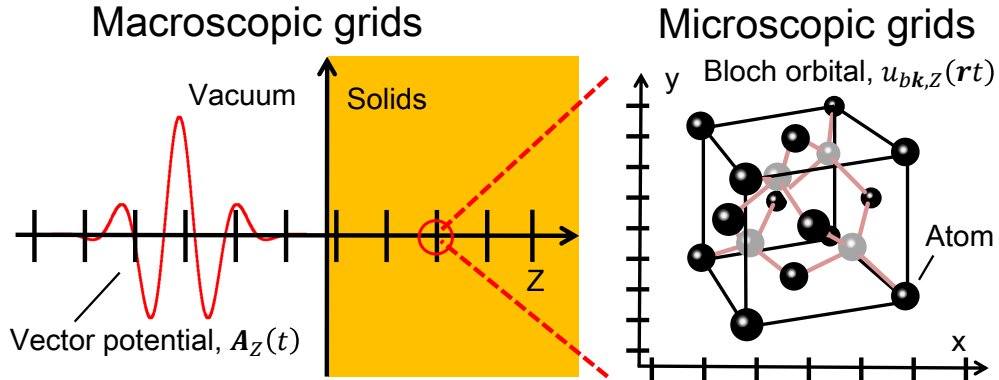


Figure 3.4: Schematic picture of the Maxwell + TDDFT multi-scale simulation. Left panel shows the macroscopic part and right panel shows the microscopic part.

In order to describe electron dynamics induced by the macroscopic vector potential $\boldsymbol{A}_Z(t)$, we next introduce microscopic grid points, which are shown in the right hand side of Fig. 3.4, at each macroscopic grid point $Z$. At each macroscopic grid point, we consider the Bloch orbitals $u_{b\boldsymbol{k},Z}(\boldsymbol{r}, t)$ on the microscopic grids. We calculate the time-propagation of the Bloch orbitals under the vector potential, by solving the time-dependent Kohn-Sham equation (2.56) with the real-space and real-time methods, which are described in Sec. 3.2. We then calculate the macroscopic current $\boldsymbol{J}_Z(t)$

from the time-propagated Bloch orbitals at each macroscopic grid point by Eq. (2.58). Finally, we use the obtained current in order to evolve the macroscopic vector potential $A_Z(t)$ by Eq. (3.15) for the next time step. We iteratively conduct these procedures and calculate the time-evolution of both electromagnetic fields and electrons.

We briefly summarize the procedures of the time-propagation in Fig. (3.5). In the initial step 00, we prepare the initial conditions for both the vector potential and the Bloch orbitals. For the vector potential, we prepare the incident pulse in the vacuum region. For the Bloch orbitals, we solve the static Kohn-Sham equations in a unit cell and prepare the ground state. From these initial conditions, we iteratively evolve $A_Z(t)$ and $u_{bk,Z}(r,t)$ by the following procedures. In step 01, we first evolve the vector potential $A_Z(t)$ for a small time step $\Delta t$ using Eq. (3.15). Here, the electric current $J_Z(t)$ and the vector potentials of previous time $A_Z(t)$ and $A_Z(t - \Delta t)$ are required.

In step 02, we then evolve the Bloch orbitals $u_{bk,Z}(r,t)$ for a small time step $\Delta t$. Here, we use the vector potential of time $t + \Delta t/2$ to obtain the Bloch orbitals of time $t + \Delta t$, $u_{bk,Z}(r, t + \Delta t)$. In pragmatic calculation, we approximate the vector potential at time $t + \Delta t/2$ by $\left(A_Z(t + \Delta t) + A_Z(t)\right)/2$.

In step 03, we calculate the Kohn-Sham Hamiltonian and the electric current at time $t + \Delta t$ from the Bloch orbitals $u_{bk,Z}(r, t + \Delta t)$. The updated Kohn-Sham Hamiltonian will be used to evolve the Bloch orbitals, and the current will be used to evolve the vector potential.

By repeating the steps 01-03, the coupled equations of the macroscopic Maxwell's equation (2.55) and the microscopic time-dependent Kohn-Sham equation (2.56) can be solved simultaneously.
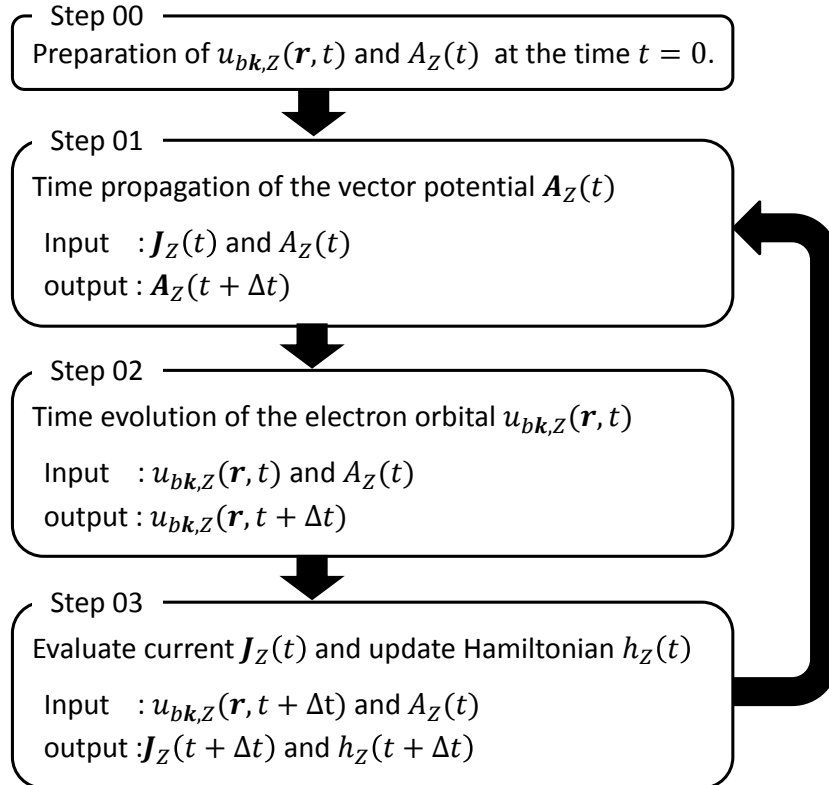


Figure 3.5: Flowchart of the multi-scale simulation.

## 3.6  Parallelization of the multi-scale simulation

The present multi-scale simulation can be very efficiently computed in massively parallel machines. To understand it and to illustrate our parallelization strategy in practice, we first illustrate computational aspects of our simulation, stressing exchange of data required to proceed the calculation. Figure 3.6 shows data flows among macroscopic grid points. Between macroscopic grid points $Z$ and $Z + \Delta Z$, exchange of the vector potential data is required to evolve it by Eq. (3.15). There are mutual data flows between macroscopic and microscopic levels: the vector potential $\boldsymbol{A}_Z(t)$ is an input to solve the time-dependent Kohn-Sham equation (2.56) in the microscopic level. The macroscopic current $J_Z(t)$ is calculated in the microscopic level and transferred to the macroscopic level. This is an input to solve the Maxwell's equation (3.15). We note that there is no direct exchange of data between electron orbitals belonging to different macroscopic grid points.
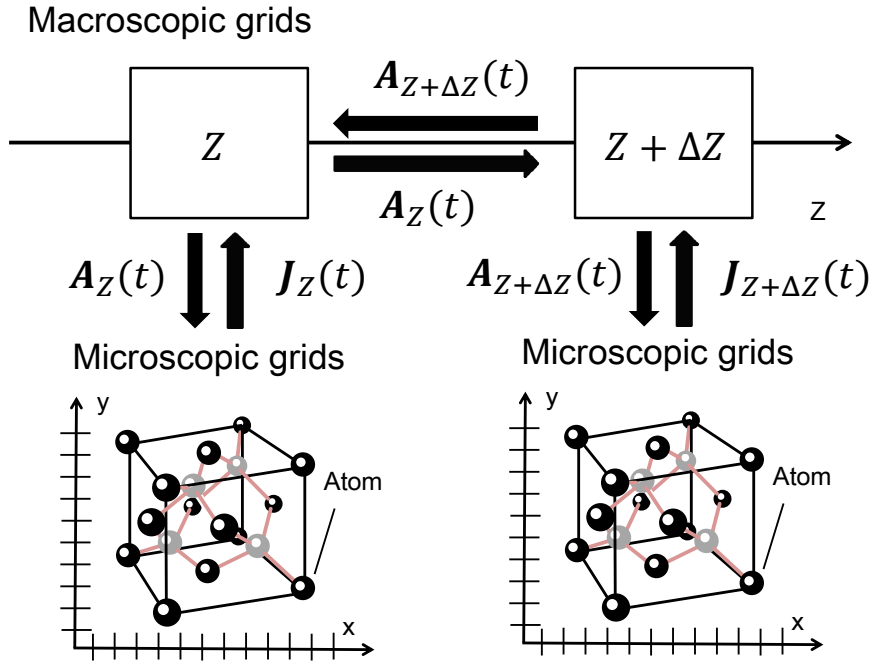


Figure 3.6: A schematic picture showing connections among grid systems. At each macroscopic gird points, the vector potential, $\boldsymbol{A}_Z(t)$, and electric current, $\boldsymbol{J}_Z(t)$, are exchanged between macroscopic and microscopic scales. The macroscopic grid points are connected to next neighbors by exchanging vector potentials, $\boldsymbol{A}_{Z\pm\Delta Z}(t)$.

In the practical implementation using MPI, we assign a communicator to each macroscopic grid point. The number of the communicators is equal to the number of macroscopic grid points. In principle, each communicator only need to have data of vector potential $A_Z(t)$ and current $J_Z(t)$ of the corresponding macroscopic grid point. In evolving the vector potential using Eq. (3.15), we need data of vector potential of nearest neighbor macroscopic grid points that requires point-to-point communication between communicators. In the present implementation of ARTED, however, data of vector potential and current of all macroscopic grid points are shared among all the communicators.

Then the macroscopic Maxwell's equation (3.15) is redundantly solved in all the communicators. This redundancy does not harm computational performance because the one-dimensional Maxwell solver part is negligible in the total computational cost.

In addition to the macroscopic grid points, calculations of microscopic level, the time evolution of the time-dependent Kohn-Sham equation, can also be very efficiently parallelized (see Sec. 3.4). There are two indices of the electron orbitals $u_{bk,Z}(r,t)$ that are also suitable for parallelization: One is the band index $b$ and the other is the $k$-point. Compared with the parallelization in $Z$, there arise communications if we parallelize over indices $b$ and $k$. At each time step, we need to sum up electron orbitals over $b$ and $k$ to calculate density (current density, kinetic energy density if necessary), and current. The density (current density, kinetic energy density if necessary) is used to construct the time-dependent Hamiltonian and the current is the basic output of the microscopic calculation. These communications can be achieved as collective communications inside the communicator of each macroscopic grid point.

Figure 3.7 shows a schematic picture for the parallelization of the multi-scale simulation in ARTED. In our present implementation, we can parallelize with MPI for macroscopic grid points $Z$ and $k$-points $k$. We can also parallelize in hybrid way using both MPI and OpenMP: $Z$ and $k$ are parallelized with MPI, while $k$ and band index $b$ are parallelized with OpenMP.
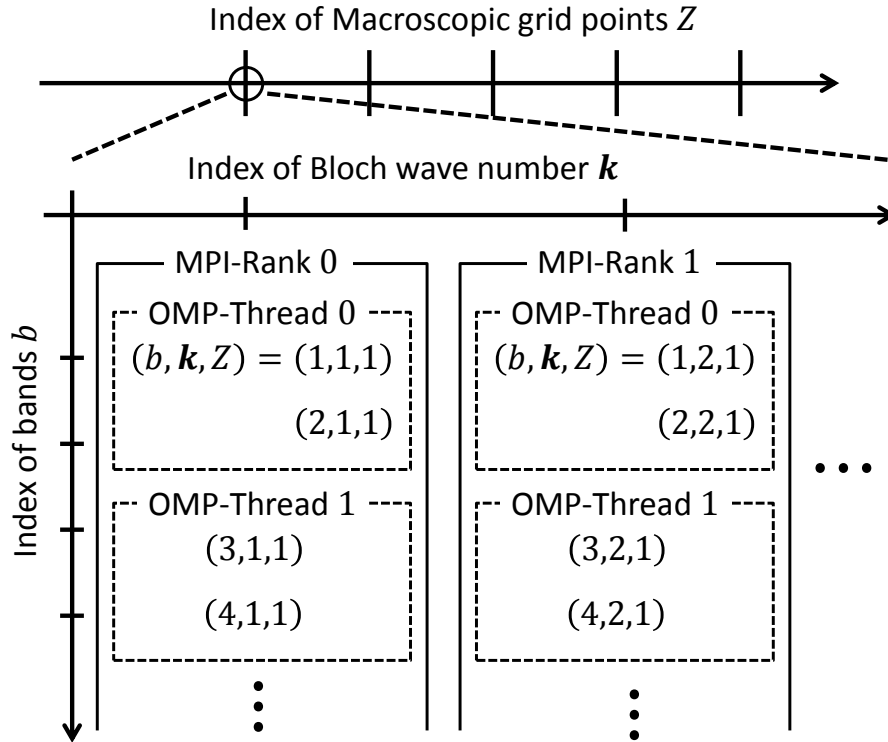


Figure 3.7: A Schematic picture of the parallelization of the multi-scale simulation in ARTED. There are three quantities $(bk, Z)$ that are indices of electron orbitals $u_{bk,Z}(r,t)$ and are subject to be parallelized.

## 3.7 Computational performance of the multi-scale simulation

Figure 3.8 shows a strong-scaling parallel efficiency of ARTED at K-computer. The data is taken for an irradiation of a laser pulse on bulk silicon. The number of macroscopic grid points is 160, the electron orbitals at each macroscopic grid point has 1152 $k$-points and 16 bands. When using 92160 cores, calculation is conducted by hybrid parallelization using 11520 MPI process times 8 OpenMP threads. Each thread takes care of 32 orbitals. As seen from Fig.3.8, ARTED shows a good parallel efficiently, more than 90 % between 7680 and 92160 cores. This good efficiency reflects the fact that communication costs of our code is rather small even for a job using about 100,000 cores.

Let us remind of communications involved in the multi-scale calculation. As mentioned previously, we calculate propagation of the macroscopic vector potential $\boldsymbol{A}_Z(t)$ redundantly at every MPI processes. This requires an all-to-all communication of the current $\boldsymbol{J}_Z(t)$ at each time step. Since this is a rather small array of typically dozens of kB, it does not cost much. Inside each communicator, there is a all-to-all communication to calculate density and current from electron orbitals. The size of this communication depends on the number of bands $b$, $k$-points, and the number of microscopic grid points for coordinate $\boldsymbol{r}$. However, it is independent of the number of macroscopic grid points for $Z$. Therefore, once a material to be calculated is set, the communication cost does not increase even if we increase the number of macroscopic grid points.

Figure 3.9 shows computing performance of ARTED. It is about 20% for cores from 7680 to 92160. In our calculation, the most time-consuming part is the operation of the single-particle Hamiltonian, $h_Z(t)$, on electron orbitals, $u_{b\boldsymbol{k},Z}(\boldsymbol{r},t)$ and it corresponds to an operation of a sparse Hermitian matrix on a complex vector. This operation can be achieved independently for all indices of $Z$, $\boldsymbol{k}$-points, and $b$. Therefore, the computational performance does not depend on the way to parallelize, as verified in the figure.
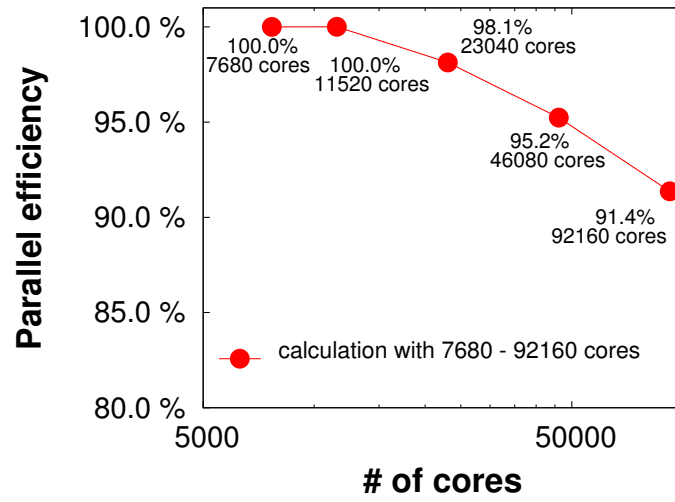
Figure 3.8: The strong-scaling parallel efficiency of ARTED at K-computer.
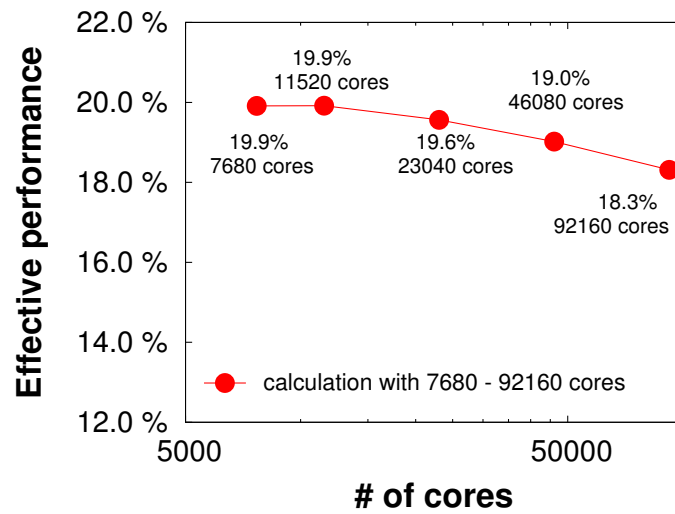


Figure 3.9: The computing performance of ARTED at K-computer.

# Chapter 4

# Electron Dynamics in Crystalline Solids

## 4.1  Introduction

At current frontiers of optical sciences, interactions of intense ultra-short laser pulses with solids have been intensively studied [11, 35, 37, 41, 54]. If the intensity of an ultra-short laser pulse exceeds a critical threshold of materials, the laser pulse bring an irreversible change to the materials through a non-equilibrium phase where the electron-temperature is much higher than the lattice temperature. This kind of irreversible phenomena can be applied to *non-thermal laser-processing* [35, 41]. The non-thermal laser-processing has been attracting much interest as a candidate of novel processing technique. In contrast, if the intensity of an ultra-short laser pulse is close to but below the damage threshold, the laser pulse may induce strongly-nonlinear reversible phenomena. For example, an ultrafast charge transfer has been induced by high-intensity ultra-short laser pulses even in a insulator in this reversible condition [56]. Moreover, ultrafast modulation of optical properties of dielectrics [53] and ultrafast band-gap dynamics [57] have been observed in the time domain. Such ultrafast reversible nonlinear phenomena would be useful for future applications of optoelectronic devices.

Theoretical investigations of these phenomena based on the first-principles calculations is quite significant to understand the microscopic mechanism of the phenomena since microscopic information of electron dynamics in a nanometer scale is difficult to extract from experiments and phenomenological models. The time-dependent density functional theory (TDDFT) is a candidate of possible theories to investigate electron dynamics in solids from the first-principles level [76]. One strong point of the TDDFT is its applicability for real-time calculations: One may directly solve the time-dependent Kohn-Sham equation in the time domain even for three-dimensional realistic systems with moderate computational costs. The real-time calculations enable us to investigate strongly-nonlinear electron dynamics induced by high-intensity ultra-short laser pulses since the calculations do not require any perturbative expansions for the strength of external fields. Indeed, the real-time TDDFT calculations for solid-state systems have been applied to investigate several nonlinear phenomena such as dielectric breakdown [97], coherent phonon generation [98, 99], and calculation of nonlinear optical properties [120], as well as linear responses of materials [96].

In order to apply the TDDFT to practical problems, it is necessary to approximate exchange-correlation potentials. So far, the adiabatic local density approximation (LDA) has only been employed in the real-time TDDFT calculations for solids. However, the adiabatic LDA has a serious problem

in calculations of light-matter interactions: The adiabatic LDA tends to under estimate optical gaps of dielectrics. This optical-gap problem is closely related to the well-known band-gap problem of the LDA in the static density functional theory (DFT) calculations. The optical gap is a crucial quantity to investigate nonlinear electron dynamics induced by intense laser pulses since it determines the order of perturbation that permits electronic excitation in the multi-photon picture. Moreover, the optical gap comes directly in the famous Keldysh formula of electronic excitations in solids [121] and largely affects the electronic excitation rate. Thus, it is difficult to quantitatively investigate light-matter interactions based on the adiabatic LDA. It often provides even qualitatively incorrect description for electronic excitations. In order to quantitatively investigate nonlinear light-matter interactions, an exchange-correlation potential that improve the description of optical gaps is highly desired.

Recently, Tran and Blaha have proposed a meta generalized-gradient approximation (meta-GGA) exchange potential, which systematically improves the band gap energy of various materials [103]. We abbreviate the potential as TB-mBJ potential. Calculated band gap energies using the TB-mBJ potential agree with experimental gap energies in a quality similar to those by the $GW$ method [103]. In this chapter, we develop theoretical and numerical methods to employ the TB-mBJ potential in the real-time TDDFT calculation, in order to improve accuracy and reliability of the calculations. To carry out stable time-evolution calculations, we find that a predictor-corrector step is indispensable in the calculations using the TB-mBJ potential, while it is not necessary in the calculations using the LDA potential. The TB-mBJ potential is directly defined without referring to the energy functional, and an explicit form of the energy functional providing the potential is not known. We discuss how to evaluate the electronic excitation energies during the irradiation of a laser pulse without referring to the energy functional.

We illustrate the real-time electron dynamics calculations in both linear and nonlinear responses, as well as the ground state calculations, employing the TB-mBJ and the LDA potentials. For the illustration, we take crystalline silicon and germanium as examples. However, our theoretical and numerical treatments are applicable not only to semiconductors but also to insulators and metals. We compare the results using the TB-mBJ and the LDA potentials and investigate the difference.

## 4.2 Properties of ground state

We first illustrate the ground-state calculation, taking a crystalline silicon as an example. The ground-state calculation is necessary to conduct the real-time TDDFT calculation since it gives the initial Bloch orbitals for electron dynamics calculations. As mentioned above, we employ the two exchange-correlation potentials: the LDA and the TB-mBJ potentials are described in Sec. 2.4.

The LDA potential tends to underestimate band gap energies of dielectrics. For example, in our LDA calculation, the band gap of silicon is 0.49 eV, which is much lower than the experimental gap, 1.17 eV [122]. The under estimation of the band gap is closely related to the optical-gap underestimation which often causes serious problems in the real-time TDDFT calculation.

The TB-mBJ potential has been developed to improve the description of band gap energies of dielectrics [103]. The potential includes a parameter $c_m$ to which the band gap is sensitive [112]. Figure 4.1 shows $c_m$-parameter dependence of the Kohn-Sham band gap of silicon, which is the energy difference of the highest single particle energy in the valence bands and the lowest energy in the conduction bands. Red circle shows the calculated gaps using the TB-mBJ potential with different $c_m$ parameters. The experimental band gap of crystalline silicon, 1.17 eV, is also shown as black solid line. As seen from the figure, the Kohn-Sham band gap much depends on the $c_m$ parameter. The gap changes from 0.1 eV to 1.8 eV, while the $c_m$-parameter changes from 0.7 to 1.2.
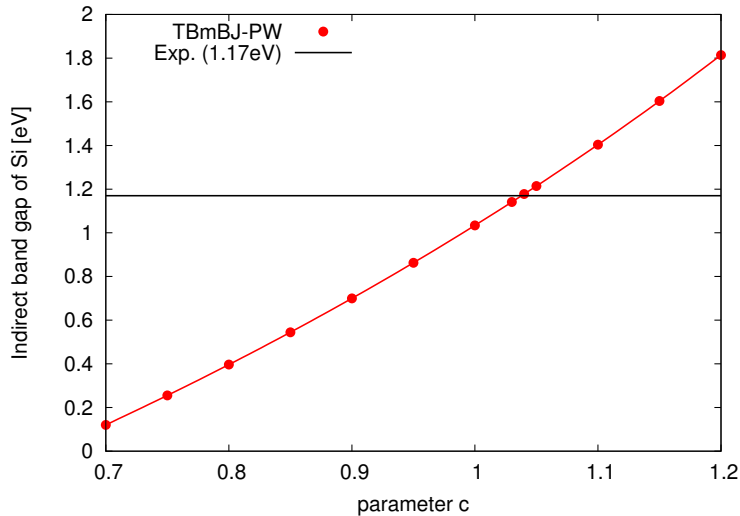


Figure 4.1: The band gap energy of crystalline silicon as a function of the $c_m$-parameter in the TB-mBJ potential.

In the original paper of the potential, a formula to define the $c_m$-parameter has been proposed [103]. In this study, we pragmatically choose the $c_m$-parameter so that the Kohn-Sham gap coincides with the experimental band gap: We set the $c_m$-parameter to $c_m = 1.04$ for the silicon case. As we will see later, if we choose the $c_m$-parameter so as to reproduce the experimental band gap in the static DFT calculation, the optical gap is also well reproduced in the TDDFT calculation.

Figure 4.2 shows the band structure of crystalline silicon. Red-solid line shows the result using the TB-mBJ potential, and green-dashed line shows that using the LDA. One sees that the calculated valence bands using the TB-mBJ potential almost coincide with those using the LDA potential. In

contrast, the calculated conduction bands using the TB-mBJ potential are simply pushed up to the higher energy direction, compared with those using the LDA potential. As a result of this behavior, the band-gap of silicon is improved by the TB-mBJ potential. As will be shown later, the dielectric function is also improved.
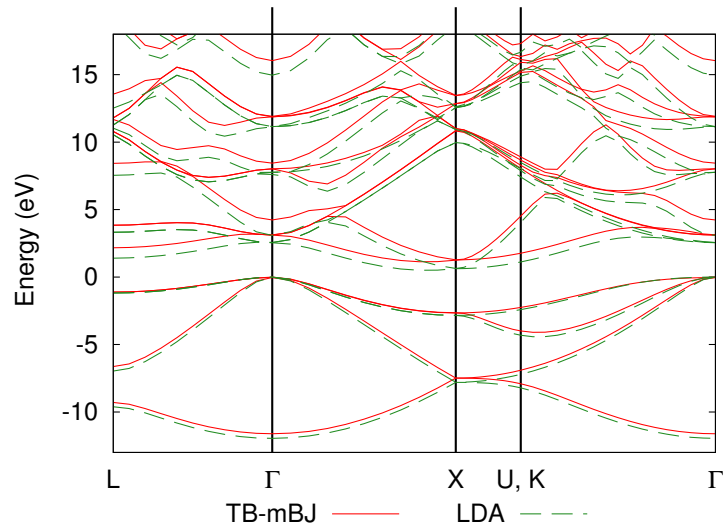


Figure 4.2: Calculated band structure of crystalline silicon. The energy of the valence top is set to 0 eV. Red-solid line shows the result of the TB-mBJ potential, and green-dashed line shows the result of the LDA.

## 4.3 Lineaer-response calculation for solids

In this section and Sec. 4.4, we apply the real-time TDDFT calculations for electron dynamics in crystalline silicon and germanium using the TB-mBJ and the LDA potentials. We choose a cubic unit cell for both silicon and germanium, containing eight atoms with 32 valence electrons. We treat only four valence electrons for each atom, employing a norm conserving pseudo-potential [107], with a separable approximation [108]. The unit cell is discretized by $16^3$ uniform grid points for silicon, and by $24^3$ uniform grid points for germanium. The first Brillouin zone is discretized by $24^3$ $k$-points for both crystals.

Although linear response properties of solids may be investigated either in frequency or in time domains, the time-domain calculation is a unique option for strongly nonlinear dynamics induced by high-intensity ultra-short laser pulses. In this section, we discuss a real-time calculation for a dielectric function of silicon. The purpose of this section is to demonstrate that numerical methods of time evolution calculations presented in Chap. 2 work stably in real-time linear-response calculations.

First, we numerically demonstrate the necessity of the predictor-corrector procedure in the real-time TDDFT calculation with the TB-mBJ potential (see Sec. 3.2.2). Figure 4.3 shows the electric current in the crystalline silicon as a function of time after an instantaneous weak distortion is applied at $t = 0$. A time step of $\Delta t = 0.04$ a.u. is used. Figure 4.3 (a) shows the electric current using the LDA potential, and (b) shows the electric current using the TB-mBJ potential. In both panels, red-solid lines show results using the predictor-corrector procedure, while green-dashed lines show results without using the predictor-corrector procedure. One sees that, while the calculations using the LDA potential give the same result regardless of whether the predictor-corrector procedure is used, the calculations using the TB-mBJ potential proceed stably only if the predictor-corrector step is used. Until $t = 0.8$ fs (about 800 time steps), the calculated electric currents with and without the predictor-corrector procedure coincide with each other. However, at $t = 0.8$ fs, the calculation without the predictor-corrector procedure starts to show unphysical oscillations. We carried out calculations with and without the predictor-corrector procedure for several time steps, $\Delta t = 0.02, 0.04$, and $0.08$ a.u., and have found that results without the predictor-corrector procedure always fail showing unphysical oscillations after a certain number of iterations. Calculations using the predictor-corrector procedure give the same result for the three time steps. We thus conclude that the predictor-corrector procedure is indispensable for stable time-evolution of orbitals when using the TB-mBJ potential. In the calculations presented below, we use the predictor-corrector procedure when the TB-mBJ potential is used, while we do not when the LDA potential is used.

We then move to calculations of dielectric functions in real-time. For dielectric functions, several *ab-initio* approaches have been developed. Among them, the $GW$ plus Bethe-Salpeter equation approach [64, 65], which is based on many-body perturbation theory, has been successful to describe dielectric functions of various materials quantitatively. *Ab-initio* calculations based on TDDFT have also been presented [82]. Recently, dielectric functions in the TDDFT have been reported using meta-GGA [123] and HSE [124] functionals, which are successful in describing band gap energies of various materials correctly.

We briefly explain how we calculate dielectric function as a function of frequency in the real-time TDDFT calculations. We calculate time evolution of electron orbitals under a weak electric field, $\boldsymbol{E}(t) = -\frac{1}{c}\frac{\partial}{\partial t}\boldsymbol{A}(t)$, solving Eq. (2.47). Using electric conductivity $\sigma_{ij}(t)$, the spatially-averaged
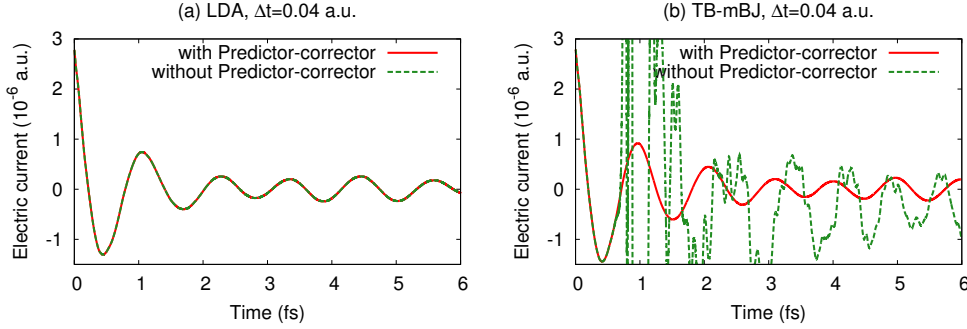
Figure 4.3: Electric currents as functions of time after an instantaneous weak distortion is applied at $t = 0$. Panel (a) shows the results using the LDA potential, and panel (b) shows the results using the TB-mBJ potential. In both panels, calculated results with (red-solid) and without (green-dashed) the predictor-corrector procedure are compared.

electric current $\boldsymbol{J}(t)$, which is given by Eq. (2.51), is related to the electric field $\boldsymbol{E}(t)$ by

$$J_i(t) = \sum_j \int dt' \sigma_{ij}(t - t') E_j(t'), \tag{4.1}$$

where $i$ and $j$ indicate Cartesian component, $i, j = x, y, z$. Taking Fourier transformations of both sides, we obtain a relation in frequency representation,

$$J_i(\omega) = \sum_j \sigma_{ij}(\omega) E_j(\omega), \tag{4.2}$$

where $E_i(\omega)$, $J_i(\omega)$, and $\sigma_{ij}(\omega)$ are Fourier transformations of $E_i(t)$, $J_i(t)$, and $\sigma_{ij}(t)$, respectively. Frequency-dependent dielectric function $\epsilon_{ij}(\omega)$ is related to $\sigma_{ij}(\omega)$ as usual,

$$\epsilon_{ij}(\omega) = \delta_{ij} + \frac{4\pi i}{\omega} \sigma_{ij}(\omega). \tag{4.3}$$

In principle, we may use any weak electronic fields $E_i(t)$ to calculate $\sigma_{ij}(\omega)$. For numerical convenience, we employ a $\delta$-type distortion in $z$-direction for the electric field, $\boldsymbol{E}(t) = s\boldsymbol{e}_z \delta(t)$ where $s$ is a small parameter. Then the conductivity is proportional to the electric current, $\sigma_{zz}(t) = J_z(t)/s$. This relation tells us that the Fourier transformation of the electric current provides the frequency-dependent conductivity. To reduce numerical noises caused by the finite evolution time $T$, we use a mask function $M(x)$ in the Fourier transformation as follows,

$$\sigma_{zz}(\omega) = \frac{1}{s} \int_0^T dt J_z(t) e^{i\omega t} M(t/T). \tag{4.4}$$

In practice, we employ the mask function $M(x) = 1 - 3x^2 + 2x^3$ [125].

Figure 4.4 shows electric currents $J_z(t)$ in crystalline silicon as functions of time after the delta-function distortion is applied at $t = 0$. Red-solid line shows the result using the TB-mBJ potential, and green-dashed line shows the result using the LDA potential. Both currents accurately coincide with each other at $t = 0$, since the initial current is determined by the sum rule [96]. Shortly after

the distortion (0 fs to 1 fs), both currents look similar to each other. They start to depart after a few femtoseconds. As discussed above, the electric current is proportional to the conductivity as a function of time when we employ the delta-type distortion. Therefore, the difference of the currents directly reflects the difference of the conductivities.
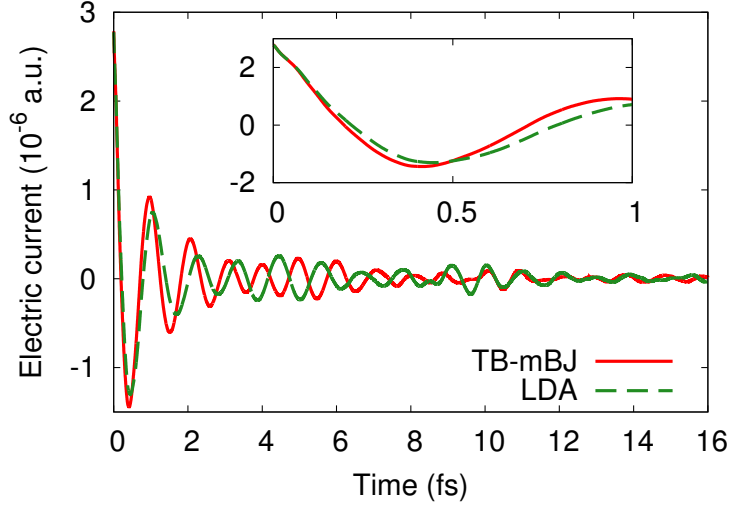


Figure 4.4: Electric currents in crystalline silicon as functions of time after an impulsive distortion is applied at time $t = 0$. Results using the two exchange-correlation potentials are compared: TB-mBJ (red-solid), and LDA (green-dashed).

From the currents shown in Fig. 4.4, dielectric functions can be calculated using Eqs. (4.3) and (4.4). Figure 4.5 shows dielectric functions of silicon: the real part in (a) and the imaginary part in (b). Red-solid line shows the result using the TB-mBJ potential, and green-dashed line shows the result using the LDA potential. A result of $GW$ plus Bethe-Salpeter equation approach [64] is shown as gray dash-dot line, and an experimental result [126] is shown as black dotted line.

As seen from Fig.4.5 (b), the optical gap is underestimated when the LDA potential is used. This is closely related to the well-known band gap problem of the LDA. In contrast, the optical gap is well reproduced when we use the TB-mBJ potential. The real parts of the dielectric functions calculated using the TB-mBJ potential also reproduce accurately the experimental values in low frequency region (below 3 eV). One sees that while the imaginary parts of the experimental and the $GW$+BSE results show a peak structure around 3.2 eV, the result of the TB-mBJ potential does not. This fact clearly indicates that the adiabatic TB-mBJ potential does not include excitonic effects.

Figure 4.6 shows dielectric functions of germanium: the real part in (a) and the imaginary part in (b). Red-solid line shows the result using the TB-mBJ potential, green-dashed line shows the result using the LDA potential, and black-dotted line shows an experimental result. A naive calculation using Eq. (4.4) results in a divergent behavior at low frequency, because of the division by frequency $\omega$ in Eq. (4.3). We remedy it by removing a constant component of the current. One sees that the TB-mBJ result shows fair agreement with the experimental result in a wide frequency region, much better than the case of silicon. This may indicates that exciton effects are not so significant in germanium. The LDA result is shifted to the low energy direction compared with the TB-mBJ result.
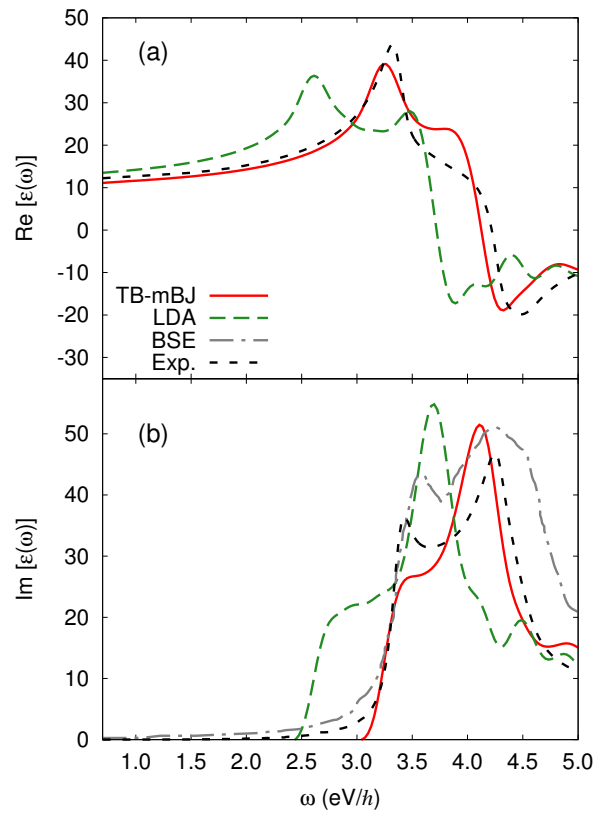
Figure 4.5: Dielectric functions of silicon; real part in (a) and imaginary part in (b). Results using the three exchange-correlation potentials are compared: HSE (red-solid), TB-mBJ (green-dashed), and LDA (blue-dotted). The result of $GW$ plus Bether-Salpeter equation approach is shown by gray dash-dot-dot line [65]. An experimental result [126] is also shown as black-dotted lines.
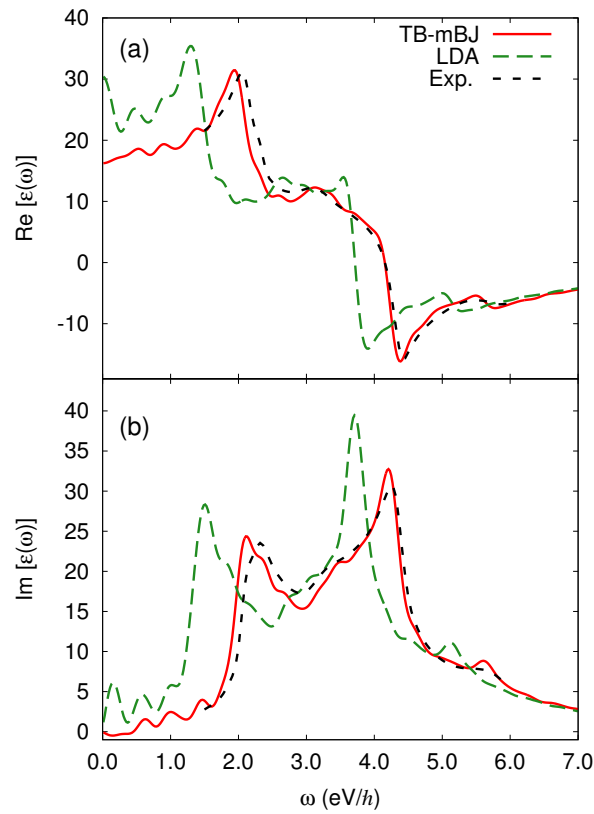
Figure 4.6: Dielectric functions of germanium; real part in (a) and imaginary part in (b). Results using the two exchange-correlation potentials are compared: TB-mBJ (red-solid) and LDA (green-dashed). An experimental result [127] is also shown as black-dash-dotted lines.

## 4.4  Nonlinear Electron dynamics under an pulse field

We next move to the electron dynamics calculation in the nonlinear regime. Our theoretical framework is applicable not only to linear responses but also to nonlinear responses since we do not have any assumption for the external field but just directly solve the time-dependent Kohn-Sham equation (2.47).

In this section, we investigate nonlinear electron dynamics in crystalline silicon and germanium under intense ultra-short laser pulses using the TB-mBJ and LDA exchange-correlation potentials. We employ electric fields derived from the following vector potential,

$$A(t) = \begin{cases} -\frac{cE_0}{\omega} \cos(\omega t) \sin^2(\frac{\pi}{T_d} t) & (0 < t < T_d) \\ 0 & \text{(otherwise)}, \end{cases} \tag{4.5}$$

where $\omega$ is a mean frequency of the field, $T_d$ is the pulse duration, and $E_0$ is the maximum electric field of the pulse. We set $\omega$ and $T_d$ to 1.35 eV/$\hbar$ and 16 fs, respectively. We define the maximum intensity of the laser pulse $I_0$ as $I_0 = cE_0^2/8\pi$. We calculate electron dynamics changing the intensity $I_0$. We will examine two physical quantities: the excitation energy during and after the laser irradiation, and the number density of excited electrons after the laser irradiation.

### 4.4.1  Excitation energy

We first consider electronic excitation energy induced by laser irradiation. The excitation energy is one of the most important quantities to investigate light-matter interactions. For example, optical damage thresholds can be estimated by comparing the electronic excitation energy with cohesive energy of solids [128, 129]. Although the LDA potential is explicitly derived from the energy functional, the TB-mBJ potential is not derived from any functionals but given directly. It is even unclear whether there exists an energy functional that provides the TB-mBJ potential. We first discuss how to evaluate electronic excitation energy when we use the TB-mBJ potential. We then investigate differences in electronic excitation energies using the TB-mBJ and the LDA potentials.

We first note that there are two procedures to calculate electronic excitation energy which should give the same result if the exchange-correlation potential is derived from an energy functional. One is to use the explicit expression of the energy functional given by

$$\begin{aligned} E_{ex}(t) &= \sum_i \int_\Omega d\boldsymbol{r} \psi_i^*(\boldsymbol{r}, t) \left[ \frac{(-i\hbar\nabla + \frac{e}{c}\boldsymbol{A}(t))^2}{2m} + \hat{v}_{ion}[\boldsymbol{A}(t)] \right] \psi_i(\boldsymbol{r}, t) \\ &+ \frac{1}{2} \int d\boldsymbol{r} v_H(\boldsymbol{r}, t)\rho(\boldsymbol{r}, t) + E_{xc}[\{\psi_i(\boldsymbol{r}, t)\}] - E_{GS}, \end{aligned} \tag{4.6}$$

where $E_{xc}$ is the exchange-correlation energy functional and $E_{GS}$ is the energy of the ground state. The other is to calculate the work done on electrons by the external electric field,

$$W(t) = \int_{-\infty}^t dt' \boldsymbol{J}(t') \cdot \boldsymbol{E}(t'), \tag{4.7}$$

where $\boldsymbol{J}(t)$ is the electric current defined by Eq. (2.51). When the exchange-correlation potential is derived from the energy functional $E_{ex}[\{\psi_i(\boldsymbol{r}, t)\}]$, we may easily prove that there holds

$$W(t) = \int_{-\infty}^t dt' \frac{d}{dt'} E_{ex}(t') = E_{ex}(t). \tag{4.8}$$

In calculations using the LDA potential, we may employ either Eq. (4.6) or Eq. (4.7). In calculations using the TB-mBJ potential, Eq. (4.7) is the unique option.

Although Eq. (4.6) and Eq. (4.7) are analytically equivalent to each other if the potential is derived from an energy functional, we have found that Eq. (4.6) is numerically more favorable when the applied laser pulse is weak. To show it, we compare excitation energies calculated by two expressions.

Figure 4.7 shows $E_{ex}(t)$ of Eq. (4.6) using the LDA potential as a function of time for two intensities, $I = 1.0 \times 10^{10}$ W/cm$^2$ in (a) and $I = 1.0 \times 10^{13}$ W/cm$^2$ in (b). In the panel (a), we find an appreciable excitation energy during irradiation of the laser pulse. However, at the end of the pulse, the system almost returns to the ground state since the laser frequency is lower than the direct band gap. We shall call it *virtual* excitation. If we calculate the excitation energy using Eq. (4.7), the integrand $\boldsymbol{J}(t) \cdot \boldsymbol{E}(t)$ behaves oscillatory during the irradiation of the laser pulse. The integration over time mostly cancels and gives the total work done by the laser pulse which is very small as seen from the panel (a). Therefore, the calculation using Eq. (4.7) may suffer from an accumulation of a numerical error during the time integral. Figure 4.7 (c) compares the electronic excitation energies after the weak laser pulse ends ($I_0 = 1.0 \times 10^{10}$ W/cm$^2$) using several different time steps $\Delta t$. Red up-pointing and green down-pointing triangles show the excitation energies calculated by Eq. (4.6) and by Eq. (4.7), respectively. As seen from the figure, results coincide numerically if we employ sufficiently small time step. The error in the excitation energy increases linearly with the time step $\Delta t$ when we employ Eq. (4.7).

When the laser pulse is so strong that electrons are substantially excited by the laser pulse, we find a steady increase of the excitation energy in time, as seen in Fig. 4.7 (b). We shall call it *real* excitation. In this case, the difference in the numerical calculation is very small between the calculations using Eqs. (4.6) and (4.7), even if we employ the largest time step, $\Delta t = 0.08$ a.u.

When we use the TB-mBJ potential, we can only evaluate excitation energy using Eq. (4.7). To obtain excitation energy, we carry out two calculations using different time steps, $\Delta t = 0.02$ a.u. and $\Delta t = 0.01$ a.u. We then estimate the converged excitation energy by a linear extrapolation using the two calculations.

Figure 4.8 shows electronic excitation energies as functions of time using the two exchange-correlation potentials; LDA and TB-mBJ. Figure 4.8 (a) shows results for a weak laser pulse ($I_0 = 1.0 \times 10^{11}$ W/cm$^2$), and Figure 4.8 (b) shows results for a strong laser pulse ($I_0 = 5.0 \times 10^{12}$ W/cm$^2$). Squared electric fields $E^2(t)$ are also shown as gray dash-dot lines in each panel. As seen from Fig. 4.8 (a), the electric field induces virtual excitation during the laser irradiation. After the irradiation ends, the excitation energy using the TB-mBJ potential returns to almost zero. In contrast, the excitation energy using the LDA potential remains finite after the irradiation, showing a substantial real excitation. These results indicate that wider optical gap in the calculations using the TB-mBJ potential suppresses the real excitation (see Fig. 4.5).

Figure 4.8 (b) shows that electronic excitation energies of silicon induced by the strong electric field persist even after the pulse ends irrespective of the exchange-correlation potentials. One sees that the excitation energy using the LDA potential is larger than that using the TB-mBJ potential. This is consistent with the above finding that the wider band gap suppresses the real excitation.

Next we investigate the electronic excitation energy after laser pulses end, changing the laser intensity $I_0$. Figure 4.9 shows excitation energies of silicon after the pulses end ($t = 19.3$ fs). Red down-pointing triangle shows the TB-mBJ result, and green up-pointing triangle shows the LDA result. Lines of cubed and squared intensity of the laser pulses are also shown as black-solid and gray-dashed lines, respectively. These lines are normalized at low intensity to coincide with the excitation
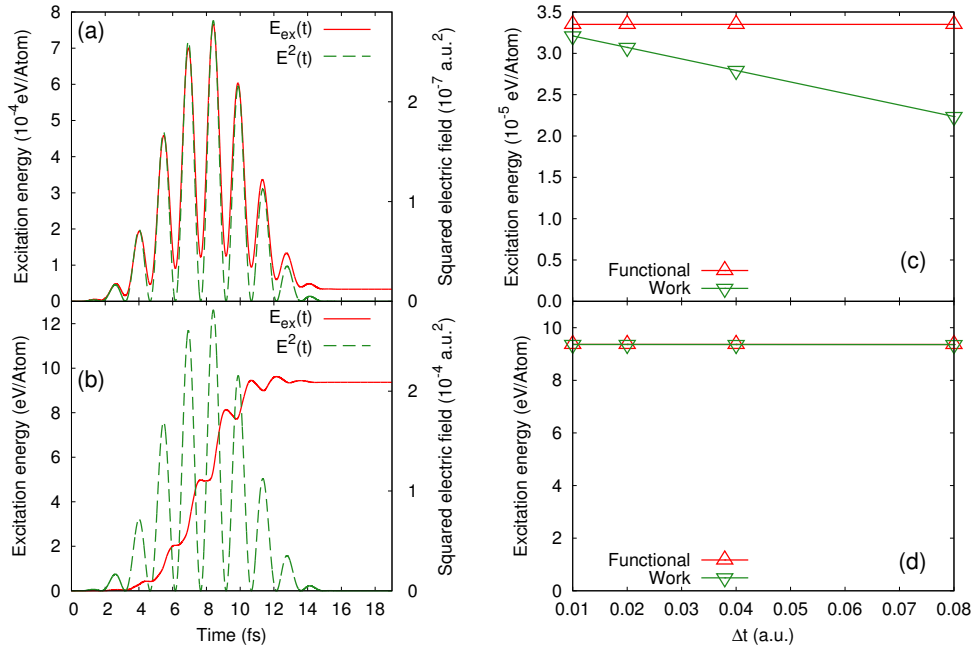
Figure 4.7: Laser-induced electronic excitation energy calculated using the LDA potential. Panels (a) and (b) show the electronic excitation energy (red-solid) and the applied squared electric field (green-dashed) as functions of time. Panels (c) and (d) show the electronic excitation energy after the laser irradiation ends using Eqs. (4.6) and (4.7). Results in the panels (a) and (c) are for the irradiation of the weak laser pulse ($I_0 = 1.0 \times 10^{10} \mathrm{W/cm^2}$), while results in the panels (b) and (d) are for the irradiation of the strong laser pulse ($I_0 = 1.0 \times 10^{13} \mathrm{W/cm^2}$).

energies. Black horizontal line shows the cohesive energy of silicon, 4.62eV/atom [130], which may be regarded as a reference of the damage threshold.

Multi-photon excitations are expected for weaker intensities, while tunneling excitations are expected for stronger intensities [121]. At low intensity region, the excitation energy using the LDA potential can be fit with the squared intensity line $I_0^2$, while the excitation energies calculated using the TB-mBJ potential can be fit with the cubed intensity line $I_0^3$. These behaviors indicate that two and three-photon absorption processes take place at the low intensity region for the LDA and the TB-mBJ cases, respectively. The numbers of absorbed photons are consistent with the ratio of the photon energy of the laser pulse ($\hbar\omega = 1.35$ eV) to the optical gap: the optical gap of silicon is 2.5 eV in the LDA case, and it is 3.1 eV in the TB-mBJ case (see Fig. 4.5).

One sees that the excitation energy using the LDA potential is much higher than the excitation energy using the TB-mBJ potential at low intensity region. In contrast, the difference of the excitation energies becomes relatively small at high intensity region close to the cohesive energy of the medium.

Figure 4.10 shows excitation energies of germanium after the pulses end. Red down-pointing triangle shows the TB-mBJ result, and green up-pointing triangle shows the LDA result. Black-solid and gray-dashed lines are proportional to laser intensity, normalized to coincide with the calculated excitation energies at the lowest intensity. Black horizontal line indicates the cohesive energy of
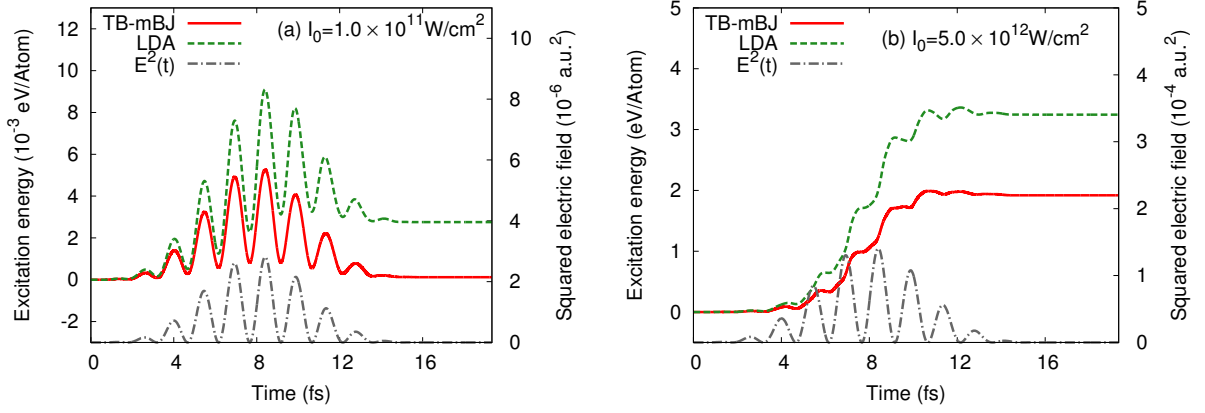
Figure 4.8: Electronic excitation energies of silicon as functions of time induced by laser irradiation. Panel (a) shows the excitation energy under irradiation of a weak laser pulse ($I_0 = 1.0 \times 10^{11}$ W/cm$^2$), while panel (b) shows that of a strong laser pulse ($I_0 = 5.0 \times 10^{12}$ W/cm$^2$). Results using the three exchange-correlation potentials are compared: HSE (red-solid), TB-mBJ (green-dashed), and LDA (blue-dotted). Squared electric fields are also shown as gray-dash-dotted lines.

germanium, 3.85eV/atom [131], which is regarded as a reference of the damage threshold.

As seen from the figure, both the TB-mBJ and LDA results are proportional to laser intensity as expected: The average photon energy of the pulse, 1.35 eV, is above the optical gap of germanium, and excitations are dominated by one-photon absorption. Then, the excitation energy is determined by the imaginary part of the dielectric function when the field is weak. The large difference between the TB-mBJ and the LDA results at low intensity region reflects the difference of the imaginary parts of the dielectric function at around 1.35 eV in Fig. 4.6. When the field intensity becomes strong, both the TB-mBJ and the LDA results deviate from the one-photon absorption line, and the difference between them becomes smaller. These behaviors are similar to the findings seen in the excitation energy of silicon.
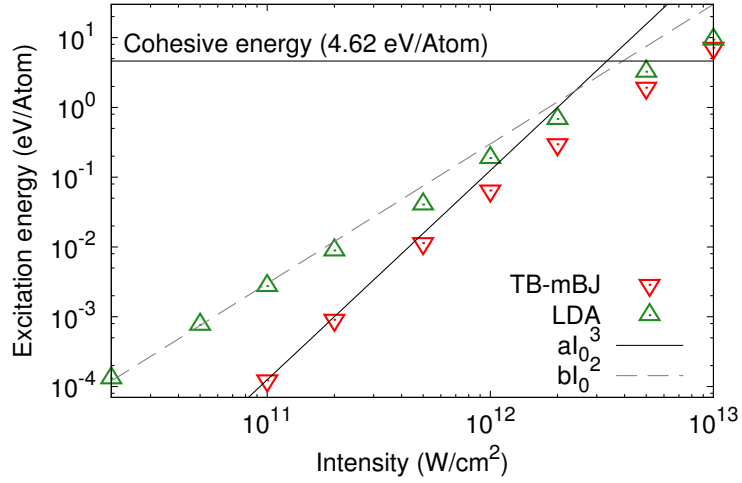
Figure 4.9: Excitation energies of silicon as functions of laser intensity calculated using the two exchange-correlation potentials: TB-mBJ (red down-pointing triangle) and LDA (green up-pointing triangle). Cubed and squared intensities normalized to the excitation energies at low intensity are also shown as black-solid and gray-dashed lines, respectively.
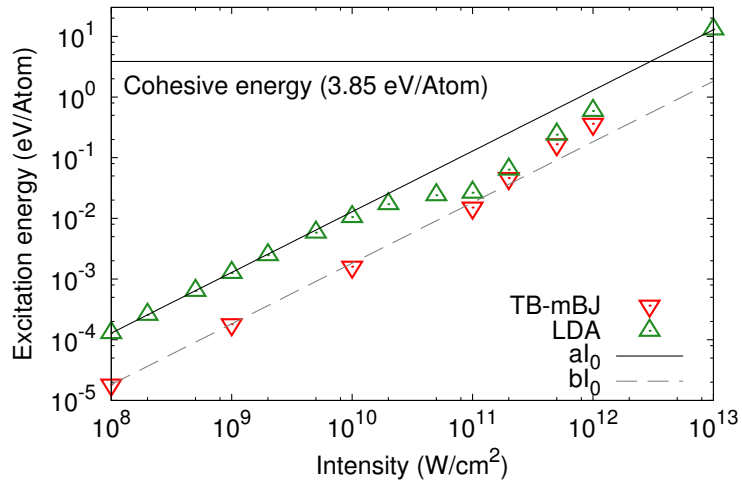


Figure 4.10: Excitation energies of germanium as functions of laser intensity calculated using the two exchange-correlation potentials: TB-mBJ (red down-pointing triangle), and LDA green up-pointing triangle). Black-solid and gray-dashed lines are proportional to the laser intensity.

### 4.4.2 Number density of excited electrons

The number density of excited electrons due to applied electric fields is one of significant observables to characterize laser excitation processes [101, 102]. To define the number density of excited electrons after laser irradiation, we first define eigenstates of the Kohn-Sham Hamiltonian after the laser pulse ends ($t_f = 19.3$fs),

$$h_{KS}(t_f)\phi_i(\boldsymbol{r}, t_f) = \epsilon_i^{t_f}\phi_i(\boldsymbol{r}, t_f). \tag{4.9}$$

Using these eigenstates, we define the number density of excited electrons $n_{ex}$ by,

$$n_{ex} = n_{elec} - \frac{1}{\Omega}\sum_{i,j=occupied}|\langle\phi_i(t_f)|\psi_j(t_f)\rangle|^2, \tag{4.10}$$

where $n_{elec}$ is the number density of valence electrons in the ground state, $\Omega$ is the volume of the unit cell, and $\psi_i(\boldsymbol{r}, t)$ are the time-dependent Kohn-Sham orbitals, which are solutions of Eq. (2.47). Only occupied states are summed in Eq. (4.10).

Figure 4.11 shows the number density of excited electrons of silicon as functions of laser intensity $I_0$. We find similar features to those seen in excitation energies shown in Fig. 4.9. The number density using the LDA potential is larger than that using the TB-mBJ potential. While the number density using the LDA potential is proportional to the squared intensity of laser pulse in the low intensity region, the number densities using the TB-mBJ potential are proportional to the cubed intensity. At high intensity region, the number densities of excited electrons using the two exchange-correlation potentials are similar to each other.
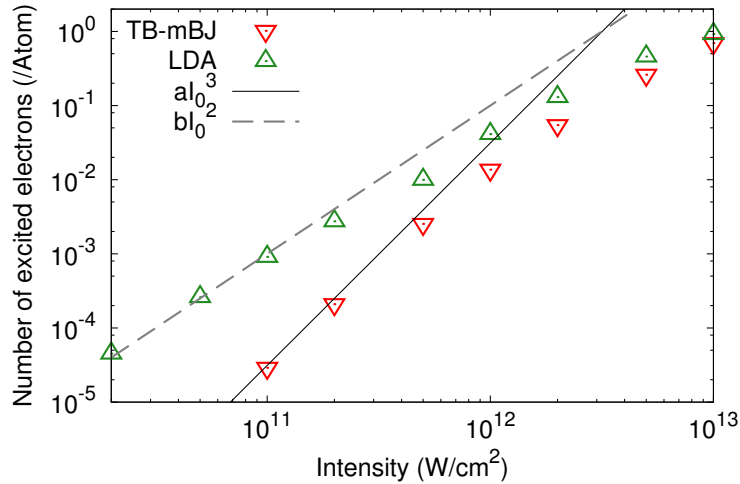


Figure 4.11: The number densities of excited electrons of silicon as functions of laser intensity calculated using the three exchange-correlation potentials: HSE (red down-pointing triangle), TB-mBJ (green up-pointing triangle), and LDA (blue square). Cubed and squared intensities normalized to the number densities of excited electrons at low intensity are also shown as black-solid and gray-dashed lines, respectively.

Figure 4.12 shows excitation energy per excited electron for silicon, namely, the excitation energy shown in Fig. 4.9 divided by the number of excited electrons shown in Fig. 4.11 as a function of laser intensity $I_0$. Twice and three times of the photon energy, 1.35 eV, are also shown by horizontal lines. At low intensity region, the excitation energy per excited electron using the TB-mBJ potential approaches to three times of the photon energy, $3 \times 1.35$ eV, while that using the LDA potential approaches twice of the photon energy, $2 \times 1.35$ eV. This fact obviously indicates that two and three-photon absorption processes dominate in the LDA case and the TB-mBJ case, respectively, and is consistent with the intensity dependences seen in Figs. 4.9 and 4.11.
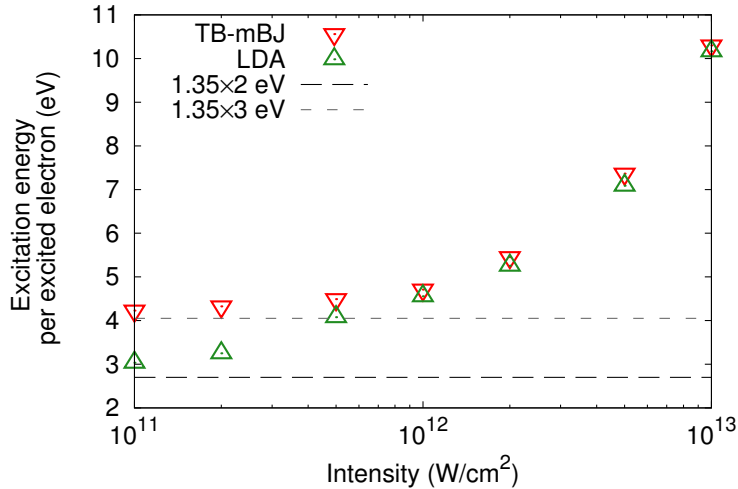


Figure 4.12: Excitation energy per excited electron in silicon is plotted against the laser intensity calculated using the three exchange-correlation potentials: HSE (red down-pointing triangle), TB-mBJ (green up-pointing triangle), and LDA (blue square). Two horizontal lines are shown at $2 \times 1.35$ (black-dashed) and $3 \times 1.35$ eV (gray-dotted).

## 4.5 Summary of electron dynamics in crystalline solids

In this chapter, we developed methods to carry out real-time TDDFT calculations using the TB-mBJ meta-GGA potential, which is known to reasonably reproduce band gap energies of insulators. To carry out stable time evolution of orbitals using the TB-mBJ potential, we find that the predictor-corrector procedure is indispensable. Without the predictor-corrector procedure, the electric current induced by an impulsive excitation shows unphysical oscillations after the time evolution of a few femtoseconds. This failure cannot be avoided even if we employ very small time step.

We examined electron dynamics using the TB-mBJ and LDA potentials. In linear response calculations, we investigated the dielectric response of crystalline silicon and germanium in the time domain. Calculated dielectric function using the TB-mBJ potential shows nice agreement with experimental results except an excitonic peak of silicon, while that using the LDA potential underestimates the optical gap. This clearly indicates that the TB-mBJ potential lacks the excitonic excitation effect. In electron dynamics calculations under intense ultra-short laser pulses, we investigated the excitation

energy and the number density of excited electrons during and after the laser irradiations. Since an explicit form of the energy functional corresponding to the TB-mBJ potential is not known, we developed a method to evaluate electronic excitation energy, not referring to the energy functional but computing the work done by the external field to electrons. For irradiation of weak laser pulses, the excitation energy and the number density of excited electrons of the LDA calculation are much larger than those of the TB-mBJ. For irradiation of strong laser pulses close to the damage threshold, we find that results are similar between the two potentials.

We consider the real-time TDDFT calculations using a modern exchange-correlation potential such as the TB-mBJ potential, which describe the band gap of dielectrics reasonably, will enable us to carry out quantitative description for electron dynamics in crystalline solids even under extremely nonlinear conditions. They are expected to provide significant insights and knowledge in wide fields of optical sciences including nonlinear optical responses, optical control of electrons, and laser processing in solids. In the following chapters, Chaps. 5,6 and 7, we employ the TB-mBJ potential in order to quantitatively investigate laser-induced nonlinear phenomena in dielectrics.

# Chapter 5

# Optical properties of highly laser-excited solids

## 5.1 Introduction

The interaction of high-intensity ultra-short laser pulses with solids is an important subject from both fundamental and technological points of view [11, 35, 37, 41, 54]. To investigate dynamics of electrons and phonons in real time, the pump-probe experimental technique has been extensively employed. One example of its use is creating coherent phonons and measuring their properties [132]. The vibration is detected by measuring the change of reflectance of the probe pulse. However, this technique requires a good understanding of the dielectric properties of the surface excited by the pump pulse. Another example is the energy deposited by strong laser pulses close to the damage threshold. They produce high-density electron-hole pairs at the surface of dielectrics, causing strong reflection for the probe pulse [101]. It is even now possible to measure the population of high-density electron-hole pairs in the time resolution less than a femtosecond [53, 56, 133]. However, the existing theory describing these effects is largely phenomenological. The dielectric properties of laser-excited material are often modeled with the Drude model [134–137], assuming that excited electrons behave like free carriers.

In this chapter, we apply the time-dependent density functional theory (TDDFT) to investigate optical properties of highly laser-excited dielectrics. Immediately after irradiation of high-intensity ultra-short laser pulses, a nonequilibrium phase is formed; only electrons are excited by the laser field, while atoms stays at their positions in the ground state because of their slow motion. We shall call it *electronic nonequilibrium phase*. After a few tens of femtosecond, a two-temperature phase is formed; excited electrons become hot electrons via electron-electron and electron-phonon collisions while lattice stays in much lower temperature. We shall call it *electronic thermal-equilibrium phase*. After several tens of picosecond, the system may become complete equilibrium phase, where electrons and lattice can be well described by the same temperature, through interactions between hot electrons and phonons. The complete equilibrium phase is out of the scope of this study.

In order to investigate the electronic nonequilibrium phase, we develop *numerical pump-probe experiments* in which the *experimental* pump-probe technique is mimicked by the real-time TDDFT calculation. In the numerical pump-probe experiments, we employ two kinds of laser pulses. One is a pump pulse which induces electronic excitation in dielectrics. The other is a probe pulse by which optical properties of the laser-excited dielectrics are extracted. If we apply the probe pulse immediately after the pump laser irradiation, we may extract the optical properties in the electronic

nonequilibrium phase. In principle, if the time delay between the pump and probe pulses are sufficiently large, the optical properties even in the electronic thermal-equilibrium phase could be extracted. However, the present real-time TDDFT calculation does not include electron-electron and electron-phonon collisions correctly. Therefore, the numerical pump-probe experiments are only valid before the times when electron-electron collisions have substantially affected the system (several tens of femtosecond). Therefore, an alternative method is required to investigate the electronic thermal-equilibrium phase. For this purpose, we develop a linear response calculation for the finite electron-temperature system described with the Fermi-Dirac function for electronic occupation factors.

We apply these methods to calculate optical properties of highly laser-excited silicon in both the electronic nonequilibrium and thermal-equilibrium phases based on the first principles description. We compare the simulated results with simple free-carrier models and explore validity and limitation of the models. We will find that many features of the response of the highly laser-excited dielectrics can be understood even at a quantitative level with the simpler treatments. However, there are also features that only appear in the full quantum mechanical simulations. We also compare the results between the electronic nonequilibrium and thermal-equilibrium phases and see how the thermalization affects the optical properties.

## 5.2 Nonequilibrium phase

In this section, we carry out what we call numerical pump-probe experiments to study the optical properties of the highly laser-excited dielectrics in the electronic nonequilibrium phase immediately after intense laser irradiation. We examine the electron dynamics in a unit cell of crystalline silicon irradiated by the pump and probe laser pulses. The current induced by the probe pulse will be used to investigate the optical properties of laser-excited silicon.

### 5.2.1 Calculation of electron dynamics

In order to describe the electron dynamics in crystalline silicon under laser fields, we solve the time-dependent Kohn-Sham equation (2.47) in the time domain. In this whole chapter, we employ the exchange-correlation potential proposed by Tran and Blaha [103] to reproduce optical gaps of materials.

We take the following form for the vector potential of the pump pulse in the medium $A_P(t)$,

$$A_P(t) = \begin{cases} -c\frac{E_0}{\omega_P}\cos(\omega_P t)\sin^2(\pi t/\tau_L) & (0 < t < \tau_L) \\ 0 & \text{(otherwise)}, \end{cases}$$

(5.1)

where $\omega_P$ and $\tau_L$ are the average frequency and the time length of the laser pulse, respectively. $E_0$ is the maximum electric field strength in the medium. This is related to the maximum intensity of the pulse $I$ by $I_v = cE_0^2/8\pi$ in the vacuum and $I_m = \epsilon^{1/2}cE_0^2/8\pi$ in the medium. Since the dielectric function $\epsilon$ is not well-defined in the presence of a strong electric field, we shall report our results using the field intensity corresponding to the vacuum relationship.

As described in Chap. 3, our computer code to solve the time-dependent Kohn-Sham equation uses a three-dimensional grid representation to represent orbital wave functions. The unit cell for the silicon crystal treated has a length $a = 10.26$ a.u. and contains eight Si atoms. The cubic unit cell is discretized into $16^3$ grid points. The four valence electrons of Si atoms beyond the closed (1s2s1p)

shells are treated dynamically. The $k$-space is also discretized into $24^3$ grid points. For the time evolution, we use a time step of $\Delta t = 0.08$ a.u. The number of time step is typically 24,000.

In Fig 5.1, we show an example of the calculated electron dynamics induced by the intense pump pulse. Here the frequency of the pump pulse is set to $\hbar\omega_P = 1.55$ eV and the duration of the pump pulse is $\tau_L = 18$ fs. These values will be used in all calculations of this chapter. For this figure, the maximum electric field strength $E_0$ corresponds to an intensity of $I = 1.0 \times 10^{12}$ W/cm$^2$.

Figure 5.1 (a) shows the time profile of the electric field, $E_P(t) = -\frac{1}{c}\frac{\partial}{\partial t}A_P(t)$, and the induced current, calculated using the time-dependent orbitals in Eq. (2.51). The average frequency $\hbar\omega = 1.55$ eV is smaller than the direct band gap energy (3.1 eV in the present calculation), so the initial current response is nondissipative since the field is sufficiently small. This is seen by the phase difference between the current and the electric field, which is shifted by $\pi/2$ at the beginning of the field pulse ($t < 5$ fs). As the intensity of the pulse increases, the system absorbs energy by the excitation of electron-hole pairs in the multiphoton absorption processes. As a result, the phase difference decreases. We also find a mixture of high frequency component in the current after the maximum of the electric field. Making a Fourier analysis, we find that it is dominated by frequencies around 4.2 eV/$\hbar$, slightly higher than the frequency of the optical band gap, 3.2 eV in the present calculation.

Figure 5.1 (b) shows the number density of excited electron-hole pairs per Si atom. To calculate it, we used Eqs. (4.9) and (4.10). From Fig. 5.1 (b), we find a rapid increase of the excited electrons during the field pulse. After the pulse ends, the number density is independent of time, showing that the present adiabatic framework does not include any recombination mechanisms.
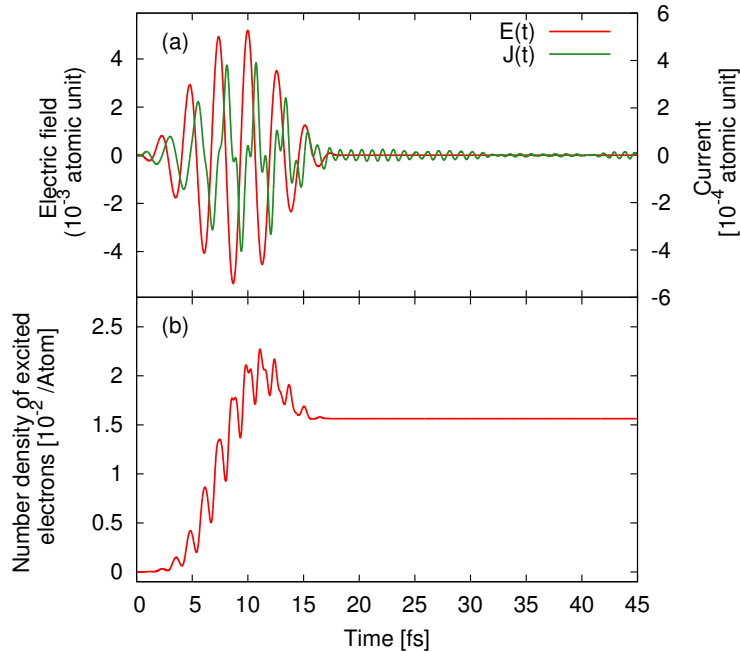


Figure 5.1: (a) The time profile of the electric field applied to crystalline silicon and the current induced by the field. The laser intensity corresponds to $I = 1.0 \times 10^{12}$ W/cm$^2$. (b) The number density of excited electrons per atom.

We next discuss the number density of excited electron-hole pairs after the laser pulse ends for different intensities. Figure 5.2 shows the result. As seen from the figure, the number of excited electrons increases with increasing the applied field intensity. At low intensity region, they scale with the square of the field intensity. This is because two photons are required for electrons to be excited across the direct band gap. In the figure, the horizontal line indicates the critical number density, the plasma frequency of this critical density coincides with the frequency of the incident laser pulse. At around the field intensity of $1.0 \times 10^{12}$ W/cm$^2$ corresponding to the critical number density, the number density of electron-hole pairs becomes larger than the intensity squared line. As will be seen later, the dielectric property of excited matter shows a large change from that in the ground state at field intensities around this value and above.
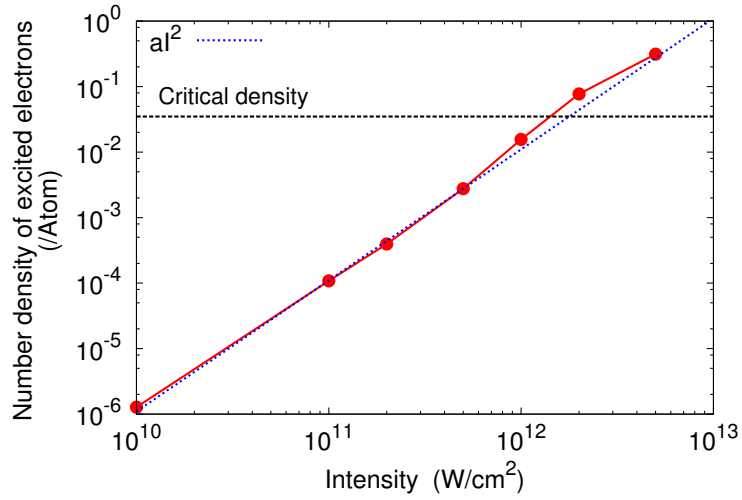


Figure 5.2: The number density of electron-hole pairs of the crystalline silicon in the final state following the pulsed excitation as a function of the maximum pump intensity determined as $I = cE_0^2/8\pi$. The critical density is indicated by the horizontal line. The squared intensity line normalized at $10^{10}$ W/cm$^2$ is also shown by blue-dotted line.

### 5.2.2  Dielectric function from numerical pump-probe experiments

To extract dielectric properties of excited matter, we compare two calculations, one solving the time-dependent Kohn-Sham equation of Eq. (2.47) with the vector potential containing pump and probe pulses and the other containing the pump pulse only. We denote the electric field of the pump pulse as $E_P(t)$ and that of the probe pulse as $E_p(t)$. We denote the current in the calculations containing the pump pulse only as $J_P(t)$ and that in the calculations containing both pump and probe pulses as $J_{Pp}(t)$. We define the current induced by the probe pulse as the difference,

$$J_p(t) = J_{Pp}(t) - J_P(t). \tag{5.2}$$

From the probe current $J_p(t)$, we may extract the electric conductivity $\sigma(\omega)$ and the dielectric function $\epsilon(\omega)$ of excited matter by the following equations:

$$\sigma(\omega) = \frac{\int dt J_p(t) e^{i\omega t}}{\int dt E_p(t) e^{i\omega t}}, \tag{5.3}$$

$$\epsilon(\omega) = 1 + \frac{4\pi i \sigma(\omega)}{\omega}, \tag{5.4}$$

We note that, in principle, the above-defined conductivity and dielectric function depend also on the time delay $\tau_{Pp}$ between the pump and probe pulses. We will later show that the dependence on delay-time is rather small, at least for the real part of the dielectric function.

In practice we employ the vector potential of the form of Eq. (5.1) as the pump pulse. As for the probe pulse, we use the same functional form as Eq. (5.1) delayed by an amount $\tau_{Pp}$ from the pump pulse,

$$A_p(t) = -c\frac{e_0}{\omega_p}\cos\left(\omega_p(t - \tau_{Pp})\right) \times \sin^2(\pi(t - \tau_{Pp})/\tau_L) \tag{5.5}$$

for $\tau_{Pp} < t < \tau_L + \tau_{Pp}$ and zero otherwise.

In Fig. 5.3, we show typical time profiles of the electric fields and the induced currents for a delay time of $\tau_{Pp} = 19$ fs. The pump pulse is the same as in Fig. 5.1, with a maximum intensity of $1.0 \times 10^{12}$ W/cm$^2$. The probe intensity is a factor of 100 smaller, which we deem to be sufficiently weak to extract the linear response. In the left panels of Fig. 5.3, we show electric fields of pump and probe pulses, $E_P(t) + E_p(t)$, in (a), pump pulse, $E_P(t)$, in (b), and probe pulse, $E_p(t)$, in (c), as functions of the time. The right panels show currents induced by the pump and probe pulses, $J_{Pp}(t)$, in (d), by the pump pulse only, $J_P(t)$, in (e), and the difference of the currents, $J_p(t)$ of Eq. (5.2), in (f).
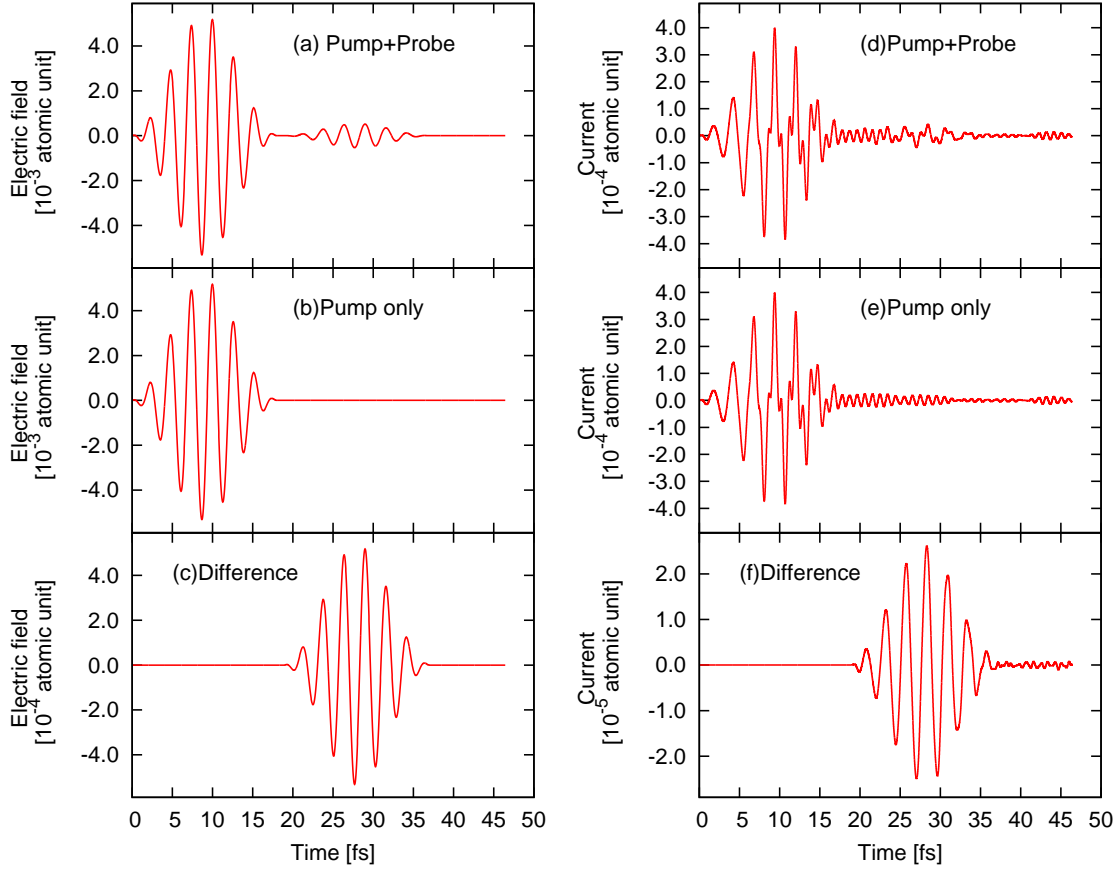
Figure 5.3: Left panels show the electric field of pump and probe pulses in (a), pump pulse in (b), and the probe pulse in (c). Right panels show the current induced by the pump plus probe pulse in (d), the current by the pump pulse only in (e), and the difference of the currents shown in (d) and (e) in (f).

The next step is to calculate the dielectric function from the probe current using Eqs. (5.3) and (5.4). The pump-probe calculation using the probe pulse of Eq. (5.5) and the probe current of Eq. (5.2) gives us dielectric properties around the average frequency $\hbar\omega_p$. To explore the dielectric properties for a wide frequency region, we repeat the pump-probe calculations for different frequencies of the probe pulses.

In Fig. 5.4, we show typical calculations using a number of probe pulses of differing frequencies. Panels (a) and (b) show the absolute values of the Fourier transforms of $E_p(t)$ and $J_p(t)$, respectively. Panels (c) and (d) show the real and imaginary parts of the dielectric function which is calculated using Eqs. (5.3) and (5.4). The curve is composed of a number of curves with different colors for each probe frequency. One can see that the overlap is very good for the different average probe frequencies, validating our method to extract the dielectric function.
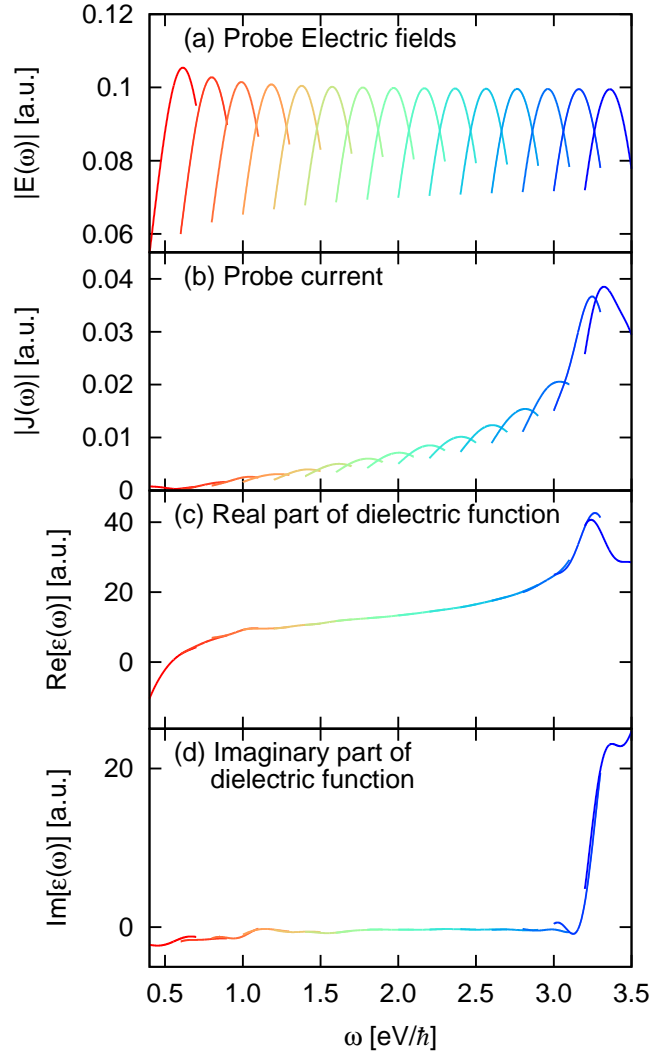
Figure 5.4: The top two panels show the Fourier transformations of the probe electric field $E_p(\omega)$ and the probe current $J_p(\omega)$. The bottom two panel shows the real and imaginary parts of the dielectric function extracted from $E_p(\omega)$ and $J_p(\omega)$ through Eqs. (5.3) and (5.4). The pump pulse has an intensity $I = 1.0 \times 10^{12}$ W/cm$^2$ and an average frequency $\omega_P = 1.55$ eV/$\hbar$. The polarization directions of the pump and probe pulses are taken to be parallel.

We have carried out the pump-probe simulations for several intensities of the pump pulse. The results for the dielectric functions are shown in Fig 5.5. The real and the imaginary parts are presented in panels (a) and (b), respectively.

The distinguishing feature in the response is the negative divergence at small frequencies seen in the real part. This arises from the quasiparticles in the excited system, as we will see more quantitatively later. The imaginary part of the response is not quite as simple to analyze. At the strongest case

of $I = 5.0 \times 10^{12}$ W/cm$^2$, the dielectric functions calculated using probe pulses of different central frequencies are not connected smoothly. This indicates the imaginary part of the dielectric function is not well defined under strong excitation.
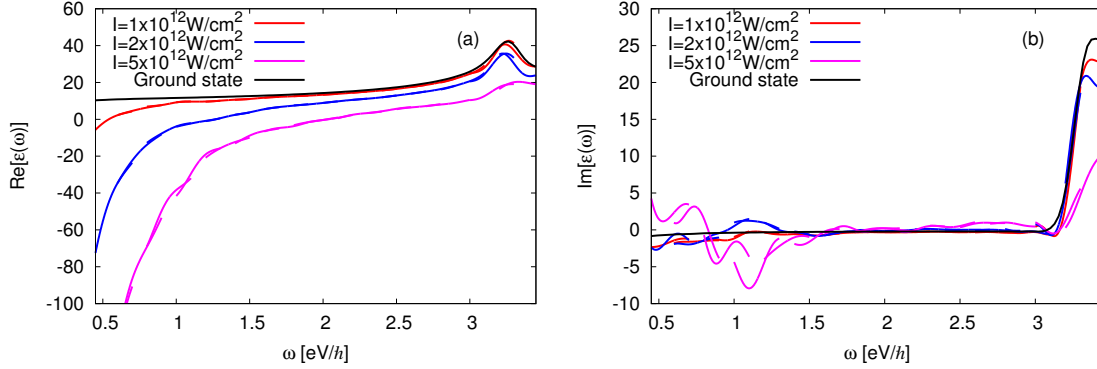


Figure 5.5: Real (a) and imaginary (b) parts of the dielectric functions of Si excited by field pulses of three intensities. The dielectric functions are deduced using pump-probe calculations. The polarization direction of the probe pulse is taken to be parallel to that of pump pulse. The dielectric function of silicon in the ground state is also shown.

An interesting feature of the TDDFT response is that the dielectric tensor is not isotropic in the excited crystal, even though the crystal symmetry is cubic. This may be seen in Fig. 5.6, comparing the dielectric functions for the probe polarization either parallel or perpendicular to the pump polarization.

The real part of the dielectric function shows the low-frequency plasmon response more strongly for the parallel component. One may notice that $\mathrm{Im}[\epsilon(\omega)]$ is negative at some frequencies when pump and probe pulses are parallel. This was also observed in Fig. 5.4(d). This might indicate a population inversion that could sustain a growth of intensity at those frequencies. However, one should carry the coupled calculation of the electron dynamics and the propagation of laser pulses in Sec. 2.3 to assert that the excited medium can amply the pulses.

We next ask how sensitive the extracted dielectric function is to the time delay of the probe pulse. Since there are no dissipative processes in the adiabatic TDDFT, the properties of the system should not change after some initial period when the phases of the excited orbitals become incoherent. Figure 5.7 shows how the extracted dielectric function depends on delay time for the case of strongest laser intensity shown in Fig. 5.5.

We have selected delay times over a range that corresponds to a full cycle of the pump pulse, since that frequency could be imprinted on the phases of the particle at later times. The range of the delay times is 19.00 fs, 19.67 fs, 20.33fs, and 21.67fs. The latter three delay times correspond to a quarter, a half, and one period of the pump pulse $2\pi/\omega_P$ added to the first time. One can see that the variation of the real part is rather small, considering that the dielectric function without laser distortion is in the range of 10-15. The imaginary part, however, shows different behavior. Although the average values over the frequency region are more or less similar, the frequency dependences show substantial variation. This fact indicates that the imaginary part of the dielectric function is not well defined after the irradiation of the strong pump pulse and is consistent with the observation in Fig. 5.5(b).

We found the same behavior for other cases of time delays as well. Namely, the real part is
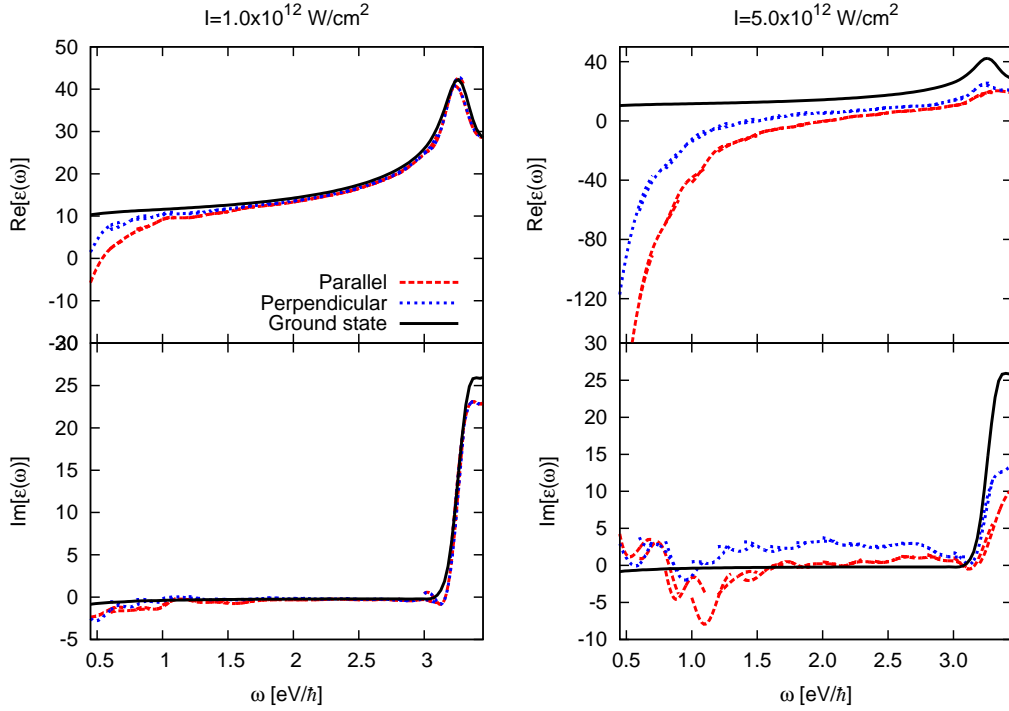
Figure 5.6: Comparison of dielectric functions of excited silicon probed with either parallel or perpendicular direction to the pump fields. Red dashed curves show results of parallel probe cases, blue dotted curves show results of perpendicular probe cases, and the black solid curves show dielectric function without the pump pulse.

mostly independent of delay, even extending the delay to very large times. The imaginary part is only qualitatively similar for different delay times for strong pump cases. In the sequel, we will analyze all the results using the dielectric function at $\tau_{Pp} = 19$ fs, and one should remember that the imaginary part is less well defined than the real part.

### 5.2.3 Comparison with free-carrier models

Dielectric properties of solids excited by intense and ultrashort laser pulses are often modeled employing a simplified dielectric function, adding a Drude-like component to the dielectric function in the ground state [135, 136]. In this subsection, we will examine how well the dielectric function of excited matter in the present calculation may be described by simplified dielectric models.

First we consider an embedded Drude model, the dielectric function given as a sum of the ground state response and the Drude response of free carriers

$$\epsilon_D(\omega) = \epsilon_0(\omega) - 4\pi \frac{e^2 n_{eh}}{m^* \omega(\omega + i/\tau)}. \tag{5.6}$$

Here $\epsilon_0(\omega)$ is the dielectric function in the ground state, $n_{eh}$ is the electron-hole density, $m^*$ is the reduced mass of electron-holes, and $\tau$ is the Drude damping time. For the dielectric function in the
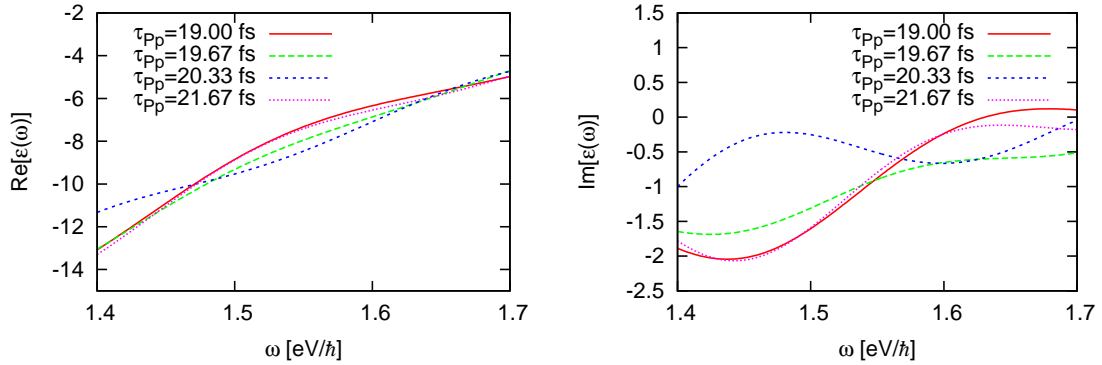
Figure 5.7: Extracted dielectric functions as a function of the delay time $\tau_{Pp}$. The pump pulse has an intensity $I = 5.0 \times 10^{12}$ W/cm$^2$ and an average frequency $\omega_P = 1.55$ eV/$\hbar$. The probe frequency is $\omega_p = 1.55$ eV/$\hbar$ and its delay times for the four graphed lines are $\tau_{Pp} = 19, 0, 19.67, 20.33$ and $21.67$ fs. The polarization directions of the pump and probe pulses are taken to be parallel.

ground state, $\epsilon_0(\omega)$, we will use the values obtained from the present calculation. The number density of electron-hole pairs, $n_{eh}$, is extracted from the calculation using Eq. (4.10). We treat $m^*$ and $\tau$ as parameters, fitting to the calculated $\epsilon(\omega)$.

Sokolowski-Tinten and von der Lind proposed a more sophisticated model for the dielectric function excited by strong laser fields [101], which we shall call the SL model. They consider three physical effects for the dielectric response of laser-excited semiconductor: (i) state and band filling, (ii) renormalization of the band structure, and (iii) the free-carrier response. The SL dielectric function is parameterized as

$$
\begin{aligned}
\epsilon_{SL}(\omega) &= 1 + [\epsilon_0(\omega + \Delta E_{gap}) - 1] \frac{n_0 - n_{eh}}{n_0} \\
&\quad - 4\pi \frac{e^2 n_{eh}}{m^* \omega(\omega + i/\tau)},
\end{aligned}
\tag{5.7}
$$

where $\Delta E_{gap}$ is the change of the band gap by the laser irradiation and $n_0$ is the density of electrons which contribute to the dielectric response. For $\Delta E_{gap}$, we use a change of single particle energies, $\epsilon_i^{t_f}$, of Eq. (4.9) at the time $t = t_f$ after the laser pulse ended. We treat the active number of valence electrons, $n_0$, as a fitting parameter.

We achieved the fits only to the real part of the dielectric function, which shows a smooth behavior as seen in Fig. 5.5. The imaginary part, which shows negative value for a certain frequencies cannot be described reasonably with the Drude model. Figure 5.8 shows the fits obtained in the embedded Drude model and the SL model for two intensities of the pump field. The polarization directions of the pump and probe pulses are taken to be parallel. The real part of the dielectric function is well fitted by both models. At higher intensity, both models describes well at lower frequencies, but the SL model fits better above the direct band gap.

In the fitting procedure, we found the effective mass is sensitive and can be determined without ambiguity. The effective mass for the pump pulse of $1.0 \times 10^{12}$ W/cm$^2$ is given by $m^* = 0.35$, while the effective mass for the pump pulse of $5.0 \times 10^{12}$ W/cm$^2$ is given by $m^* = 0.45$. The real part of the
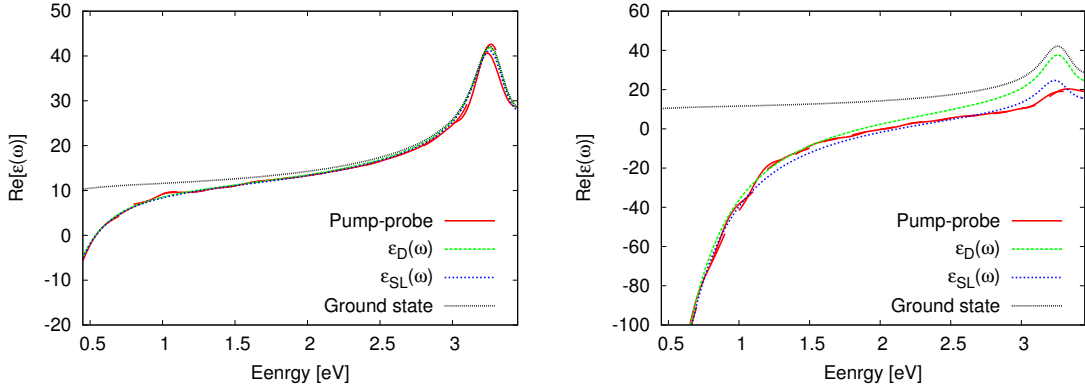
Figure 5.8: Dielectric function of silicon excited by two field pulses, $1.0 \times 10^{12} \mathrm{W/cm^2}$ (left panels) and $5.0 \times 10^{12} \mathrm{W/cm^2}$ (right panels), are fitted by the embedded Drude model and by the SL model. The polarization directions of the pump and probe pulse are taken to be parallel.

dielectric function is not sensitive to the collision time. In the fit, we use $\tau = 25$ fs, but other values give similar curve. We have also achieved fits to the case of the probe pulse polarization perpendicular to the pump one. The effective mass for the pump pulse of $1.0 \times 10^{12}$ W/cm$^2$ is given by $m^* = 0.70$, while the effective mass for the pump pulse of $5.0 \times 10^{12}$ W/cm$^2$ is given by $m^* = 0.85$. We thus find that the effective mass increases as the pump intensity increases. The effective mass is also larger for the cases of perpendicular polarizations of pump and probe pulses than for the parallel case.

The effective mass and its change with the pump intensity and polarization may be understood from the band structure. A weak pump pulse excites electrons at specific $k$-points by two-photon absorption, while a strong pump pulse excites electrons at various $k$-points by tunnel and multi-photon excitations. The effective mass of electrons depends very much on the their positions in the bands.

In the SL fitting, we use a change of energy gap, $\Delta E_g$, estimated from $\epsilon_i^{t_f}$. This is a small negative value, $\Delta E_g \simeq 0.01$ eV. The gap narrowing in highly excited matter has been an actively discussed issue both experimentally and theoretically. Much larger amount of decrease than the present analysis has been theoretically reported and attributed to a change of dielectric screening effects [138, 139]. This is an electron correlation effect which requires a treatment beyond the adiabatic TDDFT.

## 5.3 Electronic thermal-equilibrium phase

The numerical pump-probe experiments reported in Sec. 5.2 are applicable to the excited matter immediately after the pump irradiation, perhaps for a time period of a few tens of femtoseconds. In this section, we will investigate dielectric properties of thermally excited matter, which should be more appropriate at later times. We assume that the electronic states are described by a thermal ensemble, but the ions have not yet had time to respond.

### 5.3.1 Ground state

We model the electronic state of crystalline silicon after irradiation of a high-intensity laser pulse by static DFT for a thermal ensemble of electrons. Atomic positions are kept at their equilibrium positions in the ground state, assuming that electron thermalization time is so short that atomic motions may be ignored. The Kohn-Sham equation for orbitals is given by

$$\left\{ -\frac{\hbar^2}{2m_e}\nabla^2 + V_{ion} + \int d\boldsymbol{r}' \frac{e^2}{|\boldsymbol{r}-\boldsymbol{r}'|}\rho^T(\boldsymbol{r}') + \mu_{xc} \right\} \phi_i(\boldsymbol{r}) = \epsilon_i \phi_i(\boldsymbol{r}). \tag{5.8}$$

The electron density at temperature $T$, $\rho^T(\boldsymbol{r})$, is given by

$$\rho^T(\boldsymbol{r}) = \sum_i n_i^T |\phi_i(\boldsymbol{r})|^2, \tag{5.9}$$

where $n_i^T$ is the temperature-dependent occupation number of Fermi-Dirac distribution,

$$n_i^T = \frac{1}{1 + \mathrm{e}^{(\epsilon_i - \mu)/k_B T}}. \tag{5.10}$$

Here $\epsilon_i$ is the energy of electron orbitals, $\mu$ is the chemical potential, and $k_B T$ is the temperature in energy units. We note that all the quantities related to the orbitals, $\phi_i$, $\epsilon_i$, and $\mu$ depend on the temperature $T$ due to the self-consistency requirement.

For the present purpose, it is essential to use a functional which reproduces both indirect and direct band gaps. The reproduction of the indirect band gap is important to produce correct density of electron-hole pairs for a given electronic temperature. The reproduction of the direct band gap is important for reasonable descriptions of the optical properties. We choose the meta-GGA (generalized-gradient approximation) potential of Tran and Blaha [103] for the exchange-correlation potential, $\mu_{xc}$. The meta-GGA potential depends on the density $\rho^T(\boldsymbol{r})$, the gradient of the density $|\nabla\rho^T(\boldsymbol{r})|$, and the kinetic energy density $\tau^T(\boldsymbol{r}) = \sum_i n_i^T |\nabla\phi_i(\boldsymbol{r})|^2$. The Tran-Blaha meta-GGA potential is known to resolve to some extent the band gap problem inherent to the local density approximation.

Practical calculations are achieved as follows. We consider only valence electron orbitals treating electron-ion interaction by a norm-conserving pseudopotential [107, 108]. We use a three-dimensional grid representation to represent orbital wave functions. The cubic unit cell of a side length $a = 10.26$ a.u. containing eight silicon atoms is discretized into $20^3$ grid points. The $k$-space is also discretized into $32^3$ grid points.

Figure 5.9 shows number density of excited electrons as a function of electron temperature for crystalline silicon. Here, we define the number density of excited electrons $n_{e-h}$ by,

$$n_{e-h} = \frac{1}{\Omega}\sum_{i=cond.} n_i^T, \tag{5.11}$$

where the sum is carried out for conduction bands.

As seen from the figure, the number density of excited electrons monotonically increases as the electron temperature increases. At electron temperature of 1.0 eV, which corresponds to 11,600K, the number density of electron-hole pairs is 0.2 per atom, indicating excitations of 5 % of valence electrons. We note that electronic temperatures and number densities of excited electrons shown in Fig. 5.9 correspond to values of physical interests. It has been often argued that the critical electron density is related to the laser damage threshold. The critical electron density is so defined that the plasma frequency of excited carriers coincides with the laser frequency. For Si at $\lambda = 625$ nm, it is estimated to be $n_c = 8.7 \times 10^{21}$ cm$^{-3}$ [101]. We also note that several experiments have observed laser-excited solids where the number density of excited electrons exceeds $10^{22}$cm$^{-3}$ [101,140]. In theoretical ab-initio calculations, transition of laser-irradiated silicon into liquid phase has been discussed [141]. In the analysis, initial electronic temperature which is necessary for liquid transition is reported to be 25,000 K (2.15 eV). In [142], instabilities of phonon modes of silicon are reported following thermal electronic excitations at temperature 1.5 eV.

Figure 5.10 shows occupation distributions at various temperatures, as well as the density of states shown by black solid line. At temperatures around 1 eV, we find a substantial excitations of electrons from orbitals within 3 eV below the highest occupied orbital to orbitals within 5 eV above the lowest unoccupied orbitals. From the figure, we find that there is little change in the amount of band gap for wide temperatures. In literatures [139, 143], changes of band gap due to band gap renormalization effect [139] and to a decrease of electron-hole attraction [143] have been investigated. They are originated from screening effects by excited carriers. We consider that these correlation effects are not properly treated in our thermal TDDFT calculation with the meta-GGA potential.
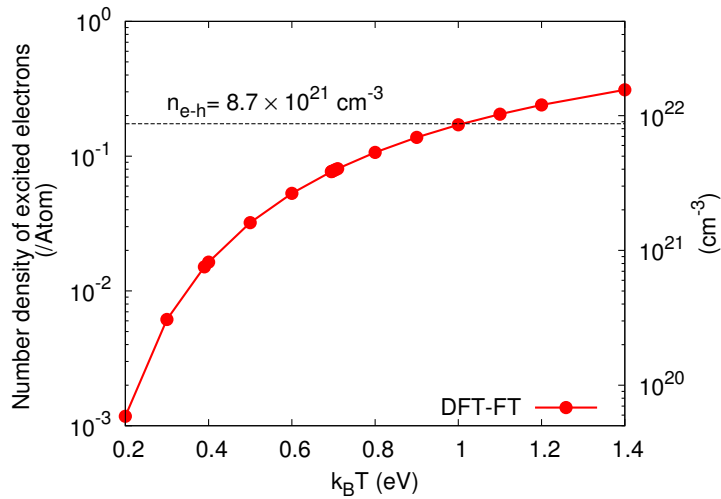


Figure 5.9: The number density of electron-hole pairs is shown as a function of electronic temperature in the thermal DFT calculation of crystalline silicon.
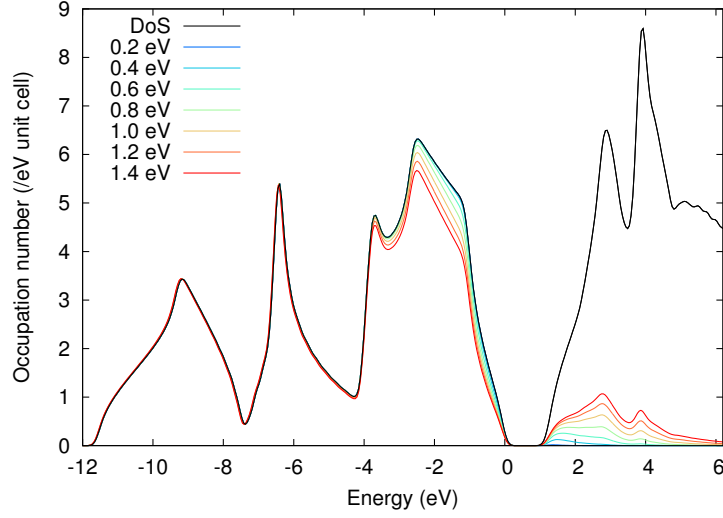
Figure 5.10: Occupation number distribution of silicon at various temperatures. The density of states is also shown by black-solid line.

### 5.3.2 Linear response

We calculate dielectric properties of the medium in the adiabatic TDDFT, using the same Tran-Blaha meta-GGA potential for the response calculation. Numerically, we solve the time-dependent Kohn-Sham equation (2.42) in real time to calculate the dielectric property. The density $\rho(\boldsymbol{r}, t)$ is constructed from time-dependent orbitals as $\rho(\boldsymbol{r}, t) = \sum_i n_i^T |\psi_i(\boldsymbol{r}, t)|^2$, using the occupation numbers in the ground states. To explore the dielectric property, we apply a distorting vector potential of step function in time [96, 100].

$$\boldsymbol{A}(t) = \boldsymbol{e}_\beta A_0 \theta(t), \tag{5.12}$$

where $\boldsymbol{e}_\beta$ is a unit vector in the $\beta$ direction. We calculate the current flowing within the unit cell from the solution by

$$\boldsymbol{J}(t) = -\frac{e}{\Omega} \sum_i n_i^T \int_\Omega d\boldsymbol{r} d\boldsymbol{r}' \psi_i^*(\boldsymbol{r}, t) \boldsymbol{v}(\boldsymbol{r}, \boldsymbol{r}') \psi_i(\boldsymbol{r}', t), \tag{5.13}$$

where $\Omega$ is a volume of the unit cell and the velocity operator $\boldsymbol{v}(\boldsymbol{r}, \boldsymbol{r}')$ is defined by

$$\boldsymbol{v}(\boldsymbol{r}, \boldsymbol{r}') = -\frac{i\hbar}{m_e} \boldsymbol{\nabla} \delta(\boldsymbol{r} - \boldsymbol{r}') + \frac{1}{i\hbar} \left[ \boldsymbol{r} V_{ps}^{NL}(\boldsymbol{r}, \boldsymbol{r}') - V_{ps}^{NL}(\boldsymbol{r}, \boldsymbol{r}') \boldsymbol{r}' \right], \tag{5.14}$$

where $V_{ps}^{NL}$ is the nonlocal part of the pseudopotential. The conductivity is calculated from the induced current by

$$\sigma_{\alpha\beta}(\omega) = -\frac{c}{A_0} \int_0^T dt e^{i\omega t} W(t/T) J_\alpha(t), \tag{5.15}$$

where $J_\alpha(t)$ is the $\alpha$ component of $\boldsymbol{J}(t)$, and $T$ is the duration of time evolution. We use the mask function $W(x)$ given by $W(x) = 1 - 3x^2 + 2x^3$ [125]. The dielectric function is obtained from the

conductivity by

$$\epsilon_{\alpha\beta}(\omega) = \delta_{\alpha\beta} + \frac{4\pi i \sigma_{\alpha\beta}(\omega)}{\omega}. \tag{5.16}$$

In silicon, only diagonal element appears in the thermal model, $\epsilon_{\alpha\beta}(\omega) = \delta_{\alpha\beta}\epsilon(\omega)$.

In time evolution calculations, we use the same grid points in the real space and the $k$-space as those in the static calculation. The time propagation is computed using a fourth-order Taylor expansion method [91], with a time step of $\Delta t = 0.04$ a.u. The total duration of the time evolution is $T = 1,280$ a.u. with the number of time steps $N_T = 32,000$.

In Fig. 5.11, we show dielectric functions of silicon at several electron temperatures. In the real part of the dielectric function, all responses at finite temperatures show a strong negative behavior at low frequencies. This Drude-like behavior comes from excited electron-hole pairs. The low energy component of the imaginary part shows absorptive contributions at low frequencies, increasing monotonically as the temperature increases. In the previous study in Sec. 5.2 employing the numerical pump-probe experiments which catch nonequilibrium distributions of electron-hole pairs, we have observed a similar behavior of Drude-like divergence in the real part. However, the absorptive contribution in the imaginary part was not observed.

A convenient way to exhibit the plasmon contribution to the response is to plot the imaginary part of the inverse dielectric function, $\text{Im}\epsilon^{-1}$. This is shown in Fig. 5.12 for several temperatures up to $k_B T = 1.4$ eV. At the lowest temperature, one sees a very sharp plasmon peak, located at an energy of $\sim 0.4$ eV. The plasmon excitation energy increases with temperature, due to the increased density of electron-hole pairs. We note that the width of the plasmon also increases with temperature, up to about $k_B T \approx 0.6$ eV. Beyond that, the width does not change very much, up to the maximum temperature considered.

We note that local field corrections are not important in the above results. Namely, results shown above hardly change if we fix the Kohn-Sham Hamiltonian in Eq. (2.47) to that in the thermal ground state.

### 5.3.3   Comparison with free-carrier models

The dielectric response of solids excited by intense and ultrashort laser pulses is often modeled by a simplified dielectric function, adding a Drude-like component to the dielectric function in the ground state [136, 137]. In this section, we will show that a model of this kind can reproduce quite well our calculated finite-temperature response.

We again consider the SL model, which is introduced in Sec. 5.2 and is described by Eq. (5.7). We fit the parameters of the model by by minimizing the mean square error as given by

$$I_{error} = \int_{\omega_i}^{\omega_f} d\omega \left| \epsilon_T^{-1}(\omega) - \epsilon_{SL}^{-1}(\omega) \right|^2, \tag{5.17}$$

where $\epsilon_T(\omega)$ is the dielectric function in the thermal model. We take the interval $\hbar\omega_i = 0.3$ eV and $\hbar\omega_f = 6.0$ eV. The quality of the fit is shown in Fig. 5.13 for temperatures of $k_B T = 1.4$ eV in the thermal model. The fit is very good except for the $\text{Im}\epsilon$ at the lowest frequencies. In particular, the plasmon peak in the inverse dielectric function is very well reproduced.

In Fig. 5.14, we show the fitted effective mass $m^*$ and the collision time $\tau$ as functions of the temperature in the thermal model. The top panel shows that the effective mass $m^*$ increases as the temperature increases. We have found a similar behavior in the numerical pump-probe experiments
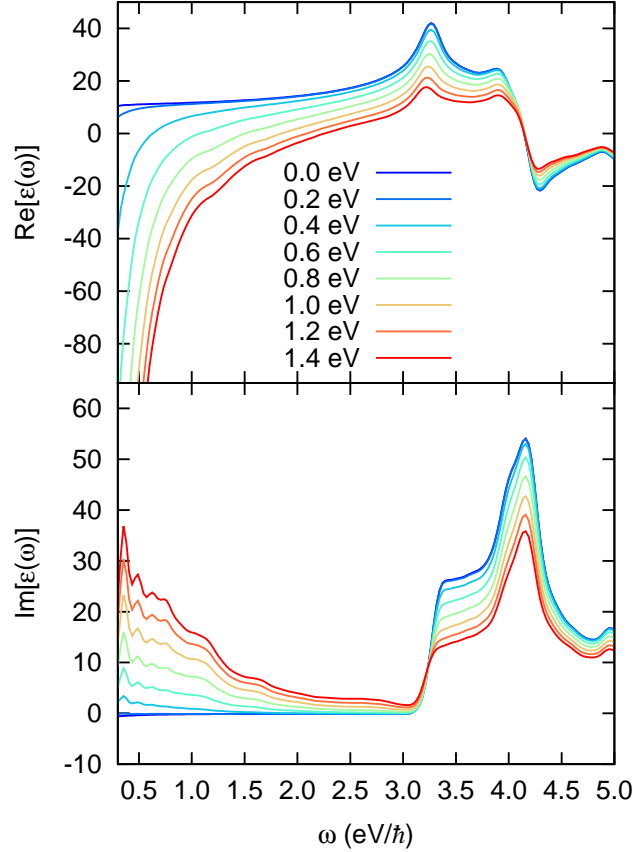
Figure 5.11: The dielectric function of silicon in the finite temperature model at several temperatures. Top panel shows the real part of the dielectric function, and the bottom panel shows the imaginary part.

in Sec. 5.2. The change of effective mass may be understood by the change of the distribution of the electron-hole pairs in $k$-space.

The bottom panel of Fig. 5.14 shows that the damping time $\tau$ becomes very small as the electron temperature increases. The value of $\tau$ monotonically decreases and reaches a value of 1.0 fs at $k_B T \approx$ 1.4 eV. At first sight this is puzzling, because there are no explicit collision effects in either the time-dependent Kohn-Sham equation or in the thermal model in the adiabatic meta-GGA which we adopted. Since we fix ion positions during time evolution calculations of orbitals, no electron-phonon interactions are taken into account. In spite of them, our plasmon peak has a large damping, corresponding to collision times as short as 1.0 fs in the thermal model. We consider that the damping arises from the elastic scattering of electrons from ionic core potentials. Since the electron-ion interactions constitute periodic potential for electrons, we may equivalently say that the damping is due to the interband transitions of excited carriers. We note that TDDFT treatment of linear response describes the dielectric function of metals fairly well, including the width of plasmon seen in the inverse dielectric
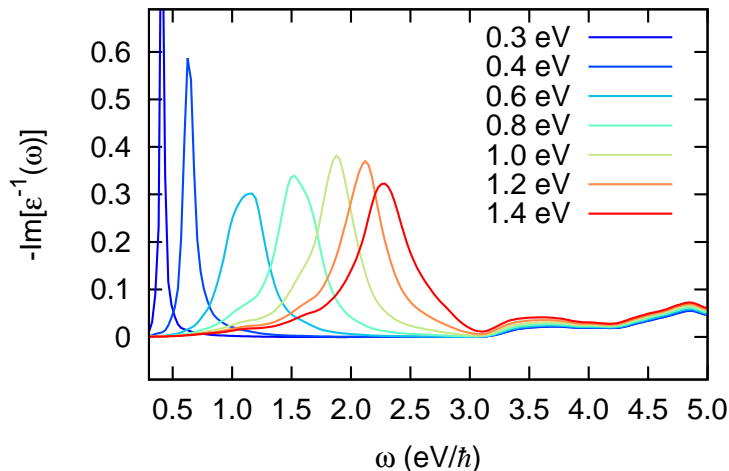
Figure 5.12: The imaginary part of the inverse dielectric function for various electronic temperatures.

function [96].

### 5.3.4 Comparison with numerical pump-probe experiments

In Sec. 5.2, we have carried out numerical pump-probe experiments to extract dielectric properties of laser-excited silicon immediately after irradiation by the laser pulse. This method catches fully the nonequilibrium nature of the excited electrons. The difference between the numerical pump-probe calculations and the present thermal model comes entirely from the different electron-hole distributions in the excited system to be probed. In this subsection, we compare their predicted dielectric functions.

To compare results of the thermal model with those of the numerical pump-probe experiments, we first need to assume a correspondence between the excited systems that we wish to compare. Since the plasmon characteristics are closely tied to the number of electron-hole pairs, we shall use that measure to make the comparison.

In Sec. 5.2, we solved the time-dependent Kohn-Sham equation with laser pulses of the frequency $\hbar\omega = 1.55$ eV and the duration of the pulse $\tau_L = 18$ fs, and calculated the number density of excited electrons induced by the laser pulses. We showed the number of excited electrons as a function of the laser intensity in Fig. 5.2. Combining Fig. 5.2 and Fig. 5.9, we can relate the laser intensity $I$ and the electronic temperature $k_B T$ through the number density of electron-hole pairs $n_{eh}$. For example, in the TDKS calculation using the laser pulse of $I = 1.0 \times 10^{12} \text{W/cm}^2$ excites electron hole pairs of $n_{eh} = 0.016$/Atom. From Fig. 5.9, the corresponding temperature is given by $k_B T = 0.4$ eV. For the laser pulse of $I = 5.0 \times 10^{12} \text{W/cm}^2$, the density of electron-hole pair is $n_{eh} = 0.31$/Atom. Corresponding temperature is $k_B T = 1.4$ eV. In the following, we use $n_{eh}$ to specify calculations of the finite temperature model and the numerical pump-probe experiments.

We show a comparison of dielectric function by two methods for two cases, $n_{eh} = 0.016$ /Atom and $n_{eh} = 0.31$ /Atom, in Fig. 5.15. The black lines show dielectric function of thermal model. The red-dashed line and the blue-dotted line show the results of the numerical pump-probe calculations for probe polarization parallel and perpendicular to the pump, respectively.
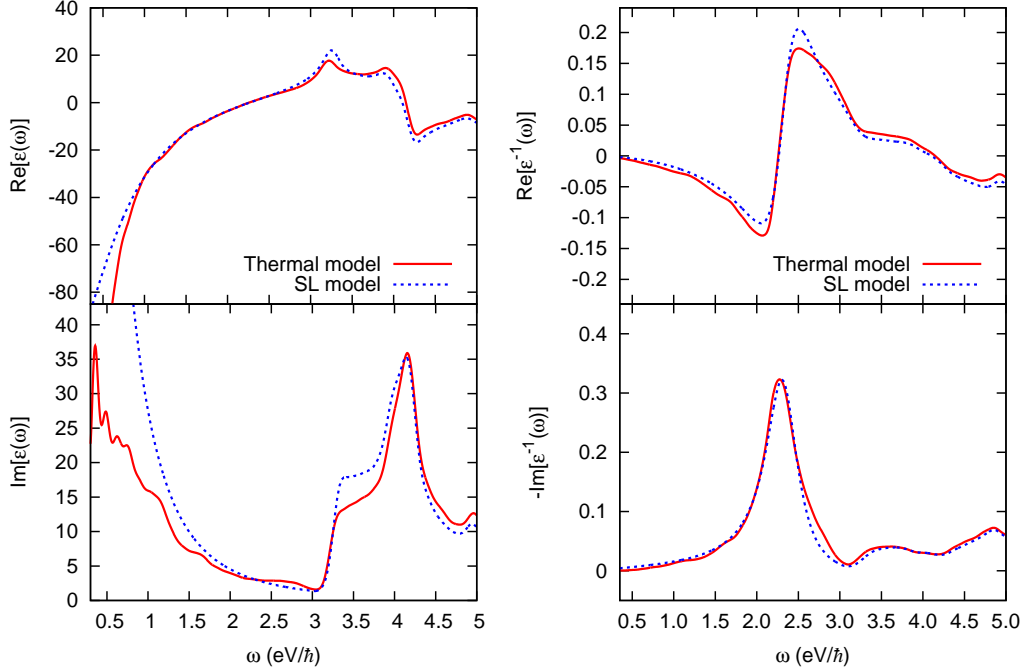
Figure 5.13: Comparison of the thermal model and a fit with the SL model. The electronic temperature in the thermal model is $k_B T = 1.4$ eV.

As seen from the figure, the real part of the dielectric function of silicon excited by the pump pulse is close to the thermal model for two cases. At lower excitation of $n_{eh} = 0.016$ /Atom, the thermal model is close to the pulsed excitation in the parallel probing. At higher excitation of $n_{eh} = 0.31$ /Atom, the thermal model is again close to the pulsed excitation in the parallel probing at higher frequencies ($\hbar\omega > 1$ eV) and is between the parallel and perpendicular probings at low frequencies ($\hbar\omega < 1$ eV). The imaginary part of the dielectric function looks rather different. While the thermal model predicts positive imaginary part below the band gap, the pulse-excited silicon shows much smaller value, even negative in certain frequencies.

The difference between two calculations comes entirely from different distributions of electron-hole pairs: thermal equilibrium distributions in the thermal model and nonequilibrium distributions in the numerical pump-probe simulation. To clarify the difference, we investigate population distributions in energy and momentum space.

We first denote the orbital index $\{i\}$ in terms of $\{b, \boldsymbol{k}\}$, where $b$ indicates bands and $\boldsymbol{k}$ indicates the Bloch momentum. Occupation numbers are expressed as $n_{b\boldsymbol{k}}^X$, where $X = T$ for thermal model and $X = NPP$ for numerical pump-probe simulation. We define the occupation distribution function by

$$f^X(\boldsymbol{k}, \epsilon) = \sum_b n_{b\boldsymbol{k}}^X \delta(\epsilon - \epsilon_{b\boldsymbol{k}}^X). \tag{5.18}$$

For numerical pump-probe simulation, we define the energy eigenvalue $\epsilon_{b\boldsymbol{k}}^{NPP}$ by solving the following
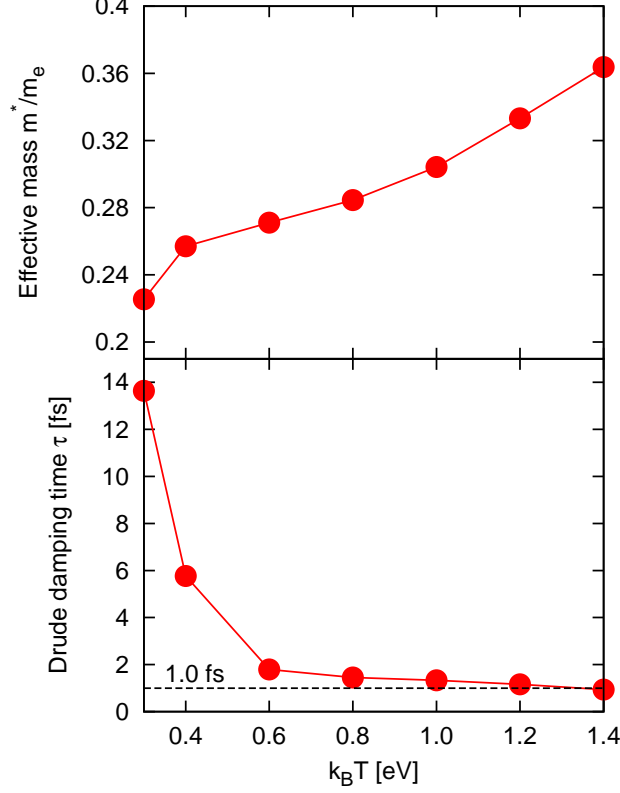
Figure 5.14: Parameters of the SL model determined by the fitting procedure to the thermal model. Top panel shows the effective mass $m^*$ and the bottom panel shows the Drude damping time $\tau$.

Kohn-Sham equation,

$$\hat{h}_{KS}^{NPP}(t_f)\phi_{b\boldsymbol{k}}^{NPP} = \epsilon_{b\boldsymbol{k}}^{NPP}\phi_{b\boldsymbol{k}}^{NPP}, \tag{5.19}$$

where $h_{KS}^{NPP}(t_f)$ is the time-dependent Kohn-Sham Hamiltonian at time $t_f$ when the laser pulse ended. The occupation number in the numerical pump-probe simulation is defined by

$$n_{b\boldsymbol{k}}^{NPP} = \sum_{b'\boldsymbol{k}'} |\langle \phi_{b\boldsymbol{k}}^{NPP} | \psi_{b'\boldsymbol{k}'}^{NPP}(t_f) \rangle|^2, \tag{5.20}$$

where $\psi_{b\boldsymbol{k}}^{NPP}$ is the solution of the time-dependent Kohn-Sham equation at time $t_f$.

Using the occupation distribution function, we first calculate the occupation distribution as a function of energy,

$$D^X(\epsilon) = \sum_{\boldsymbol{k}} \left\{ f^X(\boldsymbol{k},\epsilon) - f^0(\boldsymbol{k},\epsilon) \right\}, \tag{5.21}$$

where $f^0(\boldsymbol{k},\epsilon)$ is the occupation distribution function in the ground state at zero temperature. The calculated results are shown in Fig. 5.16 for cases when $n_{e-h} = 0.31$ /Atom. Red-solid line shows the
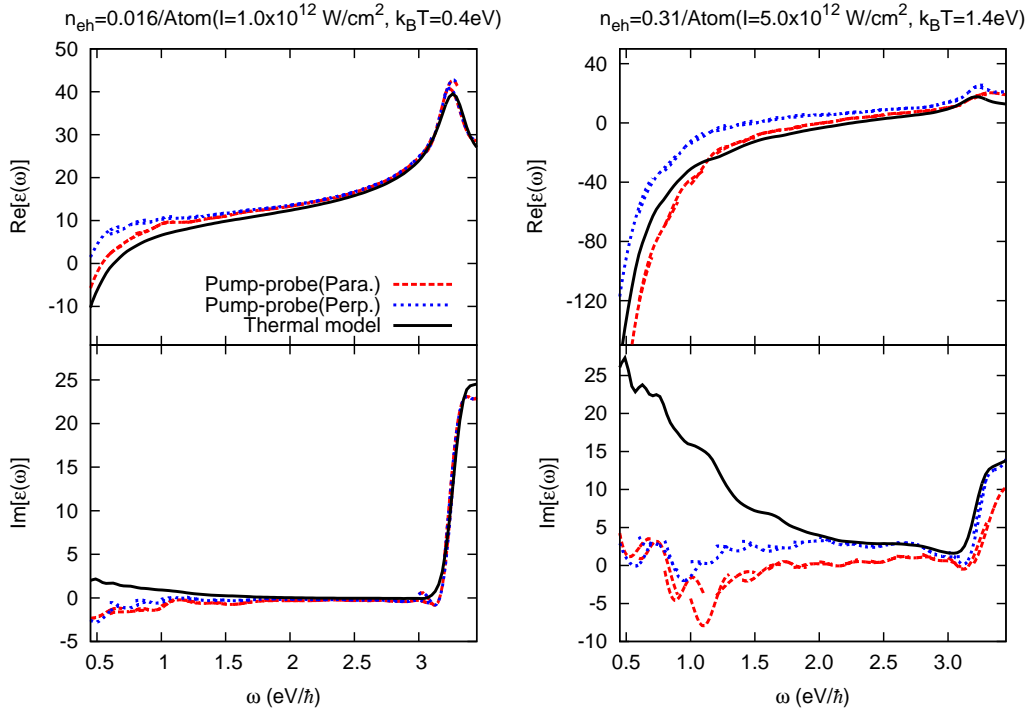
Figure 5.15: Comparisons of the dielectric function of the numerical pump-probe calculation and the thermal model. Left-hand panels: $n_{eh} = 0.016$ /Atom; right-hand panels: $n_{eh} = 0.31$ /Atom.

distribution of the numerical pump-probe simulation, and green-dotted line shows that of the thermal model. We set the highest energy of the valence band to zero. Positive values at positive energy region show distribution of electrons in conduction band, while negative values at negative energy region show the hole distribution in the valence band.

From the figure, we observe that electrons and holes distribute in wider energy region in the numerical pump-probe simulation than those in the electron thermal model. The decrease of the lower energy electron-hole and the increase of higher energy electron-hole in the numerical pump-probe simulation may cause optical emissions which negatively contribute to the imaginary part of the dielectric function. This explains small or even negative values of the imaginary part of the dielectric function in the numerical pump-probe simulation.

To further clarify the difference in electron-hole distributions, we calculate the distribution in the Bloch momentum space. We note that the Bloch momentum does not correspond to that in the primitive cell since we employ the cubic unit cell containing eight silicon atoms in our calculation. We define the distribution of electrons in the following way:

$$D_e^X(\boldsymbol{k}) = \int_0^\infty d\epsilon \left\{ f^X(\boldsymbol{k}, \epsilon) - f^0(\boldsymbol{k}, \epsilon) \right\}. \tag{5.22}$$

For the distribution of holes, integration is achieved for $\epsilon < 0$. We note that there holds $D_e^{NPP}(\boldsymbol{k}) = -D_h^{NPP}(\boldsymbol{k})$.

Figure 5.17 (a) shows the distributions of electrons and holes in the thermal model at electron

temperature $T = 1.4$eV, while Figure 5.17 (b) shows the distribution of electrons in the numerical pump-probe simulation at the pump intensity $I = 5.0 \times 10^{12}$W/cm$^2$. The polarization direction of the pump pulse is set parallel to $z$-direction. In both panels, distributions integrated over $k_y$ are shown in $k_x$-$k_z$ plane. As is evident from panels (a) and (b), there is a large difference in the distribution in momentum space between the thermal model and the numerical pump-probe simulation. In the thermal model, distributions of electrons and holes are different, reflecting the indirect band gap structure. The distribution in the numerical pump-probe simulation shows much more complex, structured, and nonuniform behavior than that in the thermal model, since electrons and holes are in nonequilibrium phase immediately after the laser irradiation. We note that the real parts of the dielectric functions do not show large differences between two calculations (See Fig. 5.15). This indicates that the real part of dielectric function is sensitive to the number density of excited electrons, not to the detailed distribution of electrons and holes.

We thus conclude that the thermal model describes the real part of the dielectric function quite well, provided the number density of electron-hole pairs is the same. The difference between two calculations comes from the nonthermal distribution of electron-hole pairs in numerical pump-probe simulation. It seems that the difference is more evident for the imaginary part. A nonequilibrium phase of electronic excitations manifests more sensitively in the imaginary part of the dielectric function.
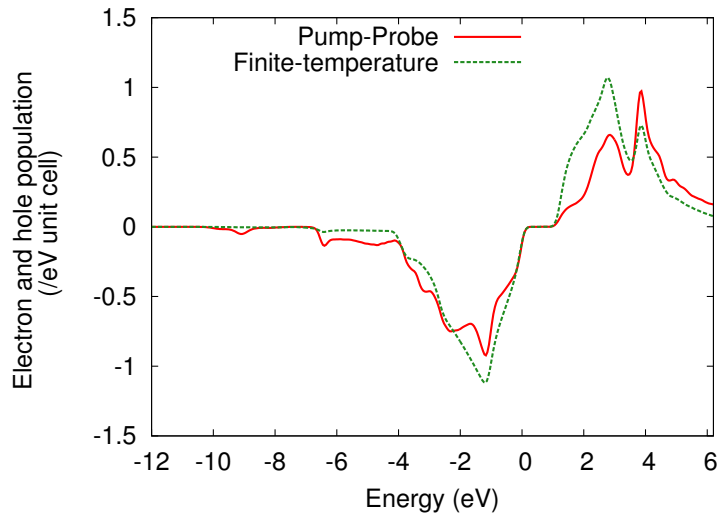


Figure 5.16: Population distribution of electrons and holes in laser-excited silicon.

## 5.4 Summary of optical properties of highly laser-excited solids

We have investigated the optical properties of highly laser-excited dielectrics based on the time-dependent density functional theory (TDDFT). In order to investigate the optical properties in the electronic nonequilibrium phase immediately after laser irradiation, we have developed the numerical pump-probe experiments in which two kinds of laser pulses are employed. One is the pump pulse which excites the system, and the other is the probe pulse by which the optical properties of the laser-excited system are extracted. The simulation makes it possible to investigate the optical properties of
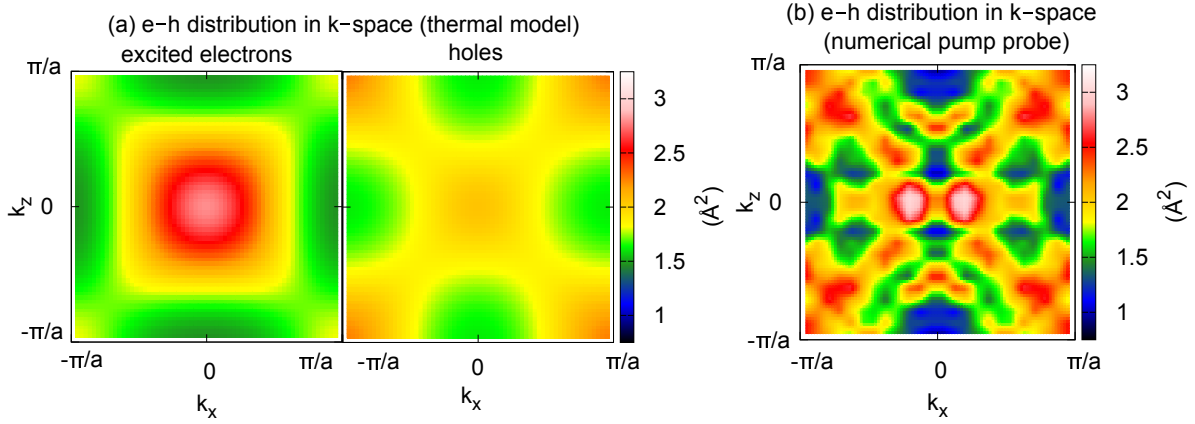
Figure 5.17: Population distributions of excited electrons and holes in the Bloch momentum space. The panel (a) shows the excited electron (left hand side) and hole (right hand side) distributions in the thermal model at electron temperature $k_B T = 1.4$eV, while the panel (b) shows the excited electron distribution in the numerical pump-probe method at the pump intensity $I = 5.0 \times 10^{12}$W/cm$^2$. The population distributions are shown in the $k_x$-$k_z$ plane integrating over $k_y$.

excited matter before any dissipation or dephasing effects start to become significant. Furthermore, we developed a linear response calculation for the finite electron-temperature systems to investigate the optical properties in the electronic thermal-equilibrium phase. In the method, the electronic systems are described with the Fermi-Dirac function for electronic occupation factors, while the lattice are fixed at their positions in the zero-temperature ground-state.

In the electronic nonequilibrium phase, we have found that the real part of the dielectric function can be reliably extracted in the numerical pump-probe experiments. It shows a metallic response reflecting dense electron-hole pair excitations. The imaginary part of the dielectric function is less well defined, especially at strong excitations. It has a negative value at certain frequencies, indicating a possible amplification of the laser pulse. The extracted dielectric function also shows anisotropy in the direction relative to the pump polarization direction. The difference comes from the nonequilibrium distributions of electrons and holes in $k$-space.

A simple model can be constructed using ingredients of the Drude model of free-electron dynamics. The real part of the dielectric function in the electronic nonequilibrium phase was found to be well described by a Drude-like contribution of the excited quasiparticles embedded in the dielectric medium corresponding to the ground state. In the embedded Drude model, there are three parameters determining the quasiparticle plasmon contribution, namely, the density of quasiparticles, their effective mass $m^*$, and the damping time $\tau$. The density of quasiparticles is known from the numerical simulation, but the other quantities are fit. From the real part of the dielectric function, we find that the effective mass increases with increasing pump field intensity, as expected from the band structure. We also find the effective mass depends on the relative direction between the pump and probe pulses, with a larger value in the perpendicular case than in the parallel case. The collision time cannot be determined reliably from the present numerical pump-probe experiments.

In the electronic thermal-equilibrium phase, we have found that the dielectric function shows the metallic response as in the nonequilibrium phase, reflecting the free-carrier response of excited

electrons. The imaginary part of the dielectric function in the thermal-equilibrium phase shows the absorptive contributions at low frequencies, while that in the nonequilibrium phase does not. This discrepancy originates from the difference between the thermal and nonequilibrium distribution of excited electrons. We have found that the dielectric function in the electronic thermal-equilibrium phase can be well described by the Drude-like model not only for the real part but also for the imaginary part. We have extracted the effective mass $m^*$ and the damping time $\tau$ from the dielectric function in the thermal-equilibrium phase by fitting with the Drude-like model. The effective mass increases as the temperature increases. This behavior is similar to the behavior of the effective mass in the nonequilibrium phase: the mass increases as the pump intensity increases. We have also found that the damping time monotonically decreases as the temperature increases and can be shot (about 1 fs). This short time value for the collision time is unexpected, since there are no explicit collision term in the time-dependent Kohn-Sham equation that we solve. We believe the short damping time comes from the elastic scattering of electrons from atom rather than from electron-electron or electron-phonon interactions, but we lack a simple model to exhibit this aspects of the response.

# Chapter 6

# Nonlinear polarization in time domain

## 6.1 Introduction

Nonlinear interactions of light with medium have been extensively studied for a long period [10,11,144, 145]. For relatively weaker intensities, low order nonlinear phenomena such as the second-harmonic generation (SHG) and the optical Kerr effect have been intensively studied and have already been applied in optical devices. Thanks to the recent development of laser technologies, high-intensity ultra-short laser pulses whose intensity is around $10^{13} - 10^{15}$ W/cm$^2$ and whose pulse width is less than 10 fs have become available. The field strength of these laser pulses is close to the strength of the force acting on electrons in medium, and the pulse length is comparable to the time scale of the electron dynamics. Thus, the high-intensity ultra-short laser pulses are suitable to control the motion of electrons in medium and to be employed to induce highly-nonlinear ultrafast phenomena. Recently, employing the high-intensity ultra-short laser pulses, several strongly-nonlinear phenomena in a femtosecond time-scale have been observed such as ultrafast charge transfer [56], modification of optical properties [53], and band-gap dynamics [57]. These phenomena would be useful for future applications to optoelectronic devices. Furthermore, once intensity of the laser pulses exceeds a critical threshold of materials, a permanent structural modification can be induced through a nonequilibrium phase induced by the nonlinear ultra-fast energy transfer from the laser to electrons in the medium. This kind of permanent structural modification has been applied to *non-thermal laser-processing* [36, 41].

One of the most fundamental physical quantities that describes interactions of light with matter is polarization $P$, which is spatially-averaged microscopic charge-separation such as induced-dipole of atoms in medium. The polarization represents responses of medium to applied electric fields $E$ and also produces additional electromagnetic fields. In conventional nonlinear optics, the polarization is treated by a perturbative expansion as follows,

$$P = \chi^{(1)}E + \chi^{(2)}E^2 + \chi^{(3)}E^3 + \cdots, \tag{6.1}$$

where $\chi^{(1)}$ is the linear susceptibility [1], and the quantities $\chi^{(2)}, \chi^{(3)}, \cdots$, are the nonlinear susceptibilities. For the linear and the low order nonlinear responses, the linear and the corresponding nonlinear susceptibilities give the complete description of the light-matter interactions. For example, reflectivity for weak light is described by $\chi^{(1)}$, the SHG is described by $\chi^{(2)}$, and the optical Kerr effect is described

---

[1]The linear susceptibility is related to the dielectric function as $\epsilon = 1 + 4\pi\chi^{(1)}$

by $\chi^{(3)}$. The linear and the low order nonlinear susceptibilities have been extensively studied from both theories [?] and experiments [?]. However, the perturbative expansion in Eq. (6.1) is no more useful for the strongly-nonlinear phenomena induced by the high-intensity ultra-short laser pulses, and sometimes is not even applicable. Therefore, direct investigations of the nonlinear polarization $P_{NL}$, which is the deviation from the linear response $P_{NL} = P - P_L = P - \chi^{(1)}E$, without any perturbative decompositions would be significant to understand the light-matter interactions in highly-nonlinear conditions.

Spatial and time scales of nonlinear polarizations are comparable to those of electromagnetic fields that induce the nonlinear polarizations. For infra-red laser pulses, the spatial scale of the nonlinear polarizations is sub-micrometer and the time scale is about femtoseconds. The microscopic origin of the linear and the nonlinear polarizations is the microscopic charge separation in the atomic scale. Experimental observation of such microscopic ultrafast phenomena is quite difficult and challenging. Thus, theoretical investigation of the strongly-nonlinear polarization based on the quantum electron dynamics in medium is significant.

In this chapter, we theoretically investigate the nonlinear polarizations induced by high-intensity ultra-short laser pulses in medium based on a coupled theoretical framework [100] of the time-dependent density functional theory [76] and Maxwell's equation. We simulate irradiation of intense femtosecond laser pulses on a SiO$_2$ ($\alpha$-quartz) thinfilm ($10\mu$m thickness) and calculate the nonlinear polarizations in the medium in the time domain. We analyze the calculated nonlinear polarization and find the time delay between the nonlinear polarization and the applied electric field, indicating the energy transfer from the light to the medium through the nonlinear light-matter interactions. We further investigate the microscopic origin of the nonlinear polarization based on the microscopic electron density dynamics in the subnanometer scale. In recent experiments, employing the *attosecond streaking* technique, it is possible to observe transmitted laser pulses in a attosecond time-resolution. We also compare the simulated transmitted laser pulses with recent experimental data.

## 6.2   Method

We employ the coupled theory of the TDDFT and Maxwell's equation, which is introduced in Sec. 2.3, in order to describe the interactions of high-intensity ultra-short laser pulses with the medium in the strongly nonlinear conditions. The numerical implementation of the method is introduced in Sec. 3.5. In the method, we simultaneously solve the time-dependent Kohn-Sham equation (2.56) for electron dynamics and the Maxwell equation (2.55) for electromagnetic fields. In this study, we simulate laser irradiation at normal incidence into the $\alpha$-quartz thinfilm (10 $\mu$m thickness). We take the propagation direction as $x$-axis and set $x = 0$ at the front surface of the thinfilm. We take the polarization direction of the incident electric field as $z$-axis.

We employ a meta generalized gradient approximation (meta-GGA) potential proposed by Tran and Blaha [103], which is introduced in Sec. 2.4 as Eq. (2.69). We set the $c_m$ parameter to 1.20 in order to reproduce the band gap of $\alpha$-quartz. We solve the Maxwell's equation (2.55) by using one-dimensional grid with spacing 10 nm for propagation of laser electromagnetic fields. Thus, we have 1000 macroscopic grid points to describe the 10 $\mu$m thinfilm. At each macroscopic grid point, we solve the time-dependent Kohn-Sham equation (2.56) employing a rectangular unit cell containing 6 Silicon atoms and 12 Oxygen atoms which are discretized into Cartesian grids of $20 \times 36 \times 50$. We set $c$-axis of $\alpha$-quartz parallel to the $z$-axis, which is the direction of the polarization of the incident electric field.

The laser pulse in the vacuum is described by the vector potential $\boldsymbol{A}(x,t)$ of the form

$$\boldsymbol{A}(x,t) = \hat{z}A_0 \sin^2(\pi t_x/T_p)\cos(\omega t_x), \tag{6.2}$$

in the domain $0 < t_x < T_p$ and zero outside. Here $\omega$ is the mean frequency, $t_x = t - x/c$ describes the space-time dependence of the field, and $T_p$ controls the pulse length. We set the mean frequency $\omega$ to 1.55 eV/$\hbar$, and set the full duration of the pulse length $T_p$ to 10.672 fs, which corresponds to the time of four optical-cycles; $T_p = 4 \times \frac{2\pi}{\omega}$. The full width at half-maximum (FWHM) intensity $\tau_p$ of the pulses is related to the full duration $T_p$ by $\tau_p = 0.364T_p$, which is about 4 fs.

## 6.3 Results

### 6.3.1 Modulation of transmitted laser pulses

We first illustrate the simulation of the laser irradiation into the $\alpha$-quartz thinfilm. Here, we employ the laser pulse with the peak intensity of $1.0 \times 10^{11}$ W/cm$^2$. Figure 6.1 shows snapshots of the laser propagation. The incident laser pulse in vacuum is irradiated on the $\alpha$-quartz surface and splits into two pulses. One is reflected at the surface and the other penetrates into the medium. Then the penetrating pulse further propagates in the medium. Finally, the pulse reaches at the rear surface and splits again into the reflected and transmitted pulses. We repeat this kind of simulations by changing intensities of the laser pulses and analyze the transmitted laser pulses and the induced polarizations in the medium.
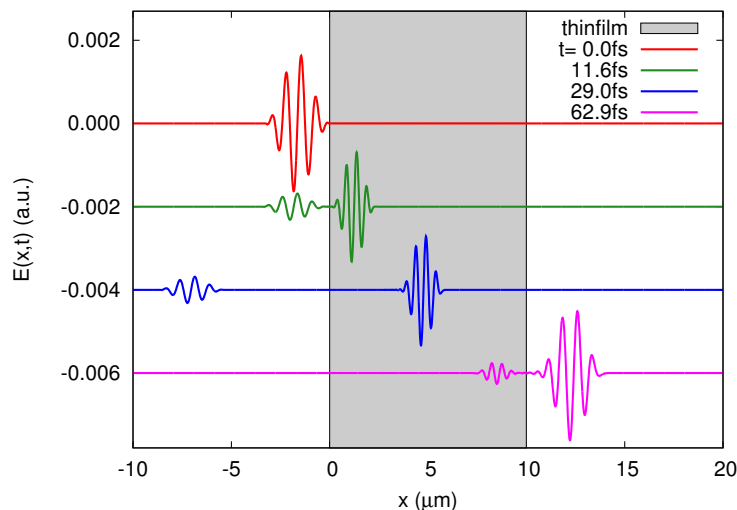


Figure 6.1: Snapshots of propagation of a laser pulse into the SiO$_2$ thinfilm.

Figure 6.2 shows the transmitted laser pulses as functions of time. Red-solid line shows the result for the incident peak intensity of $5 \times 10^{13}$ W/cm$^2$, and green-dashed line shows the result for $1 \times 10^{11}$ W/cm$^2$. The discrepancy of them completely originates from the nonlinear responses of the medium to the intense fields. One may see that the earlier part of the intense pulse is suppressed and the later part is enhanced, compared with the weak pulse. Moreover, a phase shift can be observed between

them around the strong intensity region (6-9 fs) in Fig. 6.2. Experimentally-observed transmitted-laser-pulses have also shown these features [146, 147]. These features are explained by change of the refractive index due to the intense fields: the head-suppression and tail-enhancement features are explained by the group velocity modification, so-called self-steepening [148], and the phase shift is explained by the phase velocity modification.

In Fig. 6.2, while the weak laser pulse does not show any fields at around 15 fs, the intense laser pulse has some high frequency components. By performing Fourier transformation, we have confirmed that this higher frequency component is the third-order harmonic of the incident laser pulse.
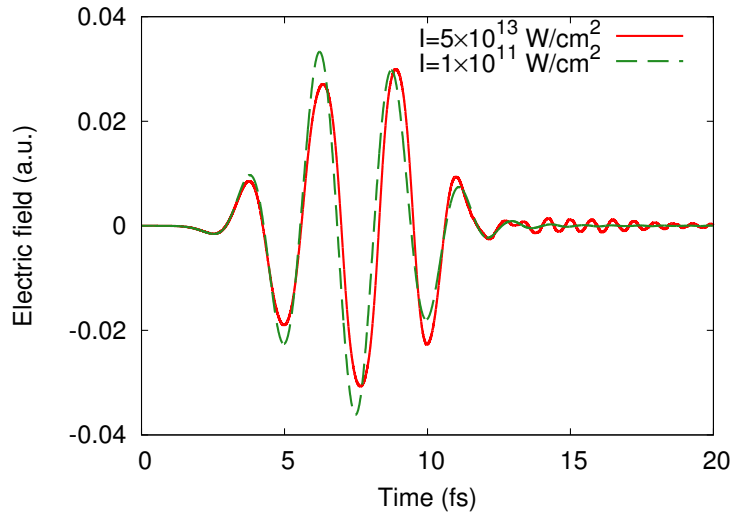


Figure 6.2: Transmitted laser pulses through a thin $SiO_2$ film as functions of time. Red-solid line shows the result for the incident peak intensity of $5 \times 10^{13}$ W/cm$^2$, and green-dashed line shows the result for $1 \times 10^{11}$ W/cm$^2$. The green-dashed line is scaled by multiplying $\sqrt{500}$ so as to coincide with red-solid line. We note that the pulse head comes earlier in time, and the pulse tail comes later.

To quantitatively investigate the transmitted pulses, we perform the Hilbert transformation (see Appendix A). The Hilbert transformation is one of the methods of signal analysis and provides information on amplitude and phase of pulsed waves. Figure 6.3 shows the result of the Hilbert transformation of the transmitted laser pulse with the incident peak intensity of $5 \times 10^{13}$ W/cm$^2$. Red-solid line shows the field amplitude as a function of time, and green-solid line shows the relative phase shift from the result of the weak laser pulse with the incident intensity of $1 \times 10^{11}$ W/cm$^2$. One sees that the positive phase shift appears at around $t = 6$ fs, when the amplitude achieves the maximum. Since positive phase shifts in time corresponds to the time delay, the phase velocity of the intense laser pulse at around the pulse peak is slower than that of the weak intensity laser pulse. As mentioned above, this velocity modification corresponds to the modification of refractive index originating from the nonlinear laser-solid interactions such as the optical Kerr effect and higher nonlinear effects.

We performed the Hilbert transformation for transmitted laser pulses of several intensities and extracted their phase shifts at the peak of the amplitude. Figure 6.4 shows the phase shift as a function of the incident laser intensity. Red-circle shows the theoretical results, and blue-square shows the experimental results [146,147]. The theoretical results show good agreement with the experimental results. This indicates that the present real-time TDDFT simulation succeeds to capture the nonlinear
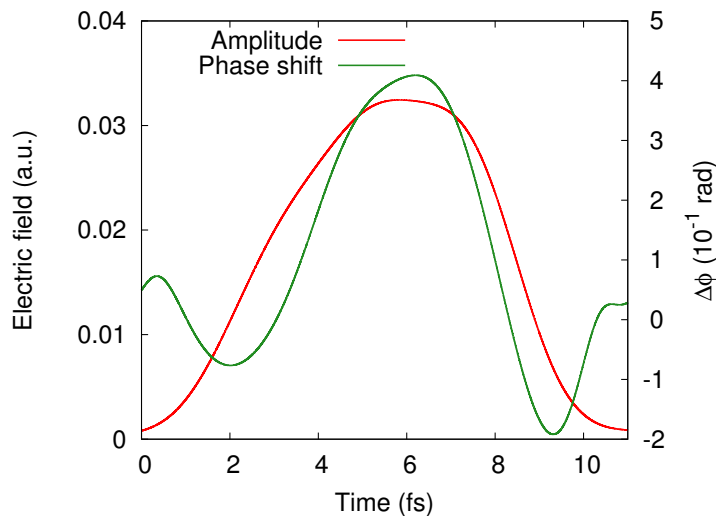
Figure 6.3: Hilbert transformation of the transmitted laser pulse whose incident intensity is $5 \times 10^{13}$ W/cm$^2$ through a thin SiO$_2$ film. Red-solid line shows the field amplitude of the laser pulse, and green-solid line shows the phase shift from the result of the weak intensity laser. We note that high frequency components ($\omega > 3.7$ eV/$\hbar$) such as optical harmonics are removed from the transmitted pulse before the Hilbert transformation in order to concentrate the fundamental frequency component.

nature of the light-medium interaction. As seen from the figure, the phase shift monotonically increases with increasing of the laser intensity. The increase of the phase shift is related to the increase of the refractive index. In principle, we may extract the information on the modulation of refractive index from the modulation of the transmitted pulses due to the nonlinear effects. Furthermore, it may be possible to access the nonlinear polarization itself. However, the deviation of the intense and weak transmitted pulses is a rather complicated quantity since the nonlinear effects are intricately integrated during the field propagation through the 10 $\mu$m thinfilm. Thus, it is not obvious how to extract the nonlinear nature from the transmitted laser pulses.

### 6.3.2  Nonlinear polarization

One strong point of the real-time TDDFT simulation is possibility to directly access the microscopic information within a subnanometer scale in space and a subfemtosecond scale in time. Here, we investigate the nonlinear polarization induced by the field in the thin SiO$_2$ film.

As results of the above TDDFT simulations, we obtained the vector potential $\boldsymbol{A}(x,t)$ and the current density $\boldsymbol{J}(x,t)$ as functions of time $t$ and macroscopic coordinate $x$. The electromagnetic fields, $\boldsymbol{E}(x,t)$ and $\boldsymbol{B}(x,t)$, and the polarization $\boldsymbol{P}(x,t)$ can be derived from $\boldsymbol{A}(x,t)$ and $\boldsymbol{J}(x,t)$. To investigate the nonlinear polarization $\boldsymbol{P}_{NL}(x,t)$, we need to subtract the linear polarization $\boldsymbol{P}_L(x,t)$ from the full polarization $\boldsymbol{P}(x,t)$.

To obtain the linear polarization, we consider an additional TDDFT calculation for electron dynamics in a unit cell of $\alpha$-quartz under a certain external electric field $\boldsymbol{E}_{ext}(t)$. If we take the electric field $\boldsymbol{E}(x,t)$ at a certain point of the sample $x = x_m$ as the external electric field $\boldsymbol{E}_{ext}(t) = \boldsymbol{E}(x_m,t)$, the electron dynamics of the additional TDDFT calculation is nothing but the electron dynamics at
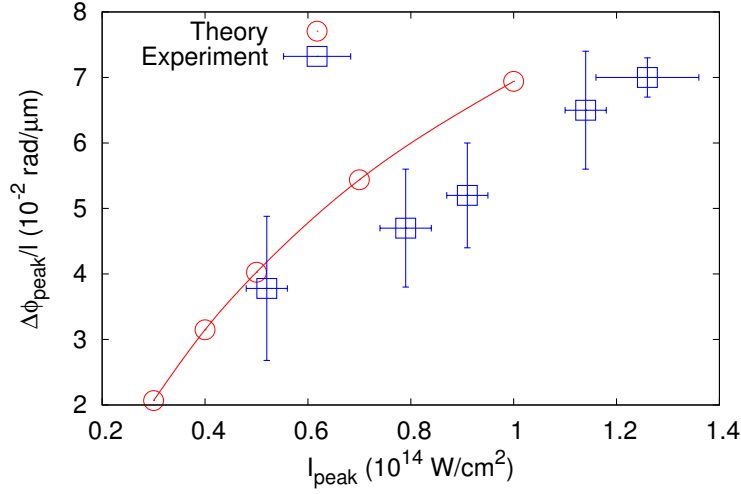
Figure 6.4: Phase shift of transmitted laser pulses as a function of laser intensity. Red-circle shows the theoretical results, and blue-square shows the experimental results [146, 147].

$x = x_m$ in the original TDDFT calculation. If we take the electric field of the original calculation $\boldsymbol{E}(x = x_m, t)$ as the external field of the additional calculation with a sufficiently small scaling factor $\beta$, $\boldsymbol{E}_{ext}(t) = \beta \boldsymbol{E}(x_m, t)$, the results of the additional calculation may only include the linear response and provides the linear polarization $\boldsymbol{P}_L(t) = \int dt' \chi^{(1)}(t - t')\boldsymbol{E}_{ext}(t')$. By subtracting the linear polarization of the additional simulation from the full polarization of the original simulation, we may extract the nonlinear polarization as follows:

$$\boldsymbol{P}_{NL}(x = x_m, t) = \boldsymbol{P}(x = x_m, t) - \beta^{-1}\boldsymbol{P}_L(t). \tag{6.3}$$

We can choose any points in the thinfilm as $x_m$ and extract the nonlinear polarization $\boldsymbol{P}_{NL}(x = x_m, t)$ at any points. We set $x_m$ to the middle point of the thinfilm ($x_m = 5$ $\mu$m) as an example, and extract the nonlinear polarization for several laser intensities. We choose the scaling factor $\beta$ by $\beta^{-1} = \sqrt{I/I_0}$, where $I$ is the peak intensity of the incident pulse and $I_0$ is set to $1 \times 10^{11}$ W/cm$^2$.

Figure 6.5 shows the nonlinear polarization $P_{NL}(x = x_m, t)$ at the middle point of the thinfilm as a function of time. Red-solid line shows the nonlinear polarization induced by the laser pulse with the incident intensity of $5 \times 10^{13}$ W/cm$^2$, and green-dashed line shows the electric field at the middle point of the thinfilm. As seen from the figure, the nonlinear polarization shows the higher frequency oscillation after the pulse peak at around 10 fs, while it does not show such higher frequency components in the earlier half part ($t < 10$ fs). The high frequency components of the nonlinear polarization reflect the existence of excited electrons induced by the laser field. Before the time when the laser field reach the peak amplitude, electrons are not excited since the field strength is not enough. Once the field amplitude becomes strong enough, electrons are excited by the field and the high frequency component of the nonlinear polarization is induced by the interference of conduction and valence states.

In order to investigate the nonlinear polarization in detail, we focus on the fundamental frequency component of the nonlinear polarization, removing the high frequency components by the Fourier
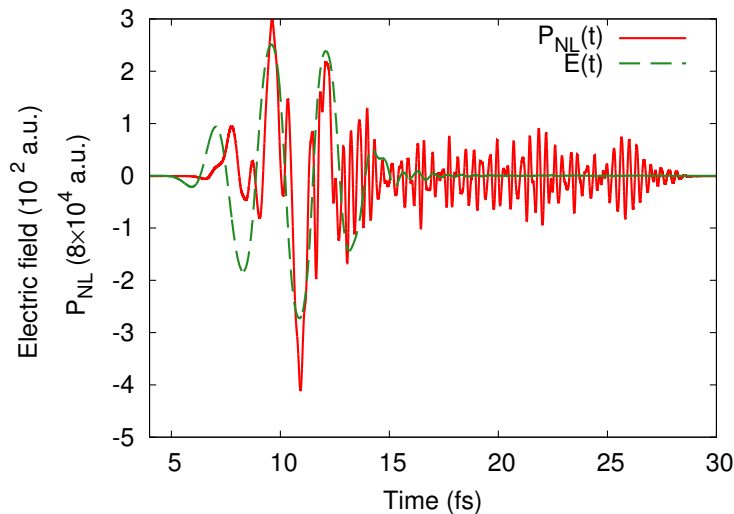
Figure 6.5: Nonlinear polarization at the middle point of sample as a function of time. Red-solid line shows the nonlinear polarization induced by the laser pulse whose incident intensity is $5 \times 10^{13}$ W/cm$^2$, and green-dashed line shows the electric field of the laser pulse.

filtering: First, we compute the Fourier transformation of the nonlinear polarization,

$$\tilde{P}_{NL}(\omega) = \int_{-\infty}^{\infty} dt e^{i\omega t} P_{NL}(t). \tag{6.4}$$

Then, we compute the inverse Fourier transformation with a filter function $M(\omega)$

$$\bar{P}_{NL}(t) = \frac{1}{2\pi} \int_{-\infty}^{\infty} d\omega \tilde{P}_{NL}(\omega) M(\omega). \tag{6.5}$$

We employ the simple step function $\Theta(x)$, which is 1 if $x > 0$ and 0 otherwise, as the filter function $M(\omega) = \Theta(\omega_c - |\omega|)$ and set the cutoff frequency $\omega_c$ to 3.7 eV/$\hbar$. We note that the cutoff frequency is between the fundamental frequency of the laser pulse is 1.55 eV/$\hbar$ and the third harmonics 4.65 eV/$\hbar$.

Figure 6.6 shows the fundamental frequency component of the nonlinear polarization at the middle point of the thinfilm as a function of time. Red-solid line shows the fundamental frequency component of the nonlinear polarization induced by the laser pulses with the incident intensity of $5 \times 10^{13}$ W/cm$^2$ and green-dashed line shows the electric field of the laser pulse. One sees that the fundamental frequency component of the nonlinear polarization exists only during the laser irradiation and disappears after the laser field ends. The nonlinear polarization oscillates almost in phase with the electric field. Reflecting the nonlinearity, the amplitude of the nonlinear polarization is not proportional to the applied electric field. When the amplitude of the electric field becomes about half of its peak amplitude, that of the nonlinear polarization becomes much smaller than the half of its peak amplitude. The inset of Fig. 6.6 shows the enlarged view of the nonlinear polarization and the electric field. One sees that there exists the time delay between the nonlinear polarization and the electric field; the delay is about 100 as. The existence of the time delay indicates the energy transfer from the laser field to electrons since the energy transfer rate is determined by $\dot{\boldsymbol{P}}(t) \cdot \boldsymbol{E}(t)$.

85
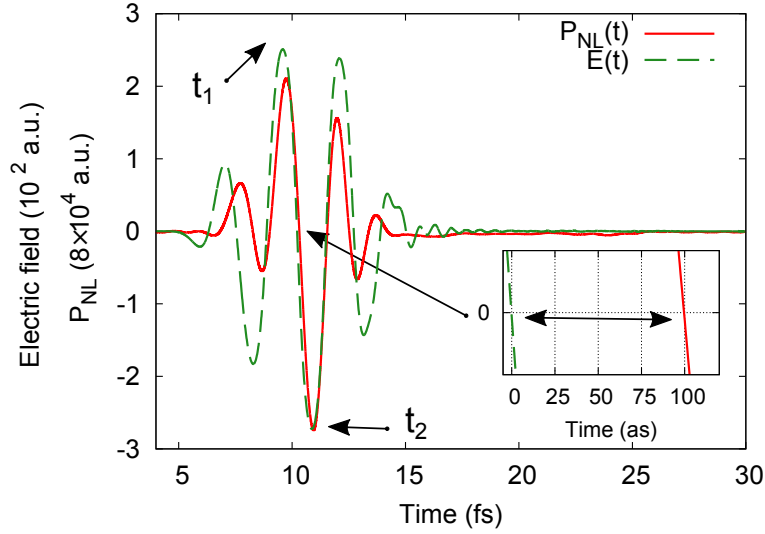
Figure 6.6: Fundamental frequency component of the nonlinear polarization at the middle point of sample as a function of time. Red-solid line shows the fundamental frequency component of the nonlinear polarization induced by the laser pulse whose incident intensity is $5 \times 10^{13}$ W/cm$^2$, and green-dashed line shows the electric field of the laser pulse.

By using the nonlinear polarization, we may evaluate the modification of the refractive index under some assumptions (see Appendix B). The modification of the refractive index $\Delta n$ may be evaluated by

$$\Delta n = \frac{2\pi}{n_0} \frac{\bar{P}_{NL}^{peak}}{E^{peak}}, \tag{6.6}$$

where $n_0$ is the refractive index without fields, $\bar{P}_{NL}^{peak}$ is the peak amplitude of the fundamental frequency component of the nonlinear polarization, and $E^{peak}$ is the peak amplitude of the electric field. The refractive index of $\alpha$-quartz is about 1.5 for the fundamental frequency of 1.55 eV/$\hbar$.

Figure 6.7 shows the maximum modification of the refractive index at the middle point of the thinfilm as a function of the incident laser intensity. The modification of the refractive index increases as the intensity increases. It reaches about $1.15 \times 10^{-2}$, which is about 0.75% of the original value $n_0 = 1.5$, at the laser intensity of $1 \times 10^{14}$ W/cm$^2$, which is slightly below the experimental damage threshold of $1.3 \times 10^{14}$ W/cm$^2$ [146, 147]. Thus, we could conclude that the maximum modulation of the refractive index below the damage threshold intensity is about 1%. After simple mathematics, we have the relation between the modification of refractive index $\Delta n$ and the induced phase shift of the transmitted laser pulse $\Delta \phi$,

$$\Delta \phi = \frac{\omega}{c} \Delta n L, \tag{6.7}$$

where $\omega$ is the carrier frequency and $L$ is the sample thickness. By using this formula, the modification of the refractive index of $1.15 \times 10^{-2}$ gives the phase shift of $9 \times 10^{-2}$ rad/$\mu$m. Although the phase shift of $9 \times 10^{-2}$ rad/$\mu$m is simply evaluated from the nonlinear polarization only at the middle point

of the thinfilm, it shows fair agreement with the actual phase shift of $7 \times 10^{-2}$ rad/$\mu$m for the laser pulse of $1 \times 10^{14}$ W/cm$^2$ in Fig. 6.4. This coincidence indicates that the modulation of the refractive index at different points in the thinfilm are similar to each other and their averaged value can be well approximated by that of the middle point of the thinfilm.
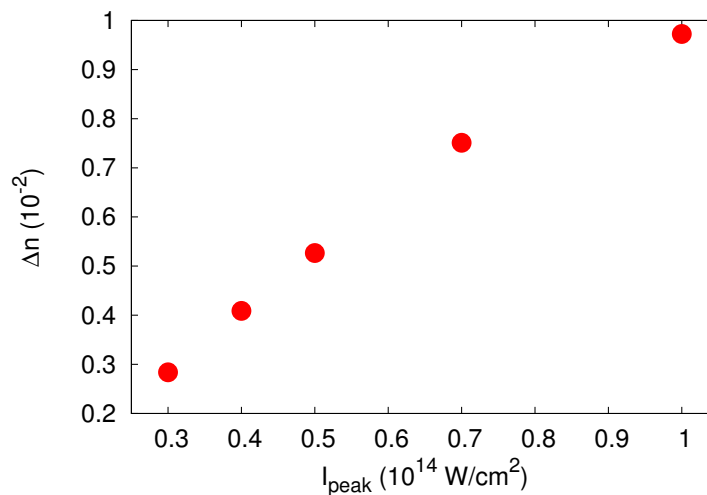


Figure 6.7: Maximum modification of refractive index due to strong fields at the middle point of the thinfilm as a function of incident laser intensity.

We then investigate the local intensity dependence of the modulation of refractive index. We define the local intensity of the laser field by $I_{local-peak} = c n_0 |E^{peak}|^2 / 8\pi$. Figure 6.8 shows the modification of the refractive at the middle point of the thinfilm as a function the local laser intensity, $I_{local-peak}$. The modification based on the Kerr effect, $\Delta n = n_2 I_{local-peak}$, is also shows by blue-dashed line. We used the nonlinear refractive index $n_2$ of $0.6 \times 10^{-16}$ cm$^2$/W, which is an experimental value [146, 147]. While the modification based on the Kerr effect is proportional to the local laser intensity, the modification based on the multi-scale TDDFT simulation shows the superlinear behavior. This fact clearly indicates that higher order nonlinear effects beyond the Kerr effect become significant even below the damage threshold.

We next investigate the time delay between the nonlinear polarization and the electric field, which was shown in the inset of Fig. 6.6. We define the time delay as the difference of the peak times of the nonlinear polarization and the electric field. Figure 6.9 shows the time delay as a function of the laser intensity. The time delay monotonically increases as the laser intensity increases, indicating the increase of the energy transfer from the laser fields to the electronic system. The time delay reaches about 160 as for the laser field of $1 \times 10^{14}$ W/cm$^2$. This result indicates possibility of the real-time measurement of the time delay by using attosecond pulses, whose pulse width can be shorter than 100 as, since the time delay can be larger than 100 as below the damage threshold.

### 6.3.3 Energy transfer from light to medium

The energy transfer from the laser fields to the electronic system is indicated by the time delay of the nonlinear polarization. Here, we investigate the energy transfer in the time domain. We compute the
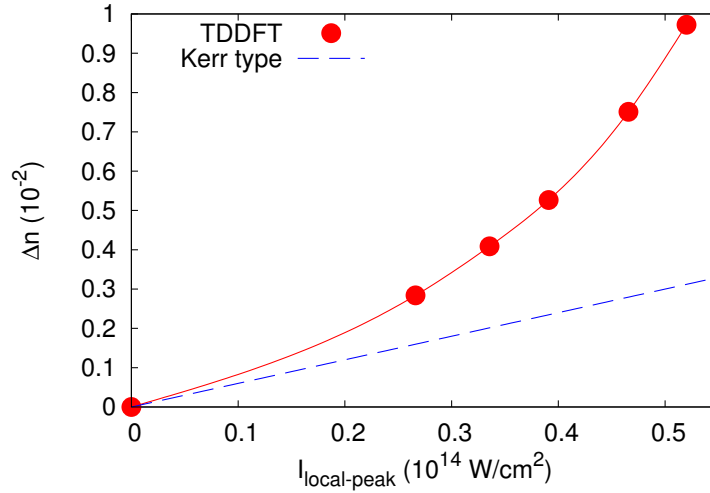
Figure 6.8: Local laser intensity dependence of refractive index modification due to strong fields at the middle point of the thinfilm.

transferred energy as a function of time by

$$W_{NL}(t) = \int_{-\infty}^{t} dt' \frac{d\bar{\boldsymbol{P}}_{NL}(t')}{dt'} \cdot \boldsymbol{E}(t'). \tag{6.8}$$

We note that the linear polarization does not contribute to the permanent energy transfer since the fundamental frequency 1.55 eV/$\hbar$ is much lower than the band gap of $\alpha$-quartz. Furthermore, the higher frequency components also do not contribute the permanent energy transfer since the electric field has no such higher frequency component. If we add the linear polarization and the higher frequency components of the nonlinear polarization to the polarization $\bar{\boldsymbol{P}}_{NL}$, Eq. (6.8) coincides with the equation of the electronic excitation energy (4.7) since the polarization $\boldsymbol{P}(t)$ is nothing but the time integral of the electric current $\boldsymbol{J}(t)$. This clearly means that Eq. (6.8) gives the energy transfer through the nonlinear polarization in the time domain.

Figure 6.10 shows the energy transfer from the laser fields to the electronic system as a function of time. Figure 6.10 (a) shows the simulated transferred energy by using Eq. (6.8), and (b) shows the experimental results [146, 147]. In both panels, results for different laser intensities are shown as solid lines with different colors. In the bottom of the panel, the intensity profile of the laser pulses is also shown as black-solid lines. As seen from both panels, the theoretical results show good agreement with the experimental results. Experimentally, the energy transfer at the middle point of the thinfilm is extracted from the time-profile of the transmitted laser pulses under some assumptions. In contrast, we directly calculated the energy transfer based on the microscopic electron dynamics at the middle point of the thinfilm without any assumptions. Thus, the agreement of theoretical and experimental results validate the assumptions of the experimental extraction.

As seen from the figure, the amount of the permanent energy transfer after the laser fields end increases as the laser intensity increases. This behavior is predicted by the increase of the attosecond time delay of the nonlinear polarization in Fig. 6.9. One may see that there appears the temporal energy transfer only during the laser irradiation. The temporal energy transfer has the similar time
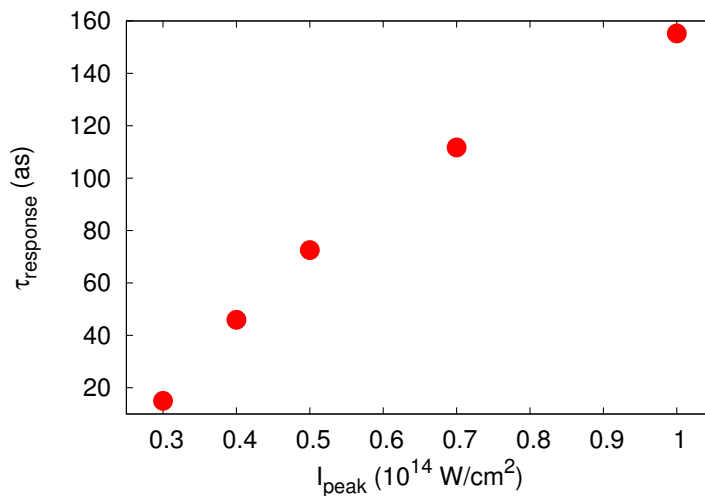
Figure 6.9: Laser intensity dependence of the time delay of the nonlinear polarization.

profile of the field intensity profile and disappear after the laser fields end. The permanent energy transfer is related to the particle-hole pair creation, which corresponds to the population transfer from valence bands to conduction bands. The temporal energy transfer is related to the (quasi) adiabatic dynamics following the modified ground state by the field. Thus, the temporal energy transfer does not cause the population transfer from the valence bands to the conduction bands.

### 6.3.4 Electron density dynamics in $\alpha$-quartz

Finally, we investigate the microscopic electron dynamics in $\alpha$-quartz under a laser electric field to understand the origin of the polarization dynamics. Figure 6.11 (a) shows the electron density in the ground state. One silicon atom and one oxygen atom are on the plane, and their positions are described by the allows. The electron density is high around the oxygen atom, while that is low around the silicon atom. Figures 6.11 (b) and (c) show the density differences from the ground state at the middle point of the thinfilm induced by the laser pulse with the incident intensity of $5.0 \times 10^{13}$W/cm$^2$. The panel (b) shows the induced density difference at the time $t_1$ of Fig. 6.6 when the electric field upwards, while the panel (c) shows the density difference at the time $t_2$ when the electric field downwards. One sees that the density difference is induced only around the oxygen atom but not induced around the silicon atom. The induced density difference around the oxygen atom shows a dipole-like distribution. The direction of the dipole-like distribution is inverted by the inversion of the field direction.

In order to investigate the nonlinearity of the induced density difference $\delta\rho(\boldsymbol{r},t)$ in detail, we consider the following expansion of the induced density difference,

$$\begin{aligned}\delta\rho(\boldsymbol{r},t) &= \int dt'\chi_\rho^{(1)}(\boldsymbol{r},t-t')E(t') + \int dt'dt''\chi_\rho^{(2)}(\boldsymbol{r},t-t',t-t'')E(t')E(t'')\\ &+ \int dt'dt''d'''\chi_\rho^{(3)}(\boldsymbol{r},t-t',t-t'',t-t''')E(t')E(t'')E(t''') + \cdots,\end{aligned} \quad (6.9)$$

where $E(t)$ is the applied electric field, and $\chi_\rho^{(i)}$ is the $i$th-order (non)linear density response function.

89
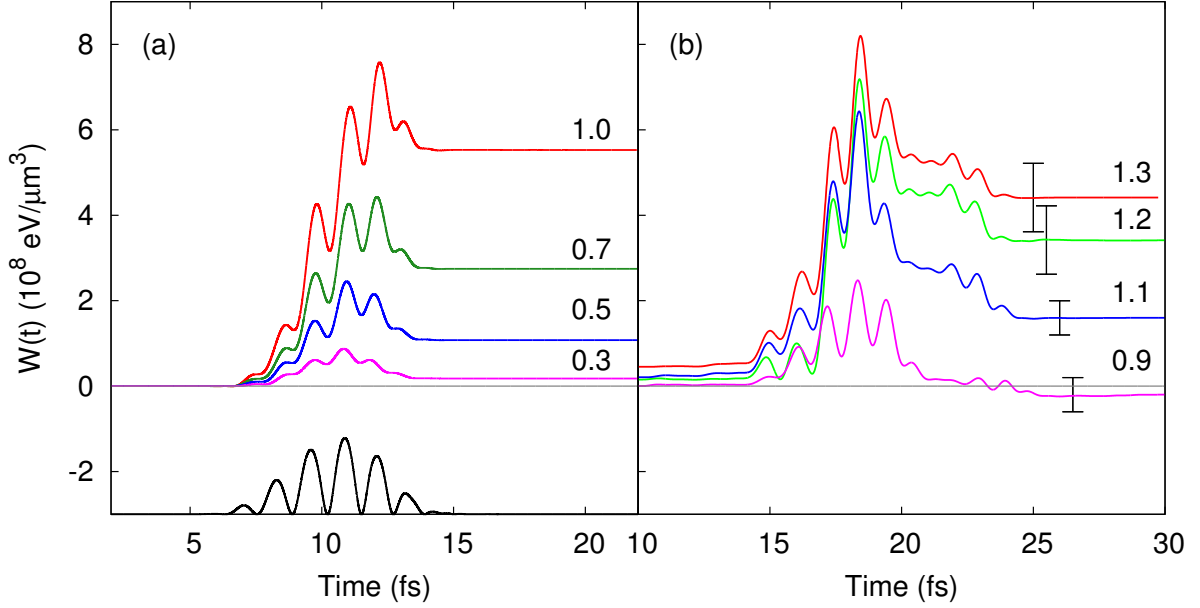
Figure 6.10: Energy transfer from the laser pulses to the solid in the time domain. Left panel shows the simulated result, and right panel shows the experimental result [146, 147]. In the left bottom panel, the time profile of the laser field intensity is shows as a black-solid line. In both the panels, the incident laser intensities are described in the unit of $10^{14}$ W/cm$^2$.

Based on this expansion, we decompose the induced density difference into three components: One is the linear response term $\rho_L(\boldsymbol{r}, t)$. Another is the even-order nonlinear response term $\rho_{NL-even}(\boldsymbol{r}, t)$. The other is the odd-order nonlinear response term $\rho_{NL-odd}(\boldsymbol{r}, t)$. These terms are defined as follows:

$$\rho_L(\boldsymbol{r}, t) = \int dt' \chi_\rho^{(1)}(\boldsymbol{r}, t - t') E(t'), \tag{6.10}$$

$$\begin{aligned}
\rho_{NL-even}(\boldsymbol{r}, t) &= \int dt' dt'' \chi_\rho^{(2)}(\boldsymbol{r}, t - t', t - t'') E(t') E(t'') \\
&+ \int dt' dt'' dt''' dt'''' \chi_\rho^{(4)}(\boldsymbol{r}, t - t', t - t'', t - t''', t - t'''') E(t') E(t'') E(t''') E(t'''') + \cdots,
\end{aligned} \tag{6.11}$$

$$\rho_{NL-odd}(\boldsymbol{r}, t) = \int dt' dt'' dt''' \chi_\rho^{(3)}(\boldsymbol{r}, t - t', t - t'', t - t''') E(t') E(t'') E(t''')$$
$$+ \int dt' dt'' dt''' dt'''' dt''''' \chi_\rho^{(5)}(\boldsymbol{r}, t - t', t - t'', t - t''', t - t'''', t - t''''') E(t') E(t'') E(t''') E(t'''') E(t''''') + \cdots. \tag{6.12}$$

We note that the even-order nonlinear responses do not exist in the nonlinear polarization $\boldsymbol{P}_{NL}$ in $\alpha$-quartz if the applied electric field is parallel to the $c$-axis of the crystal because of the crystal symmetry. In contrast, the induced density difference $\delta\rho(\boldsymbol{r}, t)$ may have the even-order nonlinear components even if the polarization of the laser field is parallel to the $c$-axis.
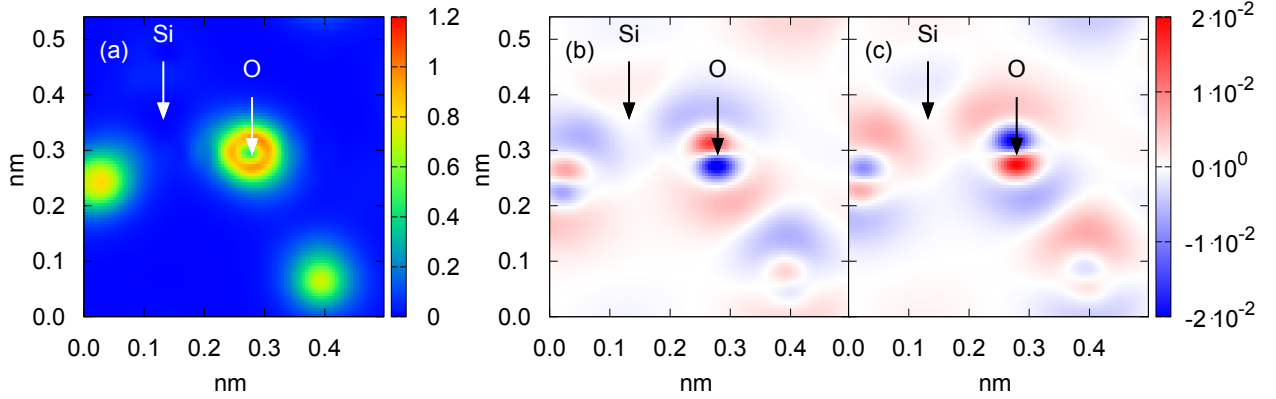
Figure 6.11: Microscopic electron dynamics in $\alpha$-quartz. The panel (a) shows the electron density in the ground state on a plane. The plane is chosen so as to be parallel to $c$-axis of $\alpha$-quartz and so that one silicon atom and one oxygen atom are on the plane. The positions of silicon and oxygen atoms are described the arrows. The panels (b) and (c) show the density differences from the ground state at the middle point of the thinfilm induced by a laser pulse whose incident intensity is $5 \times 10^{13}$ W/cm$^2$. Red means the increase of the density, and blue means the decrease. The panel (b) shows the density difference at the time when the laser electric field upwards with the maximum amplitude, and the panel (c) shows the density difference at the time when the laser electric field downwards.

We decompose the induced density difference in Fig. 6.11 into the three components, $\rho_L(\boldsymbol{r}, t)$, $\rho_{NL-even}(\boldsymbol{r}, t)$ and $\rho_{NL-odd}(\boldsymbol{r}, t)$. Figure 6.12 shows the decomposed density differences at the time $t_1$ of Fig. 6.6 when the electric field upwards. Figure 6.12 (a) shows the linear response contribution $\rho_L(\boldsymbol{r}, t_1)$, (b) shows the even-order nonlinear response contribution $\rho_{NL-even}(\boldsymbol{r}, t_1)$, and (c) shows the odd-order nonlinear response contribution $\rho_{NL-odd}(\boldsymbol{r}, t_1)$. One sees that the linear response $\delta\rho_L(\boldsymbol{r}, t_1)$ in the panel (a) looks almost the same as the density difference $\delta\rho(\boldsymbol{r}, t_1)$ in Fig. 6.11 (b). Moreover, the absolute value of the linear response in the panel (a) is much larger than those of the nonlinear responses in the panels (b) and (c). These facts indicate that the linear response contribution is dominant in the induced density difference. This is consistent with the fact that the linear polarization is dominant in the dielectric response: The nonlinear polarization induces only 1% modification of the refractive index below the damage threshold.

As seen from Fig. 6.12 (a), the linear response contribution of the induced density difference $\delta\rho_L(\boldsymbol{r}, t)$ shows the dipole-like distribution around the oxygen atom, but does not have any responses around the silicon atom. This fact indicates that the linear polarization in $\alpha$-quartz originates from the dipole-like oscillation of electron density around oxygen atoms. Similarly, the even-order nonlinear contribution in Fig. 6.12 (b) shows the quadrupole-like distribution around the oxygen atom. Probably, this is dominated by the second order nonlinear response. As mentioned above, the even-order nonlinear density modifications cannot contribute the polarization since the polarization does not contain the even orders due to the crystal symmetry in the present condition. In contrast, the odd-order nonlinearity in Fig. 6.12 (c) shows complex behavior. One might find the dipole and/or octupole-like density distribution around the oxygen atom. However, unlike the dipole-like feature in $\delta\rho_L(\boldsymbol{r}, t)$ and the quadrupole-like feature in $\delta\rho_{NL-even}(\boldsymbol{r}, t)$, the multipole-like feature is not clear in the odd-order nonlinearity $\delta\rho_{NL-odd}(\boldsymbol{r}, t)$. This can be explained by the symmetry breaking due to the crystal field.

91

The ionic potential would have spherical symmetry near the oxygen atom and the electron dynamics around there could be well described by the multi-pole expansions. Thus, there clearly appear the dipole and quadrupole-like distributions near the oxygen atom. In the highly nonlinear regime, the range of the density modifications extend to the spatial region far from the atoms and could be affected by the crystal potential which breaks the spherical symmetry of the atom. Thus, the density modification of the odd-order nonlinear contributions does not clearly show the multipole-like feature but show the complex behavior. Nevertheless, as seen from these figures, we may conclude that the electron motion around oxygen atoms mainly contributes to the dielectric response of $\alpha$-quartz to applied electric fields and that around silicon atoms does not contribute much.

## 6.4 Summary

We have investigated the nonlinear interactions of ultra-short laser pulses whose intensities are slightly below the damage threshold of the medium with the thin $SiO_2$ ($\alpha$-quartz) film (10 $\mu$m thickness). We have simulated the irradiation of femtosecond laser pulses into the thinfilm based on the time-dependent density functional theory (TDDFT) coupling with the Maxwell's equation. Analyzing the transmitted laser pulses through the thinfilm, the self-steepening effect and the phase shift due to the nonlinear laser-solid interactions have been observed. These features have also been observed in the experimental results [146, 147]. We analyzed the laser intensity dependence of the phase shift and found that the phase shift monotonically increases as the laser intensity increases. Furthermore, we have compared the simulated results with the experimental ones and found that the simulated phase shifts show quantitative agreement with the experimental ones. The agreement indicates that the present real-time TDDFT calculation succeeds to capture the nonlinear nature of the dielectric response of $\alpha$-quartz.

Then, we have investigated the nonlinear polarization in the time domain. In order to decompose the polarization into the linear and nonlinear parts, we have conducted additional real-time TDDFT calculations. In the additional TDDFT calculations, we have calculated electron dynamics under a laser pulse; The shape of the pulse is the same as the shape of the electric field at the middle point of the thinfilm but the amplitude is scaled to be sufficiently weak so that the additional calculation provides only the linear polarization. By subtracting the obtained linear polarization from the full polarization of the original calculation, the nonlinear polarization at the middle point of the thinfilm has been extracted. The nonlinear polarization induced by the laser pulse with the intensity of $5 \times 10^{13}$ W/cm$^2$ contains the higher frequency components, reflecting the existence of electron-hole pairs induced by the nonlinear excitation processes such as the multi-photon and the tunneling excitation. In order to investigate the properties of the nonlinear polarization, we focused on the fundamental frequency component of it. We have estimated the modification of the refractive index based on the fundamental frequency component of the nonlinear polarization. We found that the maximum modification of the refractive index below the damage threshold intensity is about 1%. Furthermore, we found the time delay between the nonlinear polarization and the applied electric field. We further investigated the laser intensity dependence of the time delay. We have found that the time delay monotonically increases as the laser intensity increases and can be more than 100 as below the damage threshold. The time delay implies the energy transfer from the laser field to the medium, and the increase of the time delay implies the increase of the transferred energy.

We have evaluated the energy transfer through the interaction of the laser fields with the nonlinear polarizations based on the microscopic electron dynamics. The simulated result shows nice agreement

with the experimental result [146, 147]. Experimentally, the energy transfer has been extracted from the change of the pulse shape through the thinfilm under some assumptions. On the other hand, the simulated transferred energy is directly calculated from the electron dynamics without any assumptions. Therefore, the agreement between theory and experiment validates the assumptions for experimental extraction of the energy transfer in the time domain. We have found that the transferred energy in the time domain contains two components: One is the permanent energy transfer and the other is the temporal energy transfer. The permanent energy transfer corresponds to the population transfer of electrons from valence bands to conduction bands. On the other hand, the temporal energy transfer corresponds to the modification of the stable electronic structure, or polarized states. For weaker laser pulses, the only temporal energy transfer appears but the permanent energy transfer does not. The ratio of the permanent energy transfer to the temporal energy transfer increases as the laser intensity increases.

Finally, we have investigated the microscopic origin of the dielectric response of $\alpha$-quartz based on the electron dynamics in a subnanometer scale. In the ground state, the electron density around oxygen atoms is much higher than that around silicon atoms. Reflecting this density profile, dielectric responses of $\alpha$-quartz are dominated by the motion of electrons around the oxygen atoms. We found that the linear polarization originates from the dipole-like density modification around the oxygen atoms (Fig. 6.12 (a)). The microscopic origin of the nonlinear polarization is rather complex, reflecting the symmetry breaking due to the crystal field. The nonlinear polarization in $\alpha$-quartz could originate from dipole and/or octupole-like density modification around the oxygen atoms (Fig. 6.12 (c)).
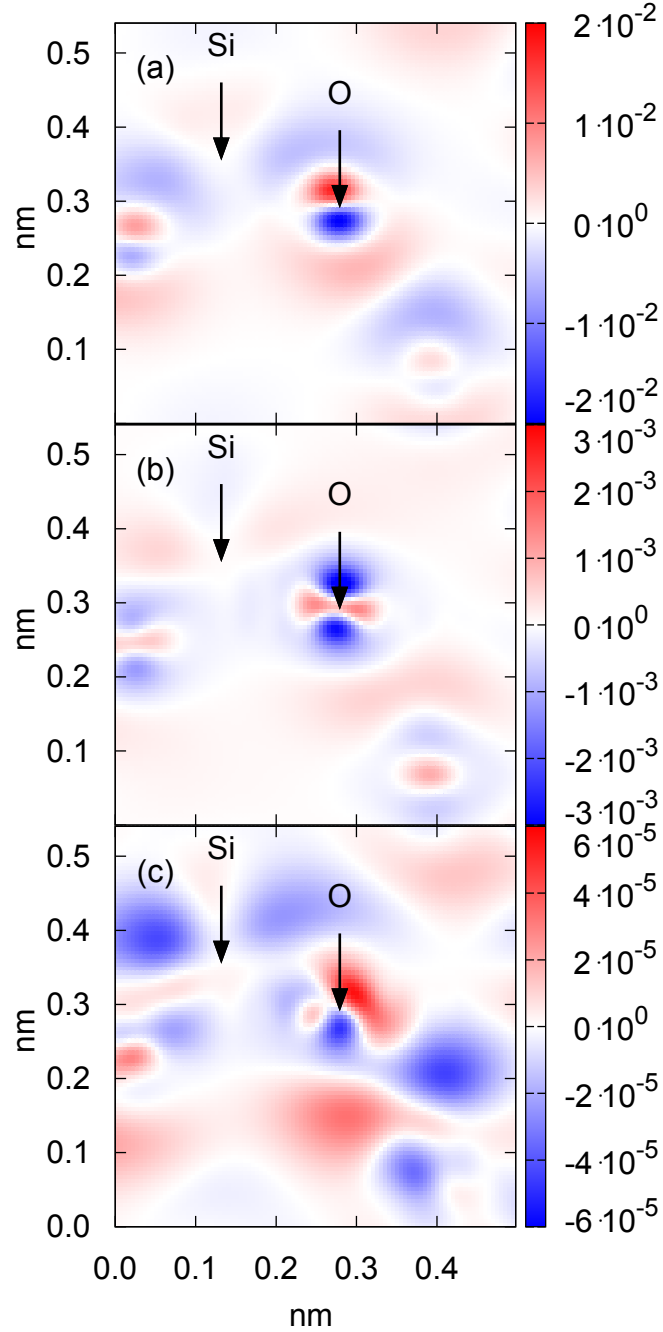
Figure 6.12: Nonlinear electron density modification in $\alpha$-quartz. The panel (a) shows the linear response contribution $\delta\rho_L(\boldsymbol{r}, t)$. The panel (b) shows the even-order nonlinear contribution $\delta\rho_{NL-even}(\boldsymbol{r}, t)$. The panel (c) shows the odd-order nonlinear contribution $\delta\rho_{NL-odd}(\boldsymbol{r}, t)$.

# Chapter 7

# Femtosecond-laser-induced damage phenomena

## 7.1    Introduction

Ablation of surfaces by intense femtosecond laser pulses is potentially a useful tool for material machining as well as preparation of nanosized particles [36, 41, 149–160]. It is important to have good models of the energy deposition and the ablation process to set up the pulse protocols for the purpose in mind. However, it is not easy to model the laser-target interaction because one has to deal with the quantum physics at the atomic scale together with the pulse propagation at a mesoscopic scale.

There is a large literature on the modeling of the laser-target interaction dynamics [134, 150, 158, 161–165] as reviewed in Ref. [41] as well as Ref. [37]. The fundamental physics is the excitation of particle-hole pairs, often parameterized by Keldysh's approximate formulas [121, 160]. The particle and hole carriers affect the electromagnetic response of the insulator, screening the field when their density becomes large. Here the effects are often parameterized by hybrid dielectric functions containing contributions intrinsic to the insulator and plasma contributions from the excited electrons. Both aspects of this electron dynamics are included in the time-dependent density functional theory (TDDFT), which is fully quantum mechanical and doesn't require any specific assumptions about the dynamics. It also gives a good compromise between *ab initio* theory and computational feasibility. In this work we shall apply the dynamic equations of TDDFT to calculate the propagation of short, intense electromagnetic pulses upon insulators and compute the energy transfer to the medium.

In recent work, TDDFT with strong fields has been applied to condensed media in several contexts: coherent phonon generation [98, 99] and high-field interactions with diamond, silicon and quartz [97, 100, 128, 166–168]. In this work, we treat the energy transfer to a crystalline $SiO_2$, $\alpha$-quartz, a material of technological importance. From the transferred energy, we conduct a first systematic investigation of laser-damage and laser-ablation phenomena in the first-principles level. The calculations require high-performance computers, so our goal is to also analyze the results in terms of simpler models that can be easily applied. We only discuss the deposited energy of the pulse, which is the most important determinant of the subsequent atomic dynamics. Since TDDFT employing practically usable functionals does not have any relaxation processes, it is limited to short-time dynamics. The main limitations to consider are the electron-electron kinetic relaxation time $\tau_{ee}$, the full electron thermalization time, and the electron-phonon equilibration time. The latter two processes have time scale much larger than 100 fs, which is well beyond the time domain considered here. Estimates of $\tau_{ee}$

range from 1 fs to 100 fs [158, 159, 169, 170]. Fortunately for the modeling by TDDFT, the response of insulators to high fields is rather insensitive to the kinetic equilibration [171]. We note that on very long time scales another mechanism that is missing from TDDFT becomes important, namely an avalanche of electrons in the free carrier bands [135].

## 7.2 Method

The theory and its implementation used in this chapter have been described in Sec. 2.3 and Sec. 3.5. In order to describe the coupled dynamics of electrons in the medium and propagation of electromagnetic fields, we simultaneously solve the time-dependent Kohn-Sham equation (2.56) for electron dynamics and the Maxwell's equation (2.55) for electromagnetic fields. In this study, we simulate irradiation of high-intensity ultra-short laser pulses at normal incidence on the $\alpha$-quartz surface. We take the propagation direction as $x$-axis and denote the depth from the surface as $x$. As results of the simulations, electromagnetic fields, $\boldsymbol{E}(x,t)$ and $\boldsymbol{B}(x,t)$, and electric current, $\boldsymbol{J}(x,t)$, are obtained as functions of time $t$ and space $x$.

For a quantitative description of the laser-damage process, theoretical inputs should meet the following demands. First it is important that the band gap is described reasonably, since the number of photons required to excite electrons across the band gap is a crucially parameter for electronic excitations. It is also important that the dielectric function at around the laser frequency, 1.55 eV in most measurements, should be described reasonably. In this work we use a modified Becke-Johnson exchange potential (mBJ) [110] with a LDA correlation potential [106] in the adiabatic approximation. We note that the mBJ potential coincides with the meta-GGA potential of Eq. (2.67) if the parameter $c_m$ is set to 1. We show in Fig. 7.1 real and imaginary parts of the dielectric function. The calculated indirect band gap with this potential is 1.3 eV lower than the experimental gap of 8.9 eV, but more relevant to electromagnetic interactions is the optical gap. This is seen to be 9 eV from the absorptive part of the dielectric function shown in Fig. 7.1, compared to the experimental value of $9 - 10$ eV. The real part of the dielectric function at around 1.55 eV is also described reasonably. We note that there is no long-range exchange-correlation contribution included in the vector potential.

We compute the energy transfer to the medium from the electromagnetic side, since the calculation from the Kohn-Sham densities would require an explicit energy density functional for the mBJ potential. The energy transfer rate $W(x,t)$ is given by

$$W(x,t) = -\boldsymbol{E}(x,t) \cdot \boldsymbol{J}(x,t), \tag{7.1}$$

where $\boldsymbol{E}$ is the electric field associated with the pulse. In comparing different pulse lengths and intensities, we find the most convenient measure of the pulse strength is its fluence $F(x)$ given by

$$F(x) = (c/4\pi) \int dt \hat{x} \cdot \boldsymbol{E}(x,t) \times \boldsymbol{B}(x,t), \tag{7.2}$$

where $x$ is the depth from the surface. With these definitions, the deposited energy density is given by $E_x(x) = -\int dt W(x,t) = -\frac{d}{dx} F(x)$.

Our multiscale calculation uses a one-dimensional grid with spacing of 250 au for propagation of laser electromagnetic fields. At each grid point, electron dynamics is calculated using atomic-scale rectangular unit cell containing 6 Silicon atoms and 12 Oxygen atoms which are discretized into Cartesian grids of $20 \times 36 \times 50$. The dynamics of the 96 valence electrons is treated explicitly; the

effects of the core electrons are taken into account by pseudopotentials [107,108]. Both electromagnetic fields and electrons are evolved with a common time step of 0.02 au.

The laser pulse in the vacuum is described by a gauge field $\boldsymbol{A}(x,t)$ of the form

$$\boldsymbol{A}(x,t) = \hat{z}A_0 \sin^2(\pi t_x/T_p)\cos(\omega t_x) \tag{7.3}$$

in the domain $0 < t_x < T_p$ and zero outside. Here $\omega$ is the photon's angular frequency, $t_x = t - x/c$ describes the space-time dependence of the field, and $T_p$ controls the pulse length. It is related to the usual measure $\tau_p$ (full width at half-maximum intensity) by $\tau_p = 0.364T_p$. Most of the results below were calculated for an average photon energy of $\hbar\omega = 1.55$ eV and the pulse length of $\tau_p = 7$ fs. We follow the pulse from the time its front reaches the surface ($\bar{2}10$) until it has propagated several $\mu$m into the material.
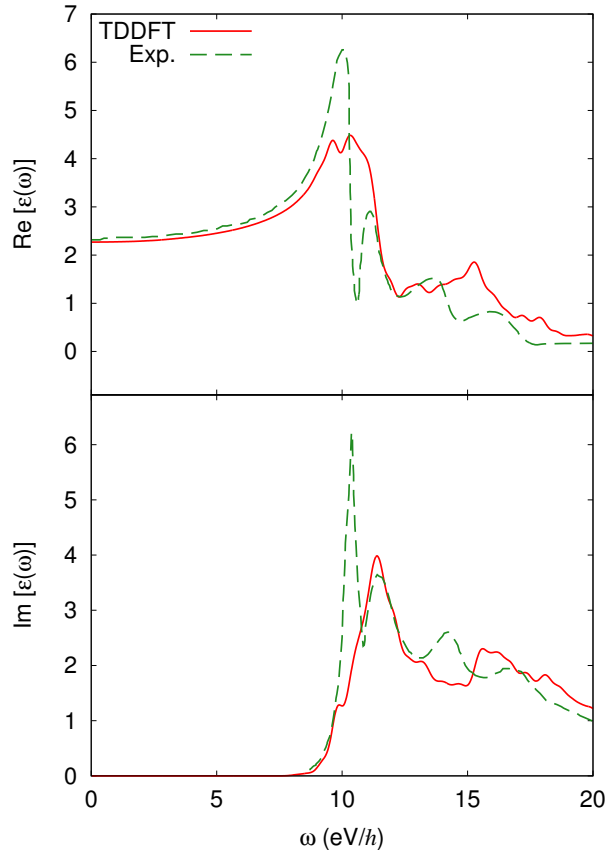


Figure 7.1: Real (a) and imaginary (b) parts of the dielectric function of $SiO_2$ in the direction perpendicular to $c$-axis.

97

## 7.3 Results

We first illustrate the simulation of the laser irradiation on a $\alpha$-quartz surface. Figure 7.2 shows snapshots of the laser propagation. The incident laser pulse in vacuum is propagated on the $\alpha$-quartz surface and splits into two pulses. One is the reflected pulse and the other is the transmitted pulse. We repeat this simulation for several different laser intensities.
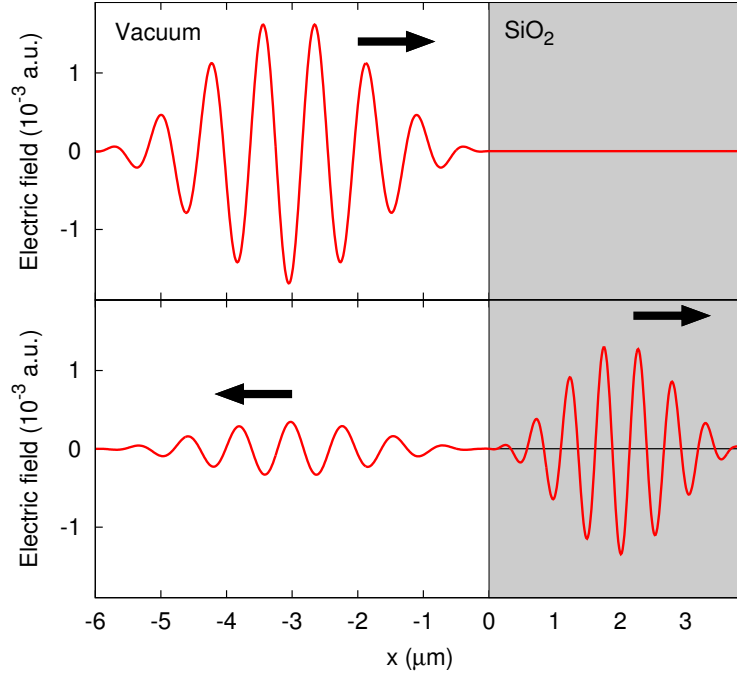
Figure 7.2: Snapshots of propagation of a laser pulse.

We then note that our calculated reflectivity of $\alpha$-quartz, shown in Fig. 7.3, is close to 4% for laser fluence below 1.5 J/cm$^2$ increasing to about 35% at fluence 10 J/cm$^2$. The rise at high field intensity is due to the screening effect of an electron-hole plasma that is formed. The figure shows the reflectivity for both the mBJ potential and the LDA potential [128]. One may see that the screening has a lower threshold for LDA functional. This can be attributed to the lower band gap in the LDA, permitting a more dense plasma to form.

The main quantity we can calculate is the deposited energy $E_x$ as a function of penetration depth $x$. The range of interest extends roughly from the energy required to melt the solid to the energy required to vaporize it. The first transition requires about 0.5 eV/atom in quartz, starting from room temperature. The second transition is not as well defined; we can estimate it as 6 eV/atom either as the heat of formation or from the "atomic-liquid" transition reported in Ref. [172].

A sampling of the results for the multiscale calculation is shown in Figs. 7.3 - 7.10. In Fig. 7.4, we show the deposited energy density at the surface for a range of laser fluences. The threshold for achieving melting is $\sim$ 1.5 J/cm$^2$, while the vaporization threshold as we have defined it is at $\sim$ 2.5 J/cm$^2$. Thus, for applications that physically transform the material, we need to only consider fluences of the order 1.5 J/cm$^2$and and higher. Figure 7.4 shows the deposited energies of lower strength pulses as well, which may be of interest to analyze the parametric dependence of the energy deposition on
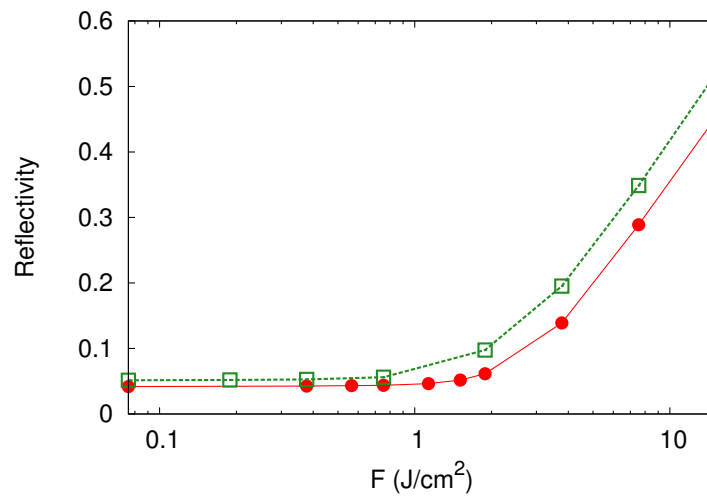
Figure 7.3: Reflectivity at the surface of $\alpha$-quartz as a function of fluence.

the characteristics of the pulse. Figure 7.4 also shows the results for the LDA functional. One sees that lower-fluence pulses are more highly absorbed in LDA . This is to be expected due to the small band gap. The difference becomes small and even changes sign at high fluence. A possible explanation might be an increased screening for the LDA, as was discussed for the reflectivity.

The dependence of $E_x$ on the depth in the medium is shown in Fig. 7.5 for a range of pulse intensities, all with pulse length of $\tau_p = 7$ fs. One sees that the melted region extends to a depth of 0.5-0.6 $\mu$m for the stronger pulses. The depth permitting ablation only extends to 0.13 $\mu$m for a pulse of 10 times the threshold intensity.

Fig. 7.6 compares the pulse profile for the $I_0 = 10^{15}$ W/cm$^2$pulse at two points, in the first cell and in the 80th cell at a depth of 1.06 $\mu$m. At this depth, the intensity has decreased below the melting threshold. One sees that the shapes are quite similar. The main difference is that the attenuation is stronger in the later arriving cycles of the pulse train. This is to be expected; the early part of the pulse creates particle-hole pairs which can then modify the propagation of the rest of the pulse.
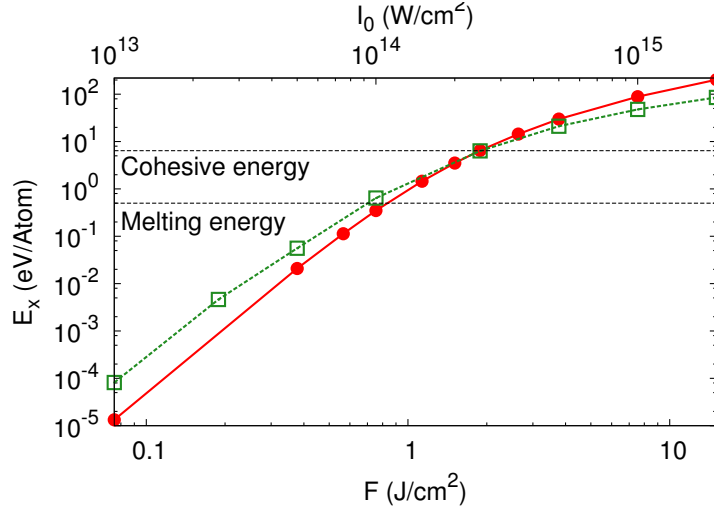
Figure 7.4: Deposited energy $E_x$ at the surface of $\alpha$-quartz is shown, as a function of the fluence and the peak intensity of the pulse. Red circles show results using mBJ potential, while green squares show results using LDA functional [128].
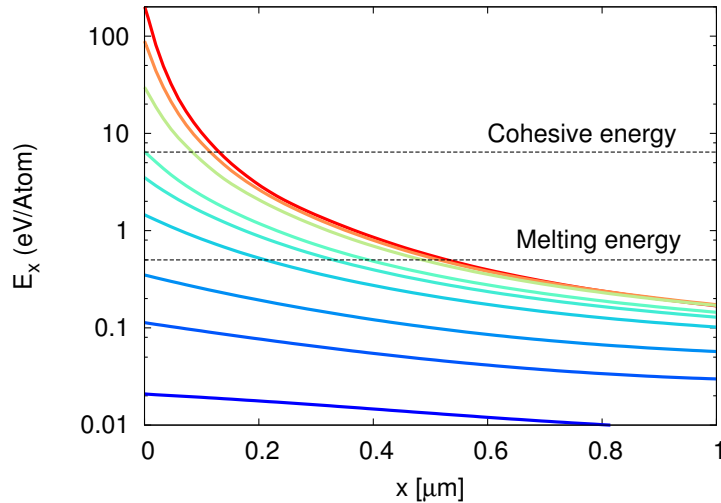


Figure 7.5: Deposited energy $E_x$ in $\alpha$-quartz as a function of distance below the surface. The curves show the results for intensities $I_0 = 0.5, 0.75, 1.0, 1.5, 2.0, 2.5, 5.0, 10.0, 20.0 \times 10^{14}$ W/cm$^2$ from lowest to highest graph. The pulse length is $\tau_p = 7$ fs for all intensities.
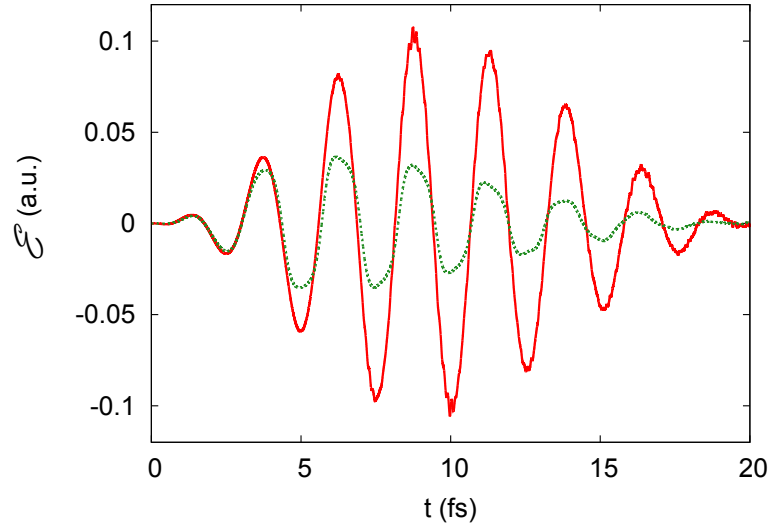
Figure 7.6: Pulse shapes at the first cell and at the 80th cell located at a depth of 1 $\mu$m are shown, for an incident pulse having intensity $I_0 = 10^{15}$ W/cm$^2$and length $\tau_p = 7$ fs.

## 7.4 Approximate description

The mild changes in pulse shape suggest that the energy deposition might be modeled simply as a function of the strength of the pulse as it is attenuated in the medium. To see how well this works, we extract the local fluence of the pulses at the different cells in our simulation. The absorbed energy versus the local fluence at each depth for the range of pulses shown in Fig. 7.5 is plotted in Fig. 7.7. We see that they fall on a common line, extending down to a fluence of 1 J/cm$^2$, well below the damage threshold. Thus, the change in pulse shapes can indeed be neglected, at least for $t_p = 7$ fs pulses. Remarkably, the dependence can be very well fitted following Keldysh's strong-field ionization rate equation [160, Eq. (9)]. An approximate formula expressing the energy deposition in terms of the fluence is

$$E_x = AF^{5/4}\exp(-B/F^{1/2}). \tag{7.4}$$

The two-parameter fit ($A = 70$ eV-(J/cm$^2$)$^{-5/4}$,B= 4.0(J/cm$^2$)$^{1/2}$) is shown as the solid black line in Fig. 7.7. One sees that the fit is valid from fluences from well below the thresholds to the highest calculated. The fit value $B = 4.0$ can be compared to the value obtained from a reduction of Keldysh's exponential factor,

$$B = \pi\tau_p^{1/2}m^{1/2}\varepsilon^{1/4}\Delta^{3/2}/2, \tag{7.5}$$

in atomic units. Taking the reduced mass $m = 1/2$, the direct band gap $\Delta = 9$ eV, and the dielectric constant $\varepsilon = 2.3$, Eq. (7.5) gives $B = 4.2$, a difference of only 5% from the fit value. The multiphoton process is only relevant at much lower fluences that are needed for structural changes.
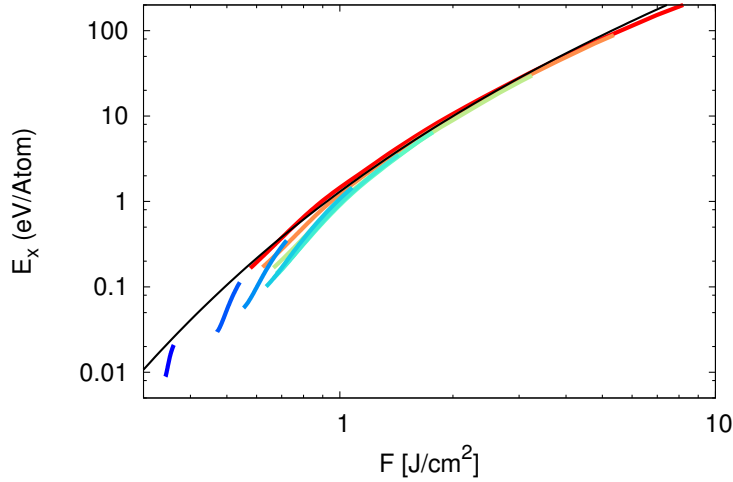
Figure 7.7: Absorbed energy is plotted as a function of local fluence of pulses. Black solid curve shows a fit by Keldysh's formula.

## 7.5 Comparison with experimental data

While it is not entirely clear how energy deposition profiles link to structural changes in the surface region, we can still compare the theory and experiment assuming that the melting and vaporization transitions control the surface damage and ablation. There are many measurements of thresholds for these quantities, but only a few for pulse as short as $\tau_p \sim 20$ fs or below [152, 154, 158, 160]. Fig. 7.8 shows a comparison with the data of Refs. [158, 160] for fused silica. For the damage threshold shown by red symbols, we compare with calculated fluences to achieve $E_x = 0.5$ eV/atom at the surface. We see that the experimental threshold is in qualitative correspondence with that value. The ablation threshold, shown by green symbols, is much lower than predicted by the $E_x = 6$ eV/atom criterion based on the formation of an atomic liquid [172]. This may indicate an importance of nonthermal effects in the ablation process by femtosecond laser pulses [173, 174]. In fact, the reported thresholds for damage and ablation at $\tau_p = 7$ fs in Ref. [158] are nearly identical. This may be seen by the sharp edges of the ablation craters formed at the shortest pulse lengths. Perhaps one needs to consider a different mechanism for ablation at threshold, which may involve the electric fields produced when excited electrons are ejected from the surface. It should also be kept in mind that damage threshold depends on structures of the material; a lower threshold is reported for fused silica than crystalline $SiO_2$ using much longer pulses [175].

We next examine the depth of the ablated craters as a function of the fluence of the pulses. The available experimental data is shown in Fig. 7.9. For the theory, we report the depth at which the deposited energy falls to $E_x = 6$ eV/atom, as in Fig. 7.8. The agreement between theory and experiment is quite satisfactory. The theory reproduces the very sharp rise above threshold as well as the saturation at high fluences.

As a final theory-experiment comparison, we investigate spatial profiles of the craters created by the laser pulses, employing the crater depth as a function of laser fluence in Fig. 7.9. We assume that the depth of the crater depends only on the local fluence of the laser pulses at each position $y$ on the
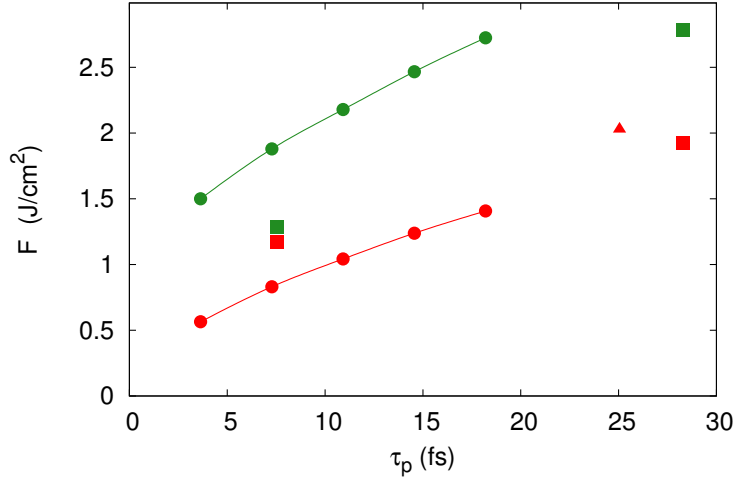
Figure 7.8: Threshold damage and threshold ablation fluences in $SiO_2$ are shown as a function of pulse width $\tau_p$. Red and green circles are the calculated fluences to deposit an energy $E_x = 0.5$ eV/atom corresponding to a damage threshold and an energy $E_x = 6$ eV/atom corresponding to an ablation threshold in $\alpha$-quartz, respectively. Experimental data from Ref. [158] for fused silica is shown with green and red squares; data from Ref. [160] is shown with red triangle.

surface. For the comparison, we employ the Gaussian shape as the beam profile at the solid surface,

$$F(y) = F_{max} e^{-2 \frac{y^2}{w_0^2}}, \tag{7.6}$$

where $F_{max}$ is the maximum laser fluence at the center of the pulse, and $w_0$ is the beam waist. We choose $F_{max}$ and $w_0$ so that the diameter and the depth of the calculated crater profile reproduce the experimental ones [159].

Figure 7.10 shows the crater profiles created by the laser pulses. Red line shows the theoretical estimation and green line shows the experimental results. Here we take the center of the pulse spot as $y = 0$. Figure 7.10 (a) shows the crater created by the relatively weak laser pulse: The diameter of the crater is 3.4 $\mu$m and the depth at center of the spot is 50 nm. For the panel (a), we set ratio of the maximum local fluence $F_{max}$ to the ablation threshold fluence $F_{th}$ to 1.36, and set the beam waist $w_0$ to 4.3 $\mu$m. Experimentally, the fluence ratio $F_{max}/F_{th}$ is 1.15 and the beam waist is 4.5 $\mu$m for the relatively weak case [159]. Figure 7.10 (b) shows the crater created by the relatively intense laser pulse: The diameter is 10.3 $\mu$m and the depth at center of the spot is 100 nm. For the panel (b), we set the fluence ratio $F_{max}/F_{th}$ to 2.63, and set $w_0$ to 7.4 $\mu$m. Experimentally, the fluence ratio $F_{max}/F_{th}$ is 5.5 and the beam waist is 4.5 $\mu$m for the relatively intense case.

As seen from Fig. 7.10 (a), the theoretical crater profile well reproduces the overall structure of the experimental one with the reasonable beam parameters, $F_{max}/F_{th}$ and $w_0$. This fact indicates that depth of craters created by relatively weak laser pulses simply depends only on the local laser fluence. In contrast, as seen from Fig. 7.10 (b), the theoretical crater profile fails to reproduce the experimental one even in a qualitative level. Furthermore, the beam parameters, $F_{max}/F_{th}$ and $w_0$, for the panel (b) are quite different from the experimental ones. This disagreement indicates that spatial
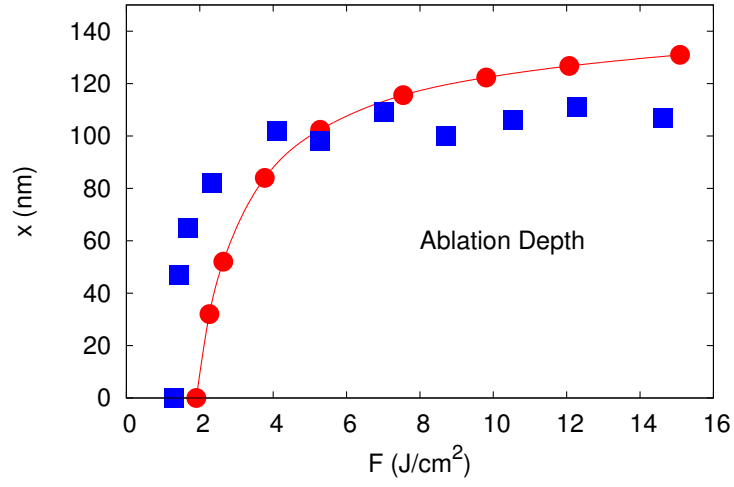
Figure 7.9: Depth of crater formed in $SiO_2$ by single laser pulses of length $\tau_p = 7$ fs, as a function of the fluence of the original pulse. Experiment is shown in blue squares, from Ref. [159]. The red circles show the depth at which the calculated energy deposition falls below $E_x = 6$ eV/atom.

profiles of craters created by relatively intense laser pulses do not locally depend on the fluence profile of the laser pulses but nonlocally. Subsequent atomic dynamics after energy transfer from laser pulses to medium would play a significant role to produce the complicated crater profile for the intense laser irradiation.
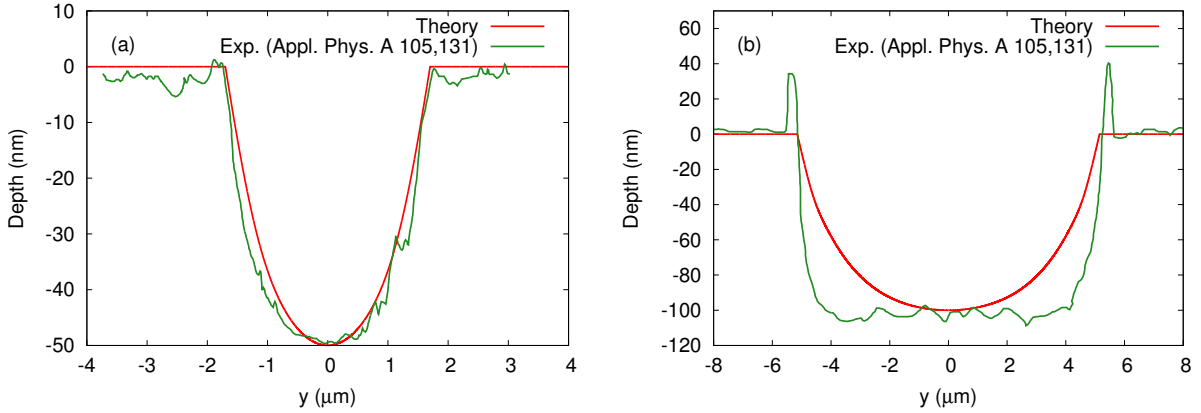
Figure 7.10: Spatial profiles of craters created by femtosecond-laser ablation. Red lines show the theoretical estimation based on the TDDFT, and green lines show the experimental results [159]. The panel (a) shows the craters crated by the relatively weak laser pulse, and (b) shows those created by the relatively intense laser pulse.

## 7.6 Summary of femtosecond-laser-induced damage phenomena

We have shown that it is feasible to calculate the interaction of intense femtosecond laser pulses with insulating media by the TDDFT, avoiding the detailed modeling of plasma formation and dynamics required in earlier theoretical treatments. The threshold for damage is accounted for by the calculated energy deposition needed to melt the quartz substrate. On the other hand, the calculated threshold for ablation via a transformation to an atomic liquid is 50% higher than the low values observed in two experiments. This may suggest the significance of nonthermal mechanism in the ablation process. It may also indicate that another mechanism is responsible for the threshold behavior, such as an electric-field assisted ionic dissociation. However, we find good agreement with experiment on the depth of the ablation taking the energy deposition criterion to estimate the depth. Furthermore, we have estimated the spatial profile of craters created laser pulses. We find that the estimated crater profile shows good agreement with experiment when the intensity of the laser pulse is relatively weak. On the otherhand, the estimated crater profile fails to reproduce the experimental one for the relatively intense laser pulse. This indicates the significance of the post atomic dynamics after the laser irradiation to produce the complicated structure of the ablated crater for the intense laser pulse. It may well be that modeling energy deposition in wide-gap insulators could be greatly simplified once one has a suitable set of benchmark multiscale calculations based on the TDDFT. Since those calculations require much computer time, it would be useful to compare them to existing models [37,41,134,135,150,158,161–165] to validate assumptions in the models and to facilitate improved modeling of the phenomena.

# Chapter 8

# Summary and outlook

In this thesis, we have presented theoretical and numerical methods to investigate nonlinear laser-solid interactions based on the time-dependent density functional theory (TDDFT). Then we have shown applications of the methods to study the following three topics (a) optical properties of highly laser-excited dielectrics, (b) nonlinear polarization induced by high-intensity ultrashort laser pulses in the time domain, and (c) initial stage of the non-thermal laser processing.

We introduced theoretical frameworks that have been employed in this thesis (chapter 2). They are based on the TDDFT and provide first-principles descriptions for laser-solid interactions in two different schemes. One is to explore electron dynamics in a unit cell of crystalline solids under given external electric fields. We call it the *single-cell* simulation. The other is to investigate coupled dynamics of electrons in solids and macroscopic electromagnetic fields, where feedback from the electron dynamics to the fields is treated consistently. We call it the *multi-scale* simulation. In the single-cell simulation, we solve the time-dependent Kohn-Sham equation in the time domain and treat electron dynamics in a unit cell of crystalline solids under spatially-uniform time-varying electric fields without any perturbative expansions for the field strength. Therefore, the single-cell simulation provides fully quantum mechanical and real-time electron dynamics in a unit cell of crystalline solids and is applicable to laser-solid interactions even in strongly nonlinear regimes as well as in the linear response regime. It is suitable to investigate the microscopic mechanism of laser-induced ultrafast phenomena. For example, one can calculate nonlinear polarization induced by intense short laser pulses in a crystalline solid and clarify which atoms/bonds mainly contribute to the nonlinear polarization in a nanometer scale. In the multi-scale simulation, we combine the single-cell simulation for microscopic electron dynamics in solids with the simulation for macroscopic propagation of electromagnetic fields, coupling the time-dependent Kohn-Sham equation with Maxwell's equation. The multi-scale simulation provides a comprehensive description of laser-solid interactions and is suitable to investigate propagation effects of laser pulses and spatial distribution of electronic excitation in a micrometer scale. For example, one can calculate a shape of transmitted laser pulses from thin samples including nonlinear effects such as the optical Kerr effect and the generation of free carriers and can evaluate the spatial distribution of transferred energy from a laser pulse to a solid due to the nonlinear excitation processes such as the multi-photon and tunneling excitations.

We have developed a computational code by ourselves to practically conduct the above single-cell and multi-scale simulations (Chapter 3). We have named the code *Ab-initio Real-Time Electron-Dynamics simulator; ARTED*. The TDDFT simulations in the time domain are computationally expensive since the time-evolution of several tens of thousands of Kohn-Sham orbitals has to be

conducted for several tens of thousands of time steps. Particularly, the multi-scale simulation is much more expensive because several hundreds of different TDDFT simulations for electron dynamics in a unit cell at different macroscopic points have to be conducted simultaneously. Thus, it is necessary both to use large-scale supercomputers like the K computer at RIKEN and to optimize the code for massively parallel-computing in order to conduct the multi-scale simulation. We have implemented the parallel computing in ARTED with the Message Passing Interface (MPI) and OpenMP. Therefore, ARTED can be used with both the Flat-MPI and the MPI+OpenMP hybrid parallel parallelization. We have optimized ARTED for massively parallel computing to employ the large-scale supercomputers. It shows good parallel efficiency and effective performance, even if several tens of thousands of cores are employed for parallel computing.

We have developed theoretical and numerical methods to employ a modern exchange-correlation potentials in the TDDFT simulations in the time domain in order to improve accuracy and reliability of theoretical investigations (Chapter 4). So far, the real-time TDDFT simulation has been applied to investigate nonlinear interactions of intense laser pulses with solids such as dielectric breakdown [97], high-order harmonic generation [176], and coherent phonon [98, 99] as well as the interaction of light with solids in the linear response regime [96]. In these applications, the adiabatic local density approximation (LDA) has only been employed. However, the adiabatic LDA has a serious problem to investigate light-matter interactions: The adiabatic LDA tends to underestimate optical gaps of dielectrics. This optical-gap problem is closely related to the well-known band-gap problem of the local density approximation in the static density functional theory. The optical gap is a crucial quantity to quantitatively investigate nonlinear electron dynamics induced by intense laser pulses since it is directly related to the order of perturbation that permits electronic excitation in the multi-photon picture. Furthermore, the optical gap also explicitly comes in the Keldysh parameter [121] which defines the transition of two different excitation regimes for strong laser fields; multi-photon and tunneling regimes. Therefore, the underestimation of the optical gap largely affects the description of nonlinear electronic excitations in both perturbative and non-perturbative nonlinear regimes. In order to improve the description of optical gaps of dielectrics, we have employed a meta generalized gradient approximation (meta-GGA) potential proposed by Tran and Blaha [103]. The meta-GGA potential improves the description of optical gaps of dielectrics as well as static band gaps. We have found that it is indispensable to adopt the predictor-corrector procedure for a stable time evolution when the meta-GGA potential is employed in the real-time TDDFT simulations. The meta-GGA potential is directly defined without referring to functional. Functional from which the meta-GGA potential is derived has not been known yet. Therefore, it is impossible to evaluate total energy of a system and its excitation energy by using an explicit expression of the exchange-correlation energy. In order to evaluate the electronic excitation energy employing the meta-GGA potential, we have developed a method to calculate it based on work done by external electric fields applied to an electronic system without referring to the energy functional. Thanks to the improvement of accuracy of the real-time TDDFT simulation achieved by the meta-GGA, quantitative investigations for laser-sold interactions in the strongly nonlinear regime has become possible. We have employed the meta-GGA in the real-time TDDFT simulations to investigate the following three topics.

Firstly, we have applied the real-time TDDFT simulation to investigate the optical properties of highly laser-excited dielectrics (Chapter 5). Modulation of optical properties induced by intense laser pulses is an important subject of the laser science and has been extensively studied in recent experiments [53, 101, 102]. High-intensity laser pulses produce electron-hole pairs in dielectrics, causing modulation of optical properties. Therefore, by analyzing the modulation, one may access the

information of the electron dynamics induced by the laser pulses in dielectrics. Indeed, the population dynamics of laser-excited electron-hole pairs has been investigated in experiments [170, 177–179] even in the time resolution of less than a femtosecond [53, 56, 133]. However, the existing theory describing these effects is largely phenomenological. Optical properties of laser-excited dielectrics are often modeled by the Drude model [134–137]. We have calculated the optical properties of highly laser-excited dielectrics based on the first-principles theory, the TDDFT. Immediately after intense laser irradiation, only electrons are excited while atoms locate at their positions in the ground state because of their slow motion. We call it the electronic nonequilibrium phase. After several tens of femtosecond, electrons are thermalized and become hot-carriers, while lattice stays in much lower temperature. We call this phase the electronic thermal-equilibrium phase. Furthermore, after several tens of picosecond, the system would become a complete equilibrium phase where electrons and lattice are described by the same temperature. This complete equilibrium phase is beyond the scope of this work. To investigate the electronic nonequilibrium phase, we have developed the *numerical pump-probe experiments* in which the experimental pump-probe technique is mimicked by the single-cell TDDFT simulation. To investigate the electron thermal-equilibrium phase, we have employed a linear response calculation for the finite electron-temperature system described with the Fermi-Dirac function for electronic occupation factors. We have applied the two methods to calculate dielectric functions of laser-excited silicon in both electronic nonequilibrium and thermal-equilibrium phases. We have found that the real parts of the dielectric functions in the both phases can be well described by the simple Drude model, indicating that the laser-excited dielectrics show the metallic behavior in the both phases. By the Drude analysis for the real part, we have found that the effective mass of electron-hole pairs depends on conditions of excitation, reflecting the different distribution of electron-hole pairs in the $k$-space. We have also found that the imaginary part of the dielectric functions shows complex behavior. The imaginary part in the nonequilibrium phase shows negative components at several frequencies, reflecting the nonequilibrium distribution of excited electrons, and cannot be described by the Drude model. On the other hand, the imaginary part in the electronic thermal-equilibrium phase does not show the negative component and can be well described by the Drude-like model. For the thermal-equilibrium phase, we have extracted the Drude damping time of hot-carriers and found that it depends on the electron temperature. The damping time can be short (about 1 fs), which is shorter than the timescale of electron-electron and electron-phonon collisions (several tens of fs to several ps). We consider that the short damping time could be caused by elastic scattering from ions.

Secondly, we have applied the real-time TDDFT simulation to investigate the nonlinear polarization and the energy transfer from laser pulses to dielectrics in the time domain (Chapter 6). Intense laser pulses may induce an irreversible structural modification in materials if the intensity of the laser pulses exceeds a critical threshold. The threshold is called damage threshold. If the intensity is close to but slightly below the damage threshold, the laser pulse may induce extremely nonlinear phenomena without any permanent damage. Such reversible nonlinear phenomena have been attracting much interest as a possible mechanism that is useful for future optical devices since the phenomena can be repeatedly used without any damage. In order to investigate such ultrafast nonlinear phenomena in the reversible regime, we have simulated fs-laser irradiation on a thin $SiO_2$ ($\alpha$-quartz) film ($10\mu m$ thickness) with the multi-scale TDDFT simulation for several laser intensities and calculated transmitted laser pulses from the thin film. As a result of the simulations, self-phase modulation and self-steepening have been found in the transmitted pulses, reflecting the Kerr and higher order nonlinear effects. Thanks to the recent development of the laser technologies, the experimental observation of the transmitted laser pulses in the time domain has become possible with the *attosecond*

*streaking* technique [180]. We have compared the simulated results with recent experimental data and found nice agreement between them even in the strongly nonlinear regime. The agreement indicates that the present TDDFT simulation correctly captures the nonlinear nature of the laser-medium interactions. Then we have investigated the induced nonlinear polarization in the time domain based on the microscopic electron dynamics. Referring the maximum amplitude of the evaluated nonlinear polarization, we estimated that the maximum modification of the refractive index below the damage threshold is about 1% in the present condition. We have found the attosecond time-delay between the applied electric field and the induced nonlinear polarization, reflecting energy transfer from laser fields to electrons in the medium. The time-delay increases as the laser intensity increases and achieves 100 as below the damage threshold. We have also evaluated the energy transfer from laser pulses to the medium in the time domain. Under some assumptions, it is possible to extract the nonlinear polarization and the energy transfer from the experimental results. We have compared the simulated energy transfer with the experimental one in the time domain and have found that they show nice agreement with each other. Thus, the assumptions of the experimental extractions have been validated based on the first-principles calculation. We have further theoretically investigated the microscopic mechanism of the nonlinear polarization in $\alpha$-quartz and found that the nonlinear polarization mainly comes from the electronic motion around oxygen atoms.

Thirdly, we have applied the real-time TDDFT simulation to investigate the initial stage of the non-thermal laser processing (Chapter 7). The non-thermal laser processing has been attracting much interest as a candidate of novel processing technique. In the initial stage of the non-thermal laser processing, energy transfer from femtosecond laser pulses to electrons in solids takes place. Since energy transfer from the excited electron to the lattice occurs in a picosecond time-scale, the femtosecond laser pulses provide a non-equilibrium phase where the electron temperature is much higher than the lattice temperature. The non-thermal laser processing phenomena take place through the non-equilibrium phase. So far, most theoretical investigations have relied on phenomenological models with empirical parameters, especially for the initial energy transfer from laser pulses to electrons in dielectrics. We have applied the first-principles calculation to investigate the initial energy transfer and investigated the microscopic mechanism of the non-thermal laser processing. First, we have simulated the fs-laser irradiation on the $SiO_2$ surface with the multi-scale TDDFT simulation and evaluated the spatial distribution of transferred energy from the laser pulses to the solid. We have employed laser pulses whose mean frequency is about $1.55/\hbar$ eV. Since the optical band gap of $\alpha$-quartz is about 9 eV, there is no energy transfer for the weak laser irradiation. Once the intensity of the laser pulses becomes sufficiently strong, the energy transfer can take place through the nonlinear light-matter interactions such as the multi-photon and tunneling excitation processes. We have found that almost all transferred energy are deposited near the surface (less than 100 nm in depth) for the strong laser irradiation due to the strong absorption and reflection for the high fields. We have estimated the damage and ablation thresholds and the ablation depth, by comparing the transferred energy distribution with melting and cohesive energies of $\alpha$-quartz. The estimated damage threshold shows the reasonable agreement with the experimental results. Also, the ablation depth fairly reproduces the experimental one. However, the estimated ablation threshold is higher than the experimental results, suggesting a nonthermal mechanism for the surface ablation. Furthermore, we have estimated the spatial profile of ablated craters. While the estimated crater profile created by the relatively weak laser pulse well reproduces the experimental one, the crater created by the relatively intense pulse fails to reproduce experiment. This indicates that the atomic dynamics after the energy transfer from light to medium plays a significant role to produce the complicated structure of ablated craters for intense laser irradiation.

So far, we have demonstrated that the real-time TDDFT simulation is a powerful tool to investigate the laser-solid interactions even in the strongly nonlinear conditions. The simulations have reproduced several experimental results even in a quantitative level and provided microscopic insight to understand the mechanism of the phenomena. The real-time TDDFT simulation would be applicable various phenomena in addition to three topics in this thesis. Further applications of the real-time TDDFT simulation to such important/interesting phenomena/systems are desired. However, it is also true that the present real-time TDDFT simulation lacks a number of effects and is not applicable several problems so far. For example, the present treatment of the real-time TDDFT simulation is not applicable to investigate relaxation dynamics after laser irradiation due to lack of electron-electron and electron-phonon scattering effects. The inclusion of such effects would be important not only to extend this thesis study but also to proceed whole light science. We describe a few perspectives below for further studies of the interactions of high-intensity ultrashort laser pulses with dielectrics in the near and/or distant future.

The optical property of laser-excited dielectrics *after* laser irradiation has been investigated in this thesis. On the other hand, transient optical property of dielectrics *during* laser irradiation is also important subject of optical science and has been intensively studied [53]. The real-time TDDFT simulation has potential ability to investigate such transient optical properties during the laser irradiation as well as after the pulses end with the numerical pump-probe experiments. A strong point of the first-principles calculation is possibility to access microscopic mechanism of the phenomena based on microscopic quantities such as time-dependent electron orbitals $\psi_n(\boldsymbol{r}, t)$, electron density $n(\boldsymbol{r}, t)$ and current density $\boldsymbol{j}(\boldsymbol{r}, t)$. We hope that the microscopic mechanism of transient modification of optical properties during the laser irradiation will be revealed by the real-time TDDFT calculation.

Recently, the experimental observation of the high-order harmonic generation (HHG) from solids has reported by several groups [28–30], and the theoretical investigation of the mechanism of HHG has been extensively studied based on simple/phenomenological models. However, the microscopic mechanism is still under discussion at present [31–34]. Since the HHG is strongly nonlinear phenomena in the nonperturbative regime, first-principles calculations based on perturbative expansions in the frequency domain do not work for the HHG. The real-time TDDFT simulation is a good candidate to investigate the microscopic mechanism since it is applicable even to the non-perturbative nonlinear dynamics and contains full quantum nature of electrons such as band structure and intra/inter-band transitions. We hope that the real-time TDDFT simulation provide the proper HHG spectra and clear insight to understand the microscopic mechanism of the HHG from solids.

One of the most significant and fundamental difficulties in the present real-time TDDFT simulation is the lack of damping effects. The present simulation, which relies on the adiabatic meta-GGA/LDA potential, does not correctly describe electron-electron collisions due to the lack of correlation effects in the exchange-correlation potentials. Furthermore, electron-phonon collisions are not described correctly, too, since atoms are simply fixed at their positions in the ground state. Therefore, once electrons are excited in the present simulation, they stay the excited states for a long time without damping, equilibration, and thermalization. However, if electrons are excited in a realistic system, the system reaches the electronic thermal-equilibrium phase, where electrons are thermalized and become hot-carriers but lattice stays in much lower temperature, in a hundred femtosecond time scale due to electron-electron and electron-phonon scattering. Eventually, the system approaches to the complete equilibrium phase due to the interaction between hot-carriers and phonons. The relaxation dynamics of laser-excited electrons in solids is one of the most important subject of optical science and has been extensively studied for a long period [170, 177–179]. However, theoretical investigations of the

relaxation from the first-principles level are still in a stage of development [181]. The correct inclusion of electron-electron and electron-phonon collisions in the real-time TDDFT simulation would be highly desired to study the relaxation dynamics.

Related to the above damping problems, the present TDDFT simulation is valid only before the times when electron-electron collisions have played significant role in the nonequilibrium dynamics of laser-excited systems (several tens of femtosecond). Moreover, the real-time TDDFT simulation is also pragmatically difficult to apply the long time evolution owing to its large computational costs. Therefore, a post-TDDFT simulation in which subsequent dynamics after laser irradiation is treated by another theoretical framework is desired. In this thesis, the damage/ablation thresholds and the ablation depth have been estimated by the simple comparison of the transferred energy distribution based on the TDDFT and melting/cohesive energies of the material. We did not explicitly investigate any microscopic dynamics after the laser irradiation. In order to investigate the subsequent dynamics of the non-thermal laser processing phenomena after laser irradiation, it is necessary to explicitly treat atomic motion. Indeed, the molecular dynamics (MD) simulations have been applied to investigate the ablation dynamics [173]. However, in these simulations, the energy transfer from laser pulses to materials is treated phenomenologically. If the real-time TDDFT simulation, which describes the energy transfer from laser pulses to samples, and the MD simulation, which provides the subsequent molecular dynamics after the laser irradiation, are correctly combined, a fully microscopic simulation of laser ablation phenomena without any phenomenological assumptions will be established. The fully microscopic simulation could provide microscopic insights of the phenomena and clarify the mechanism.

# Appendix A

# Hilbert transformation

In order to analyze the time profile of an oscillating signal, it is convenient to decompose the signal into the envelope function and the carrier wave. The Hilbert transformation is one of the signal processing methods and may provide the decomposition. In this chapter, we briefly explain the Hilbert transformation and illustrate the decomposition by taking a simple Gaussian pulse as an example.

## A.1  Fourier transformation and Hilbert transformation

Here, we consider a real function $f(t)$ in the time domain. The Fourier transformation of the real function is given by

$$\tilde{f}(\omega) = \int_{-\infty}^{\infty} dt f(t) e^{i\omega t}, \tag{A.1}$$

and the inverse Fourier transformation is given by

$$f(t) = \frac{1}{2\pi} \int_{-\infty}^{\infty} d\omega \tilde{f}(\omega) e^{-i\omega t}. \tag{A.2}$$

Since the function $f(t)$ is real, there holds,

$$\tilde{f}(\omega) = \tilde{f}^*(-\omega). \tag{A.3}$$

Employing the Fourier transformation $\tilde{f}(\omega)$, the Hilbert transformation of the real function $f(t)$ is given by

$$\bar{f}(t) = \frac{1}{\pi} \int_{0}^{\infty} d\omega \tilde{f}(\omega). \tag{A.4}$$

Although the original function $f(t)$ is real, the Hilbert transformation of it $\bar{f}(t)$ is generally complex. Furthermore, the real part of the Hilbert transformation coincides with the original function;

$$f(t) = \frac{1}{2\pi} \int_{-\infty}^{\infty} d\omega \tilde{f}(\omega) e^{-i\omega t} = \frac{1}{2\pi} \int_{0}^{\infty} d\omega \tilde{f}(\omega) e^{-i\omega t} + c.c. = \Re \left[ \frac{1}{\pi} \int_{0}^{\infty} d\omega \tilde{f}(\omega) e^{-i\omega t} \right] = \Re[\bar{f}(t)], \tag{A.5}$$

where we employed Eqs. (A.2), (A.3), and (A.4).

113

Here, we consider the amplitude and the phase of the Hilbert transformation $\bar{f}(t)$ as

$$\bar{f}(t) = A(t)e^{-iS(t)}, \tag{A.6}$$

where both the amplitude $A(t)$ and the phase $S(t)$ are real. The amplitude $A(t)$ is given by $A(t) = |\bar{f}(t)|$, and the phase $S(t)$ is given by $S(t) = -\Im\left[ln\bar{f}(t)\right]$. The amplitude $A(t)$ may give the envelope function of the signal, and the phase function $S(t)$ may give the phase of the carrier wave of the signal. We will illustrate the extraction of the envelope function and the carrier phase based on the Hilbert transformation in the next section.

## A.2    Hilbert transformation of a Gaussian pulse

Here, we illustrate the Hilbert transformation, taking a Gaussian pulse as an example. We consider the following simple Gaussian pulse,

$$f(t) = e^{-\frac{t^2}{2\sigma^2}} \cos(\omega_0 t + \phi), \tag{A.7}$$

where $\sigma$ is the width of the Gaussian envelope function, $\omega_0$ is the frequency of the carrier wave, and $\phi$ is the carrier-envelope phase. The width and the frequency are defined as positive values; $\sigma = |\sigma|$ and $\omega_0 = |\omega_0|$. For later convenience, we define the envelope function as $ENV(t) = e^{-\frac{t^2}{2\sigma^2}}$ and the carrier phase as $\Phi(t) = \omega_0 t + \phi$. The signal in the time domain $f(t)$ is simply written by $f(t) = ENV(t) \times \cos\{\Phi(t)\}$. We then extract the envelope function $ENV(t)$ and the carrier phase $\Phi(t)$ based on the Hilbert transformation.

First, we calculate the Fourier transformation of $f(t)$;

$$\tilde{f}(\omega) = \int_{-\infty}^{\infty} dt f(t)e^{i\omega t} = \frac{\sqrt{2\sigma^2\pi}}{2}\left[e^{-\frac{\sigma^2}{2}(\omega+\omega_0)^2}e^{i\phi} + e^{-\frac{\sigma^2}{2}(\omega-\omega_0)^2}e^{i\phi}\right]. \tag{A.8}$$

The Fourier transformation of $f(t)$ has two peaks at $\omega = \pm\omega_0$ in the frequency domain. Then, we calculate the Hilbert transformation;

$$\bar{f}(t) = \int_{0}^{\infty} dt \tilde{f}(\omega)e^{-i\omega t} = \int_{0}^{\infty} dt \frac{\sqrt{2\sigma^2\pi}}{2}\left[e^{-\frac{\sigma^2}{2}(\omega+\omega_0)^2}e^{i\phi} + e^{-\frac{\sigma^2}{2}(\omega-\omega_0)^2}e^{i\phi}\right]e^{-i\omega t}. \tag{A.9}$$

Assuming $\sigma\omega_0 \gg 1$, the Hilbert transformation may be evaluated as

$$\bar{f}(t) \approx \int_{-\infty}^{\infty} dt \frac{\sqrt{2\sigma^2\pi}}{2}e^{i\phi} + e^{-\frac{\sigma^2}{2}(\omega-\omega_0)^2}e^{i\phi}e^{-i\omega t} = e^{-\frac{t^2}{2\sigma^2}}e^{-i(\omega_0 t+\phi)}. \tag{A.10}$$

The assumption of $\sigma\omega_0 > 1$ guarantees that there is only one well-isolated peak of the Fourier transformation in the positive frequency region.

It is obvious that the real part of the Hilbert transformation $\bar{f}(t)$ coincides with the original signal $f(t)$;

$$\Re[\bar{f}(t)] = e^{-\frac{t^2}{2\sigma^2}} \cos(\omega_0 t + \phi) = f(t). \tag{A.11}$$

Furthermore, the amplitude $A(t)$ and the phase $S(t)$ of the Hilbert transformation coincide with the envelope function $ENV(t)$ and the carrier phase $\Phi(t)$;

$$A(t) = |\bar{f}(t)| = e^{-\frac{t^2}{2\sigma^2}} = ENV(t), \tag{A.12}$$

$$S(t) = -\Im \left[ \ln \bar{f}(t) \right] = \omega_0 t + \phi = \Phi(t). \tag{A.13}$$

These results clearly indicate that the Hilbert transformation has potential to decompose an oscillating signal into the envelope and the phase functions.

In this section, we illustrated the extraction of the envelope and the phase functions of the simple Gaussian pulse based on the Hilbert transformation. Fortunately, we easily extracted the envelope and the phase functions of the Gaussian pulse since the analytic form of the pulse was given. However, in general, it is not obvious how to extract the envelope and the phase functions. The Hilbert transformation would be an useful tool to extract the envelope and phase functions of such complicated oscillating signals.

# Appendix B

# Modification of refractive index

In this chapter, we simply describe the relation between the modification of the refractive index $\Delta n$ and the nonlinear polarization $P_{NL}$. The refractive index $n$ is defined as the square root of the dielectric function $\epsilon$ as usual; $n = \sqrt{\epsilon}$.

We first consider the apparent modification of the dielectric function due to the nonlinear polarization. The frequency dependent electric flux density $D(\omega)$ is defined by

$$D(\omega) = E(\omega) + 4\pi P(\omega), \tag{B.1}$$

where $E(\omega)$ is the electric field, and $P(\omega)$ is the polarization. If the field strength is sufficiently weak, the polarization in the above equation can be described by the linear response, $P(\omega) = \chi^{(1)}(\omega)E(\omega)$, and the equation becomes

$$D_L(\omega) = E_L(\omega) + 4\pi\chi^{(1)}(\omega)E_L(\omega) = \epsilon(\omega)E_L(\omega), \tag{B.2}$$

where $E_L(\omega)$ denotes the weak electric field, and $D_L(\omega)$ denotes the corresponding electric flux density. One may see that the dielectric function $\epsilon(\omega)$ is a quantity that connects the electric flux density and the electric field.

Decomposing the polarization $P(\omega)$ into the linear response part $P_L(\omega)$ and the nonlinear response part $P_{NL}(\omega)$, we may rewrite Eq. (B.1) as

$$
\begin{aligned}
D(\omega) &= E(\omega) + 4\pi P_L(\omega) + 4\pi P_{NL}(\omega) \\
&= E(\omega) + 4\pi\chi^{(1)}(\omega)E(\omega) + 4\pi P_{NL}(\omega) \\
&= \epsilon(\omega)E(\omega) + 4\pi P_{NL}(\omega) \\
&= \left[\epsilon(\omega) + 4\pi\frac{P_{NL}(\omega)}{E(\omega)}\right]E(\omega).
\end{aligned}
\tag{B.3}
$$

Based on Eq. (B.3), one may define the modification of the dielectric function due to the nonlinear polarization by

$$\Delta\epsilon(\omega) = 4\pi\frac{P_{NL}(\omega)}{E(\omega)}. \tag{B.4}$$

Furthermore, the modification of the refractive index can be defined by

$$\Delta n(\omega) = \frac{\Delta\epsilon(\omega)}{2n(\omega)} = 2\pi\frac{P_{NL}(\omega)}{n(\omega)E(\omega)}. \tag{B.5}$$

# Bibliography

[1] United Nations. "International Year of Light and Light-based Technologies, 2015". *General Assembly resolution 68/221*, (2014).

[2] E Fred Schubert. "Light-Emitting Diodes 2nd edition". (2006).

[3] S. Nakamura and M.R. Krames. "History of Gallium-Nitride-Based Light-Emitting Diodes for Illumination". *Proceedings of the IEEE*, **101**(10) 2211–2220, (2013).

[4] Serap Günes, Helmut Neugebauer, and Niyazi Serdar Sariciftci. "Conjugated Polymer-Based Organic Solar Cells". *Chemical Reviews*, **107**(4) 1324–1338, (2007).

[5] Anders Hagfeldt, Gerrit Boschloo, Licheng Sun, Lars Kloo, and Henrik Pettersson. "Dye-Sensitized Solar Cells". *Chemical Reviews*, **110**(11) 6595–6663, (2010).

[6] W. C. Röntgen. "Real-time observation of valence electron motion". *Nature*, **53** 274–276, (1896).

[7] S.-W. Bahk, P. Rousseau, T. A. Planchon, V. Chvykov, G. Kalintchenko, A. Maksimchuk, G. A. Mourou, and V. Yanovsky. "Generation and characterization of the highest laser intensities ($10^{22}$ W/cm$^2$)". *Opt. Lett.*, **29**(24) 2837–2839, (2004).

[8] V. Yanovsky, V. Chvykov, G. Kalinchenko, P. Rousseau, T. Planchon, T. Matsuoka, A. Maksimchuk, J. Nees, G. Cheriaux, G. Mourou, and K. Krushelnick. "Ultra-high intensity- 300-TW laser at 0.1 Hz repetition rate.". *Opt. Express*, **16**(3) 2109–2114, (2008).

[9] Tae Jun Yu, Seong Ku Lee, Jae Hee Sung, Jin Woo Yoon, Tae Moon Jeong, and Jongmin Lee. "Generation of high-contrast, 30 fs, 1.5 PW laser pulses from chirped-pulse amplification Ti:sapphire laser". *Opt. Express*, **20**(10) 10807–10815, (2012).

[10] P. A. Franken, A. E. Hill, C. W. Peters, and G. Weinreich. "Generation of Optical Harmonics". *Phys. Rev. Lett.*, **7** 118–119, (1961).

[11] Thomas Brabec and Ferenc Krausz. "Intense few-cycle laser fields: Frontiers of nonlinear optics". *Rev. Mod. Phys.*, **72** 545–591, (2000).

[12] Gerard A. Mourou, Toshiki Tajima, and Sergei V. Bulanov. "Optics in the relativistic regime". *Rev. Mod. Phys.*, **78** 309–371, (2006).

[13] Robert W Boyd. "Nonlinear optics". (2003).

[14] Paul N. Butcher and David Cotter. "The elements of nonlinear optics". **9**, (1991).

[15] G. A. Mourou, N. J. Fisch, V. M. Malkin, Z. Toroker, E. A. Khazanov, A. M. Sergeev, T. Tajima, and B. Le Garrec. "Exawatt-Zettawatt pulse generation and applications". *Optics Communications*, **285**(5) 720 – 724, (2012).

[16] A. McPherson, G. Gibson, H. Jara, U. Johann, T. S. Luk, I. A. McIntyre, K. Boyer, and C. K. Rhodes. "Studies of multiphoton production of vacuum-ultraviolet radiation in the rare gases". *J. Opt. Soc. Am. B*, **4**(4) 595–601, (1987).

[17] X. F. Li, A. L'Huillier, M. Ferray, L. A. Lompré, and G. Mainfray. "Multiple-harmonic generation in rare gases at high laser intensity". *Phys. Rev. A*, **39** 5751–5761, (1989).

[18] Nobuhiko Sarukura, Kiyoshi Hata, Takashi Adachi, Ryoichi Nodomi, Masayoshi Watanabe, and Shuntaro Watanabe. "Coherent soft-x-ray generation by the harmonics of an ultrahigh-power KrF laser". *Phys. Rev. A*, **43** 1669–1672, (1991).

[19] J. K. Crane, R. W. Falcone, M. D. Perry, and S. Herman. "High-field harmonic generation in helium". *Opt. Lett.*, **17**(18) 1256–1258, (1992).

[20] J. J. Macklin, J. D. Kmetec, and C. L. Gordon. "High-order harmonic generation using intense femtosecond pulses". *Phys. Rev. Lett.*, **70** 766–769, (1993).

[21] Anne L'Huillier and Ph. Balcou. "High-order harmonic generation in rare gases with a 1-ps 1053-nm laser". *Phys. Rev. Lett.*, **70** 774–777, (1993).

[22] Jeffrey L. Krause, Kenneth J. Schafer, and Kenneth C. Kulander. "High-order harmonic generation from atoms and ions in the high intensity regime". *Phys. Rev. Lett.*, **68** 3535–3538, (1992).

[23] K. J. Schafer, Baorui Yang, L. F. DiMauro, and K. C. Kulander. "Above threshold ionization beyond the high harmonic cutoff". *Phys. Rev. Lett.*, **70** 1599–1602, (1993).

[24] P. B. Corkum. "Plasma perspective on strong field multiphoton ionization". *Phys. Rev. Lett.*, **71** 1994–1997, (1993).

[25] M. Lewenstein, Ph. Balcou, M. Yu. Ivanov, Anne L'Huillier, and P. B. Corkum. "Theory of high-harmonic generation by low-frequency laser fields". *Phys. Rev. A*, **49** 2117–2132, (1994).

[26] P. M. Paul, E. S. Toma, P. Breger, G. Mullot, F. Aug, Ph. Balcou, H. G. Muller, and P. Agostini. "Observation of a Train of Attosecond Pulses from High Harmonic Generation". *Science*, **292**(5522) 1689–1692, (2001).

[27] Ferenc Krausz and Misha Ivanov. "Attosecond physics". *Rev. Mod. Phys.*, **81** 163–234, (2009).

[28] Shambhu Ghimire, Anthony D DiChiara, Emily Sistrunk, Pierre Agostini, Louis F DiMauro, and David A Reis. "Observation of high-order harmonic generation in a bulk crystal". *Nature physics*, **7**(2) 138–141, (2011).

[29] Olaf Schubert, Matthias Hohenleutner, Fabian Langer, Benedikt Urbanek, C Lange, U Huttner, D Golde, T Meier, M Kira, SW Koch, et al. "Sub-cycle control of terahertz high-harmonic generation by dynamical Bloch oscillations". *Nature Photonics*, **8**(2) 119–123, (2014).

[30] TT Luu, M Garg, S Yu Kruchinin, A Moulet, M Th Hassan, and E Goulielmakis. "Extreme ultraviolet high-harmonic spectroscopy of solids". *Nature*, **521**(7553) 498–502, (2015).

[31] G. Vampa, C. R. McDonald, G. Orlando, D. D. Klug, P. B. Corkum, and T. Brabec. "Theoretical Analysis of High-Harmonic Generation in Solids". *Phys. Rev. Lett.*, **113** 073901, (2014).

[32] Peter G. Hawkins, Misha Yu. Ivanov, and Vladislav S. Yakovlev. "Effect of multiple conduction bands on high-harmonic emission from dielectrics". *Phys. Rev. A*, **91** 013405, (2015).

[33] Mengxi Wu, Shambhu Ghimire, David A. Reis, Kenneth J. Schafer, and Mette B. Gaarde. "High-harmonic generation from Bloch electrons in solids". *Phys. Rev. A*, **91** 043839, (2015).

[34] C. R. McDonald, G. Vampa, P. B. Corkum, and T. Brabec. "Interband Bloch oscillation mechanism for high-harmonic generation in semiconductor crystals". *Phys. Rev. A*, **92** 033845, (2015).

[35] M. D. Perry, B. C. Stuart, P. S. Banks, M. D. Feit, V. Yanovsky, and A. M. Rubenchik. "Ultrashort-pulse laser machining of dielectric materials". *J. Appl. Phys*, **85** 6803, (1999).

[36] Rafael R. Gattass and Eric Mazur. "Femtosecond laser micromachining in transparent materials". *Nature Photonics*, **2** 219–225, (2008).

[37] E. G. Gamaly. "The physics of ultra-short laser interaction with solids at non-relativistic intensities". *Physics Reports*, **508**(4-5) 91 – 243, (2011).

[38] D. C. Emmony, R. P. Howson, and L. J. Willis. "Laser mirror damage in germanium at 10.6 m". *Applied Physics Letters*, **23**(11) 598–600, (1973).

[39] D Ashkenasi, A Rosenfeld, H Varel, M Whmer, and E.E.B Campbell. "Laser processing of sapphire with picosecond and sub-picosecond pulses". *Applied Surface Science*, **120**(1-2) 65 – 80, (1997).

[40] Shuji Sakabe, Masaki Hashida, Shigeki Tokita, Shin Namba, and Kiminori Okamuro. "Mechanism for self-formation of periodic grating structures on a metal surface by a femtosecond laser pulse". *Phys. Rev. B*, **79** 033409, (2009).

[41] P Balling and J Schou. "Femtosecond-laser ablation dynamics of dielectrics: basics and applications for thin films". *Reports on Progress in Physics*, **76**(3) 036502, (2013).

[42] K. Miura, Jianrong Qiu, S. Fujiwara, S. Sakaguchi, and K. Hirao. "Three-dimensional optical memory with rewriteable and ultrahigh density using the valence-state change of samarium ions". *Applied Physics Letters*, **80**(13) 2263–2265, (2002).

[43] Yasuhiko Shimotsuma, Masaaki Sakakura, Kiyotaka Miura, Jiarong Qiu, Peter G. Kazansky, Koji Fujita, and Andkazuyuki Hirao. "Application of Femtosecond-Laser Induced Nanostructures in Optical Memory". *Journal of Nanoscience and Nanotechnology*, **7**(1) 94–104, (2007-01-01T00:00:00).

[44] P. Krehl and S. Engemann. "August Toepler-the first who visualized shock waves". *Shock Waves*, **5**(1-2) 1–18, (1995).

[45] Ahmed H. Zewail. "Laser Femtochemistry". *Science*, **242**(4886) 1645–1653, (1988).

[46] Todd S. Rose, Mark J. Rosker, and Ahmed H. Zewail. "Femtosecond real-time observation of wave packet oscillations (resonance) in dissociation reactions". *The Journal of Chemical Physics*, **88**(10) 6672–6673, (1988).

[47] Ahmed H. Zewail. "Femtochemistry: ultrafast dynamics of the chemical bond". **1**, (1994).

[48] Ahmed H. Zewail. "Femtochemistry: Atomic-Scale Dynamics of the Chemical Bond". *The Journal of Physical Chemistry A*, **104**(24) 5660–5694, (2000).

[49] Kun Zhao, Qi Zhang, Michael Chini, Yi Wu, Xiaowei Wang, and Zenghu Chang. "Tailoring a 67 attosecond pulse through advantageous phase-mismatch". *Opt. Lett.*, **37**(18) 3891–3893, (2012).

[50] P. B. Corkum and Ferenc Krausz. "Attosecond science". *Nature Physics*, **3**(6) 381–387, (2007).

[51] Renate Pazourek, Stefan Nagele, and Joachim Burgdörfer. "Attosecond chronoscopy of photoemission". *Rev. Mod. Phys.*, **87** 765–802, (2015).

[52] Eleftherios Goulielmakis, Zhi-Heng Loh, Adrian Wirth, Robin Santra, Nina Rohringer, Vladislav S. Yakovlev, Sergey Zherebtsov, Thomas Pfeifer, Abdallah M. Azzeer, Matthias F. Kling, Stephen R. Leone, and Ferenc Krausz. "Real-time observation of valence electron motion". *Nature*, **466** 466–743, (2010).

[53] Martin Schultze, Elisabeth M. Bothschafter, Annkatrin Sommer, Simon Holzner, Wolfgang Schweinberger, Markus Fiess, Michael Hofstetter, Reinhard Kienberger, Vadym Apalkov, Vladislav S. Yakovlev, Mark I. Stockman, and Ferenc Krausz. "Controlling dielectrics with the electric field of light". *Nature*, **493** 75–78, (2013).

[54] A. Couairon and A. Mysyrowicz. "Femtosecond filamentation in transparent media". *Physics Reports*, **441**(2-4) 47–189, (2007).

[55] M. Lebugle, N. Sanner, O. Utéza, and M. Sentis. "Guidelines for efficient direct ablation of dielectrics with single femtosecond pulses". *Applied Physics A*, **114**(1) 129–142, (2014).

[56] Agustin Schiffrin, Tim Paasch-Colberg, Nicholas Karpowicz, Vadym Apalkov, Daniel Gerster, Sascha Mühlbrandt, Michael Korbman, Joachim Reichert, Martin Schultze, Simon Holzner, et al. "Optical-field-induced current in dielectrics". *Nature*, **493**(7430) 70–74, (2013).

[57] Martin Schultze, Krupa Ramasesha, C. D. Pemmaraju, S. A. Sato, D. Whitmore, A. Gandman, James S. Prell, L. J. Borja, D. Prendergast, K. Yabana, Daniel M. Neumark, and Stephen R. Leone. "Attosecond band-gap dynamics in silicon". *Science*, **346**(6215) 1348–1352, (2014).

[58] Jiří Čížek. "On the correlation problem in atomic and molecular systems. Calculation of wavefunction components in Ursell-type expansion using quantum-field theoretical methods". *The Journal of Chemical Physics*, **45**(11) 4256–4266, (1966).

[59] Lars Hedin. "New Method for Calculating the One-Particle Green's Function with Application to the Electron-Gas Problem". *Phys. Rev.*, **139** A796–A823, (1965).

[60] Mark S. Hybertsen and Steven G. Louie. "First-Principles Theory of Quasiparticles: Calculation of Band Gaps in Semiconductors and Insulators". *Phys. Rev. Lett.*, **55** 1418–1421, (1985).

[61] J. Caillat, J. Zanghellini, M. Kitzler, O. Koch, W. Kreuzer, and A. Scrinzi. "Correlated multielectron systems in strong laser fields: A multiconfiguration time-dependent Hartree-Fock approach". *Phys. Rev. A*, **71** 012712, (2005).

[62] Tsuyoshi Kato and Hirohiko Kono. "Time-dependent multiconfiguration theory for electronic dynamics of molecules in an intense laser field". *Chemical Physics Letters*, **392**(4 篜 6) 533 – 540, (2004).

[63] Takeshi Sato and Kenichi L. Ishikawa. "Time-dependent complete-active-space self-consistent-field method for multielectron dynamics in intense laser fields". *Phys. Rev. A*, **88** 023402, (2013).

[64] Michael Rohlfing and Steven G. Louie. "Excitonic Effects and the Optical Absorption Spectrum of Hydrogenated Si Clusters". *Phys. Rev. Lett.*, **80** 3320–3323, (1998).

[65] Michael Rohlfing and Steven G. Louie. "Electron-hole excitations and optical spectra from first principles". *Phys. Rev. B*, **62** 4927–4944, (2000).

[66] P. Hohenberg and W. Kohn. "Inhomogeneous Electron Gas". *Phys. Rev.*, **136** B864–B871, (1964).

[67] W. Kohn and L. J. Sham. "Self-Consistent Equations Including Exchange and Correlation Effects". *Phys. Rev.*, **140** A1133–A1138, (1965).

[68] Jeremy Taylor, Hong Guo, and Jian Wang. "*Ab initio* modeling of quantum transport properties of molecular electronic devices". *Phys. Rev. B*, **63** 245407, (2001).

[69] Shinya Kyogoku, Jun-Ichi Iwata, and Atsushi Oshiyama. "Relation between nanomorphology and energy bands of Si nanowires". *Phys. Rev. B*, **87** 165418, (2013).

[70] Yu-ichiro Matsushita, Shinnosuke Furuya, and Atsushi Oshiyama. "Floating Electron States in Covalent Semiconductors". *Phys. Rev. Lett.*, **108** 246404, (2012).

[71] Paolo Carloni, Ursula Rothlisberger, , and Michele Parrinello. "The Role and Perspective of Ab Initio Molecular Dynamics in the Study of Biological Systems". *Accounts of Chemical Research*, **35**(6) 455–464, (2002).

[72] Stefan Grimme, Jens Antony, Tobias Schwabe, and Christian Muck-Lichtenfeld. "Density functional theory with dispersion corrections for supramolecular structures, aggregates, and complexes of (bio)organic molecules". *Org. Biomol. Chem.*, **5** 741–758, (2007).

[73] Mohammad K. Nazeeruddin, Filippo De Angelis, Simona Fantacci, Annabella Selloni, Guido Viscardi, Paul Liska, Seigo Ito, Bessho Takeru, and Michael Grätzel. "Combined Experimental and DFT-TDDFT Computational Study of Photoelectrochemical Cell Ruthenium Sensitizers". *Journal of the American Chemical Society*, **127**(48) 16835–16847, (2005).

[74] Keisuke Ushirogata, Keitaro Sodeyama, Yukihiro Okuno, and Yoshitaka Tateyama. "Additive Effect on Reductive Decomposition and Binding of Carbonate-Based Solvent toward Solid Electrolyte Interphase Formation in Lithium-Ion Battery". *Journal of the American Chemical Society*, **135**(32) 11967–11974, (2013).

[75] Yuki Yamada, Keizo Furukawa, Keitaro Sodeyama, Keisuke Kikuchi, Makoto Yaegashi, Yoshitaka Tateyama, and Atsuo Yamada. "Unusual Stability of Acetonitrile-Based Superconcentrated Electrolytes for Fast-Charging Lithium-Ion Batteries". *Journal of the American Chemical Society*, **136**(13) 5039–5046, (2014).

[76] Erich Runge and E. K. U. Gross. "Density-Functional Theory for Time-Dependent Systems". *Phys. Rev. Lett.*, **52** 997–1000, (1984).

[77] S. Sharma, J. K. Dewhurst, A. Sanna, and E. K. U. Gross. "Bootstrap Approximation for the Exchange-Correlation Kernel of Time-Dependent Density-Functional Theory". *Phys. Rev. Lett.*, **107** 186401, (2011).

[78] Lucia Reining, Valerio Olevano, Angel Rubio, and Giovanni Onida. "Excitonic Effects in Solids Described by Time-Dependent Density-Functional Theory". *Phys. Rev. Lett.*, **88** 066404, (2002).

[79] Silvana Botti, Armel Fourreau, Fran çois Nguyen, Yves-Olivier Renault, Francesco Sottile, and Lucia Reining. "Energy dependence of the exchange-correlation kernel of time-dependent density functional theory: A simple model for solids". *Phys. Rev. B*, **72** 125203, (2005).

[80] Joachim Paier, Martijn Marsman, and Georg Kresse. "Dielectric properties and excitons for extended systems from hybrid functionals". *Phys. Rev. B*, **78** 121201, (2008).

[81] J. A. Berger. "Fully Parameter-Free Calculation of Optical Spectra for Insulators, Semiconductors, and Metals from a Simple Polarization Functional". *Phys. Rev. Lett.*, **115** 137402, (2015).

[82] Giovanni Onida, Lucia Reining, and Angel Rubio. "Electronic excitations: density-functional versus many-body Green's-function approaches". *Rev. Mod. Phys.*, **74** 601–659, (2002).

[83] Miguel AL Marques, Neepa T Maitra, Fernando MS Nogueira, Eberhard KU Gross, and Angel Rubio. "Fundamentals of time-dependent density functional theory". **837**, (2012).

[84] R. M. Sternheimer. "Electronic Polarizabilities of Ions from the Hartree-Fock Wave Functions". *Phys. Rev.*, **96** 951–968, (1954).

[85] Stefano Baroni, Paolo Giannozzi, and Andrea Testa. "Elastic Constants of Crystals from Linear-Response Theory". *Phys. Rev. Lett.*, **59** 2662–2665, (1987).

[86] Xavier Gonze. "Perturbation expansion of variational principles at arbitrary order". *Phys. Rev. A*, **52** 1086–1095, (1995).

[87] Xavier Andrade, Silvana Botti, Miguel A. L. Marques, and Angel Rubio. "Time-dependent density functional theory scheme for efficient calculations of dynamic (hyper)polarizabilities". *The Journal of Chemical Physics*, **126**(18) 184106, (2007).

[88] Mark E Casida. "Time-dependent density functional response theory for molecules". *Recent advances in density functional methods*, **1** 155, (1995).

[89] P. Bonche, S. Koonin, and J. W. Negele. "One-dimensional nuclear dynamics in the time-dependent Hartree-Fock approximation". *Phys. Rev. C*, **13** 1226–1258, (1976).

[90] H. Flocard, S. E. Koonin, and M. S. Weiss. "Three-dimensional time-dependent Hartree-Fock calculations: Application to $^{16}O + ^{16}O$ collisions". *Phys. Rev. C*, **17** 1682–1699, (1978).

[91] K. Yabana and G. F. Bertsch. "Time-dependent local-density approximation in real time". *Phys. Rev. B*, **54** 4484–4487, (1996).

[92] Sang-Kil Son and Shih-I Chu. "Multielectron effects on the orientation dependence and photoelectron angular distribution of multiphoton ionization of $CO_2$ in strong laser fields". *Phys. Rev. A*, **80** 011403, (2009).

[93] F. Calvayrac, P.-G. Reinhard, E. Suraud, and C.A. Ullrich. "Nonlinear electron dynamics in metal clusters". *Physics Reports*, **337**(6) 493 – 578, (2000).

[94] D. Bauer, F. Ceccherini, A. Macchi, and F. Cornolti. "$C_{60}$ in intense femtosecond laser pulses: Nonlinear dipole response and ionization". *Phys. Rev. A*, **64** 063203, (2001).

[95] Roi Baer, Daniel Neuhauser, Petra R. Ždánská, and Nimrod Moiseyev. "Ionization and high-order harmonic generation in aligned benzene by a short intense circularly polarized laser pulse". *Phys. Rev. A*, **68** 043406, (2003).

[96] G. F. Bertsch, J.-I. Iwata, Angel Rubio, and K. Yabana. "Real-space, real-time method for the dielectric function". *Phys. Rev. B*, **62** 7998–8002, (2000).

[97] T. Otobe, M. Yamagiwa, J.-I. Iwata, K. Yabana, T. Nakatsukasa, and G. F. Bertsch. "First-principles electron dynamics simulation for optical breakdown of dielectrics under an intense laser field". *Phys. Rev. B*, **77** 165104, (2008).

[98] Y. Shinohara, K. Yabana, Y. Kawashita, J.-I. Iwata, T. Otobe, and G. F. Bertsch. "Coherent phonon generation in time-dependent density functional theory". *Phys. Rev. B*, **82** 155110, (2010).

[99] Y. Shinohara, S. A. Sato, K. Yabana, J.-I. Iwata, T. Otobe, and G. F. Bertsch. "Nonadiabatic generation of coherent phonons". *The Journal of Chemical Physics*, **137**(22) 22A527, (2012).

[100] K. Yabana, T. Sugiyama, Y. Shinohara, T. Otobe, and G. F. Bertsch. "Time-dependent density functional theory for strong electromagnetic fields in crystalline solids". *Phys. Rev. B*, **85** 045134, (2012).

[101] K. Sokolowski-Tinten and D. von der Linde. "Generation of dense electron-hole plasmas in silicon". *Phys. Rev. B*, **61** 2643–2650, (2000).

[102] V. V. Temnov, K. Sokolowski-Tinten, P. Zhou, A. El-Khamhawy, and D. von der Linde. "Multiphoton Ionization in Dielectrics: Comparison of Circular and Linear Polarization". *Phys. Rev. Lett.*, **97** 237403, (2006).

[103] Fabien Tran and Peter Blaha. "Accurate Band Gaps of Semiconductors and Insulators with a Semilocal Exchange-Correlation Potential". *Phys. Rev. Lett.*, **102** 226401, (2009).

[104] M. T. Yin and Marvin L. Cohen. "Theory of static structural properties, crystal stability, and phase transformations: Application to Si and Ge". *Phys. Rev. B*, **26** 5668–5687, (1982).

[105] Kerstin Hummer, Judith Harl, and Georg Kresse. "Heyd-Scuseria-Ernzerhof hybrid functional for calculating the lattice dynamics of semiconductors". *Phys. Rev. B*, **80** 115205, (2009).

[106] J. P. Perdew and Alex Zunger. "Self-interaction correction to density-functional approximations for many-electron systems". *Phys. Rev. B*, **23** 5048–5079, (1981).

[107] N. Troullier and José Luriaas Martins. "Efficient pseudopotentials for plane-wave calculations". *Phys. Rev. B*, **43** 1993–2006, (1991).

[108] Leonard Kleinman and D. M. Bylander. "Efficacious Form for Model Pseudopotentials". *Phys. Rev. Lett.*, **48** 1425–1428, (1982).

[109] John P. Perdew, Kieron Burke, and Matthias Ernzerhof. "Generalized Gradient Approximation Made Simple". *Phys. Rev. Lett.*, **77** 3865–3868, (1996).

[110] Axel D. Becke and Erin R. Johnson. "A simple effective potential for exchange". *The Journal of Chemical Physics*, **124**(22) 221101, (2006).

[111] A. D. Becke and M. R. Roussel. "Exchange holes in inhomogeneous systems: A coordinate-space model". *Phys. Rev. A*, **39** 3761–3767, (1989).

[112] David Koller, Fabien Tran, and Peter Blaha. "Improving the modified Becke-Johnson exchange potential". *Phys. Rev. B*, **85** 155109, (2012).

[113] John P. Perdew, Robert G. Parr, Mel Levy, and Jose L. Balduz. "Density-Functional Theory for Fractional Particle Number: Derivative Discontinuities of the Energy". *Phys. Rev. Lett.*, **49** 1691–1694, (1982).

[114] Jianmin Tao. "Explicit inclusion of paramagnetic current density in the exchange-correlation functionals of current-density functional theory". *Phys. Rev. B*, **71** 205107, (2005).

[115] Jianmin Tao and John P. Perdew. "Nonempirical Construction of Current-Density Functionals from Conventional Density-Functional Approximations". *Phys. Rev. Lett.*, **95** 196403, (2005).

[116] S. Pittalis, E. Räsänen, and E. K. U. Gross. "Gaussian approximations for the exchange-energy functional of current-carrying states: Applications to two-dimensional systems". *Phys. Rev. A*, **80** 032515, (2009).

[117] Mohsen Vafaee, Firoozeh Sami, Babak Shokri, Behnaz Buzari, and Hassan Sabzyan. "Precise description of single and double ionization of hydrogen molecule in intense laser pulses". *The Journal of Chemical Physics*, **137**(4) 044112, (2012).

[118] Michael Walter, Hannu Hkkinen, Lauri Lehtovaara, Martti Puska, Jussi Enkovaara, Carsten Rostgaard, and Jens Jrgen Mortensen. "Time-dependent density-functional theory in the projector augmented-wave method". *The Journal of Chemical Physics*, **128**(24) 244101, (2008).

[119] Jun-Ichi Iwata, Daisuke Takahashi, Atsushi Oshiyama, Taisuke Boku, Kenji Shiraishi, Susumu Okada, and Kazuhiro Yabana. "A massively-parallel electronic-structure calculations based on real-space density functional theory". *Journal of Computational Physics*, **229**(6) 2339 – 2363, (2010).

[120] Vladimir A. Goncharov. "Nonlinear optical response in solids from time-dependent density-functional theory simulations". *The Journal of Chemical Physics*, **139**(8) 084104, (2013).

[121] L. V. Keldysh. "Ionization in the field of a strong electromagnetic wave". *Sov. Phys. JETP*, **20**(5) 1307–1314, (1965).

[122] Otfried Madelung. "Semiconductors-basic data". (2012).

[123] V. U. Nazarov and G. Vignale. "Optics of Semiconductors from Meta-Generalized-Gradient-Approximation-Based Time-Dependent Density-Functional Theory". *Phys. Rev. Lett.*, **107** 216402, (2011).

[124] J. Paier, M. Marsman, K. Hummer, G. Kresse, I. C. Gerber, and J. G. Ángyán. "Screened hybrid density functionals applied to solids". *The Journal of Chemical Physics*, **124**(15) 154709, (2006).

[125] K. Yabana and G. F. Bertsch. "Introduction to Computational Methods in Many Body Physics edited by M. Bonitz and D. Semka". (2006).

[126] Edward D. Palik. "Handbook of optical constants of solids". (1985).

[127] D. E. Aspnes and A. A. Studna. "Dielectric functions and optical parameters of Si, Ge, GaP, GaAs, GaSb, InP, InAs, and InSb from 1.5 to 6.0 eV". *Phys. Rev. B*, **27** 985–1009, (1983).

[128] Kyung-Min Lee, Chul Min Kim, Shunsuke A. Sato, Tomohito Otobe, Yasushi Shinohara, Kazuhiro Yabana, and Tae Moon Jeong. "First-principles simulation of the optical response of bulk and thin-film -quartz irradiated with an ultrashort intense laser pulse". *Journal of Applied Physics*, **115**(5) 053519, (2014).

[129] S. A. Sato, K. Yabana, Y. Shinohara, T. Otobe, K.-M. Lee, and G. F. Bertsch. "Time-dependent density functional theory of high-intensity short-pulse laser irradiation on insulators". *Phys. Rev. B*, **92** 205413, (2015).

[130] Behnam Farid and R. W. Godby. "Cohesive energies of crystals". *Phys. Rev. B*, **43** 14248–14250, (1991).

[131] Charles Kittel. "Introduction to solid state physics". (2005).

[132] R. Merlin. "Generating coherent THz phonons with light pulses". *Solid State Communications*, **102**(2-3) 207 – 220, (1997).

[133] Alexander V. Mitrofanov, Aart J. Verhoef, Evgenii E. Serebryannikov, Julien Lumeau, Leonid Glebov, Aleksei M. Zheltikov, and Andrius Baltuška. "Optical Detection of Attosecond Ionization Induced by a Few-Cycle Laser Field in a Transparent Dielectric Material". *Phys. Rev. Lett.*, **106** 147401, (2011).

[134] A. Kaiser, B. Rethfeld, M. Vicanek, and G. Simon. "Microscopic processes in dielectrics under irradiation by subpicosecond laser pulses". *Phys. Rev. B*, **61** 11437–11450, (2000).

[135] B. Rethfeld. "Unified Model for the Free-Electron Avalanche in Laser-Irradiated Dielectrics". *Phys. Rev. Lett.*, **92** 187401, (2004).

[136] N. Medvedev and B. Rethfeld. "A comprehensive model for the ultrashort visible light irradiation of semiconductors". *Journal of Applied Physics*, **108**(10) 103112, (2010).

[137] B. Rethfeld, O. Brenk, N. Medvedev, H. Krutsch, and D. H. H. Hoffmann. "Interaction of dielectrics with femtosecond laser pulses: application of kinetic approach and multiple rate equation". *Applied Physics A*, **101**(1) 19–25, (2010).

[138] A. Oschlies, R. W. Godby, and R. J. Needs. "First-principles self-energy calculations of carrier-induced band-gap narrowing in silicon". *Phys. Rev. B*, **45** 13741–13744, (1992).

[139] Sergey V. Faleev, Mark van Schilfgaarde, Takao Kotani, Fran çois Léonard, and Michael P. Desjarlais. "Finite-temperature quasiparticle self-consistent $GW$ approximation". *Phys. Rev. B*, **74** 033101, (2006).

[140] D. Hulin, M. Combescot, J. Bok, A. Migus, J. Y. Vinet, and A. Antonetti. "Energy Transfer during Silicon Irradiation by Femtosecond Laser Pulse". *Phys. Rev. Lett.*, **52** 1998–2001, (1984).

[141] Pier Luigi Silvestrelli, Ali Alavi, Michele Parrinello, and Daan Frenkel. "*Ab initio* Molecular Dynamics Simulation of Laser Melting of Silicon". *Phys. Rev. Lett.*, **77** 3149–3152, (1996).

[142] V. Recoules, J. Clérouin, G. Zérah, P. M. Anglade, and S. Mazevet. "Effect of Intense Laser Irradiation on the Lattice Stability of Semiconductors and Metals". *Phys. Rev. Lett.*, **96** 055503, (2006).

[143] Lorin X. Benedict. "Dielectric function for a model of laser-excited GaAs". *Phys. Rev. B*, **63** 075202, (2001).

[144] J. A. Armstrong, N. Bloembergen, J. Ducuing, and P. S. Pershan. "Interactions between Light Waves in a Nonlinear Dielectric". *Phys. Rev.*, **127** 1918–1939, (1962).

[145] Ferenc Krausz and Mark I Stockman. "Attosecond metrology: from electron capture to future signal processing". *Nature Photonics*, **8**(3) 205–213, (2014).

[146] A. Sommer, E. M. Bothschafter, S. A. Sato, C. Jakubeit, T. Latka, O. Razskazovskaya, H. Fattahi, M. Jobst, W. Schweinberger, V. Shirvanyan, V. S. Yakovlev, R. Kienberger, K. Yabana, N. Karpowicz, M. Schultze, and F. Krausz. "Attosecond nonlinear polarization and energy transfer in dielectrics". *Submitted.*

[147] Annkatrin Sommer. "Ultrafast Strong Field Dynamics in Dielectrics". *Ph.D thesis*, (2015).

[148] F. DeMartini, C. H. Townes, T. K. Gustafson, and P. L. Kelley. "Self-Steepening of Light Pulses". *Phys. Rev.*, **164** 312–323, (1967).

[149] B. N. Chichkov, C. Momma, S. Nolte, F. von Alvensleben, and A. Tnnermann. "Femtosecond, picosecond and nanosecond laser ablation of solids". *Applied Physics A*, **63**(2) 109–115, (1996).

[150] B. C. Stuart, M. D. Feit, S. Herman, A. M. Rubenchik, B. W. Shore, and M. D. Perry. "Nanosecond-to-femtosecond laser-induced breakdown in dielectrics". *Phys. Rev. B*, **53** 1749–1761, (1996).

[151] X. Liu, D. Du, and G. Mourou. "Laser ablation and micromachining with ultrashort laser pulses". *Quantum Electronics, IEEE Journal of*, **33**(10) 1706–1716, (1997).

[152] M. Lenzner, J. Krüger, S. Sartania, Z. Cheng, Ch. Spielmann, G. Mourou, W. Kautek, and F. Krausz. "Femtosecond Optical Breakdown in Dielectrics". *Phys. Rev. Lett.*, **80** 4076–4079, (1998).

[153] M. Geissler, G. Tempea, A. Scrinzi, M. Schnürer, F. Krausz, and T. Brabec. "Light Propagation in Field-Ionizing Media: Extreme Nonlinear Optics". *Phys. Rev. Lett.*, **83** 2930–2933, (1999).

[154] M. Lenzner and F. Krausz and J. Krüger and W. Kautek. "Photoablation with sub-10 fs laser pulses". *Applied Surface Science*, **154-155** 11–16, (2000).

[155] L. Sudrie, A. Couairon, M. Franco, B. Lamouroux, B. Prade, S. Tzortzakis, and A. Mysyrowicz. "Femtosecond Laser-Induced Damage and Filamentary Propagation in Fused Silica". *Phys. Rev. Lett.*, **89** 186601, (2002).

[156] G. Doumy, F. Quéré, O. Gobert, M. Perdrix, Ph. Martin, P. Audebert, J. C. Gauthier, J.-P. Geindre, and T. Wittmann. "Complete characterization of a plasma mirror for the production of high-contrast ultraintense laser pulses". *Phys. Rev. E*, **69** 026402, (2004).

[157] S. Amoruso, G. Ausanio, R. Bruzzese, M. Vitiello, and X. Wang. "Femtosecond laser pulse irradiation of solid targets as a general route to nanoparticle formation in a vacuum". *Phys. Rev. B*, **71** 033406, (2005).

[158] B. Chimier, O. Utéza, N. Sanner, M. Sentis, T. Itina, P. Lassonde, F. Légaré, F. Vidal, and J. C. Kieffer. "Damage and ablation thresholds of fused-silica in femtosecond regime". *Phys. Rev. B*, **84** 094104, (2011).

[159] O. Utéza, N. Sanner, B. Chimier, A. Brocas, N. Varkentina, M. Sentis, P. Lassonde, F. Légaré, and J. C. Kieffer. "Control of material removal of fused silica with single pulses of few optical cycles to sub-picosecond duration". *Applied Physics A*, **105**(1) 131–141, (2011).

[160] An-Chun Tien, Sterling Backus, Henry Kapteyn, Margaret Murnane, and Gérard Mourou. "Short-Pulse Laser Damage in Transparent Materials as a Function of Pulse Duration". *Phys. Rev. Lett.*, **82** 3883–3886, (1999).

[161] Danny Perez and Laurent J. Lewis. "Molecular-dynamics study of ablation of solids under femtosecond laser pulses". *Phys. Rev. B*, **67** 184102, (2003).

[162] B. Rethfeld, K. Sokolowski-Tinten, D. von der Linde, and S. I. Anisimov. "Timescales in the response of materials to femtosecond laser excitation". *Applied Physics A*, **79**(4-6) 767–769, (2004).

[163] J. R. Peñano, P. Sprangle, B. Hafizi, W. Manheimer, and A. Zigler. "Transmission of intense femtosecond laser pulses into dielectrics". *Phys. Rev. E*, **72** 036412, (2005).

[164] B. H. Christensen and P. Balling. "Modeling ultrashort-pulse laser ablation of dielectric materials". *Phys. Rev. B*, **79** 155424, (2009).

[165] Nils Brouwer and Bärbel Rethfeld. "Excitation and relaxation dynamics in dielectrics irradiated by an intense ultrashort laser pulse". *J. Opt. Soc. Am. B*, **31**(11) C28–C35, (2014).

[166] T Otobe, K Yabana, and J-I Iwata. "First-principles calculation of the electron dynamics in crystalline $SiO_2$". *Journal of Physics: Condensed Matter*, **21**(6) 064224, (2009).

[167] S. A. Sato, K. Yabana, Y. Shinohara, T. Otobe, and G. F. Bertsch. "Numerical pump-probe experiments of laser-excited silicon in nonequilibrium phase". *Phys. Rev. B*, **89** 064304, (2014).

[168] Georg Wachter, Christoph Lemell, Joachim Burgdörfer, Shunsuke A. Sato, Xiao-Min Tong, and Kazuhiro Yabana. "*Ab Initio* Simulation of Electrical Currents Induced by Ultrafast Laser Excitation of Dielectric Materials". *Phys. Rev. Lett.*, **113** 087401, (2014).

[169] S. D. Brorson, J. G. Fujimoto, and E. P. Ippen. "Femtosecond electronic heat-transport dynamics in thin gold films". *Phys. Rev. Lett.*, **59** 1962–1965, (1987).

[170] W. S. Fann, R. Storz, H. W. K. Tom, and J. Bokor. "Electron thermalization in gold". *Phys. Rev. B*, **46** 13592–13595, (1992).

[171] S. A. Sato, Y. Shinohara, T. Otobe, and K. Yabana. "Dielectric response of laser-excited silicon at finite electron temperature". *Phys. Rev. B*, **90** 174303, (2014).

[172] D. G. Hicks, T. R. Boehly, J. H. Eggert, J. E. Miller, P. M. Celliers, and G. W. Collins. "Dissociation of Liquid Silica at High Pressures and Temperatures". *Phys. Rev. Lett.*, **97** 025502, (2006).

[173] Patrick Lorazo, Laurent J. Lewis, and Michel Meunier. "Short-Pulse Laser Ablation of Solids: From Phase Explosion to Fragmentation". *Phys. Rev. Lett.*, **91** 225502, (2003).

[174] Takayuki Kumada, Hiroshi Akagi, Ryuji Itakura, Tomohito Otobe, and Atsushi Yokoyama. "Femtosecond laser ablation dynamics of fused silica extracted from oscillation of time-resolved reflectivity". *Journal of Applied Physics*, **115**(10) 103504, (2014).

[175] Shizhen Xu, Jianrong Qiu, Tianqing Jia, Chengbin Li, Haiyi Sun, and Zhizhan Xu. "Femtosecond laser ablation of crystals SiO2 and YAG". *Optics Communications*, **274**(1) 163 – 166, (2007).

[176] T. Otobe. "First-principle description for the high-harmonic generation in a diamond by intense short laser pulse". *Journal of Applied Physics*, **111**(9) 093112, (2012).

[177] P. A. Loukakos, M. Lisowski, G. Bihlmayer, S. Blügel, M. Wolf, and U. Bovensiepen. "Dynamics of the Self-Energy of the Gd(0001) Surface State Probed by Femtosecond Photoemission Spectroscopy". *Phys. Rev. Lett.*, **98** 097401, (2007).

[178] Lucio Rota, Paolo Lugli, Thomas Elsaesser, and Jagdeep Shah. "Ultrafast thermalization of photoexcited carriers in polar semiconductors". *Phys. Rev. B*, **47** 4226–4237, (1993).

[179] Alfred Leitenstorfer, Cornelius Fürst, Alfred Laubereau, Wolfgang Kaiser, Günther Tränkle, and Günter Weimann. "Femtosecond Carrier Dynamics in GaAs Far from Equilibrium". *Phys. Rev. Lett.*, **76** 1545–1548, (1996).

[180] E. Goulielmakis, V. S. Yakovlev, A. L. Cavalieri, M. Uiberacker, V. Pervak, A. Apolonski, R. Kienberger, U. Kleineberg, and F. Krausz. "Attosecond Control and Measurement: Lightwave Electronics". *Science*, **317**(5839) 769–775, (2007).

[181] D. Sangalli and A. Marini. "Ultra-fast carriers relaxation in bulk silicon following photo-excitation with a short and polarized laser pulse". *EPL (Europhysics Letters)*, **110**(4) 47004, (2015).

# Publications

A part of the results discussed in this work is based on publications listed below:

**Numerical aspects (Chapter 3)**

- Shunsuke A. Sato, Kazuhiro Yabana
  "Maxwell + TDDFT multi-scale simulation for laser-matter interaction"
  J. Adv. Simulat. Sci. Eng. Vol. 1, No. 1, 98-110.

**Electron dynamics in crystalline solids (Chapter 4)**

- Shunsuke A. Sato, Yasutaka Taniguchi, Yasushi Shinohara, Kazuhiro Yabana
  "Nonlinear electronic excitations in crystalline solids using meta-generalized gradient approximation and hybrid functional in time-dependent density functional theory"
  J. Chem. Phys. 143, 224116 (2015).

**Optical properties of highly laser-excited solids (Chapter 5)**

- S. A. Sato, K. Yabana, Y. Shinohara, T. Otobe, G. F. Bertsch
  "Numerical pump-probe experiments of laser-excited silicon in nonequilibrium phase"
  Phys. Rev. B 89, 064304 (2014).

- S. A. Sato, Y. Shinohara, T. Otobe, K. Yabana
  "Dielectric response of laser-excited silicon at finite electron temperature"
  Phys. Rev. B 90, 174303 (2014).

**Femtosecond-laser-induced damage phenomena (Chapter 7)**

- S. A. Sato, K. Yabana, Y. Shinohara, T. Otobe, K. M. Lee, G. F. Bertsch
  "Time-dependent density functional theory of high-intensity, short-pulse laser irradiation on insulators"
  Phys. Rev. B 92, 205413 (2015).

**Other topics**

- T. Otobe, Y. Shinohara, S. A. Sato, K. Yabana
  "Femtosecond time-resolved dynamical Franz-Keldysh effect"
  Phys. Rev. B. in press.

- Georg Wachter, Shunsuke A. Sato, Isabella Floss, Christoph Lemell, Xiao-Min Tong, Kazuhiro Yabana, Joachim Burgdörfer
  "Controlling ultrafast currents by the non-linear photogalvanic effect"
  New J. Phys. 17, 123026 (2015).

- Georg Wachter, Stefan Nagele, Shunsuke A. Sato, Renate Pazourek, Michael Wais, Christoph Lemell, Xiao-Min Tong, Kazuhiro Yabana, Joachim Burgdörfer
  "Protocol for observing molecular dipole excitations by attosecond self-streaking"
  Phys. Rev. A 92, 061403(R) (2015).

- Xiao-Min Tong, Georg Wachter, Shunsuke A. Sato, Christoph Lemell, Kazuhiro Yabana, and Joachim Burgdörfer
  "Application of norm-conserving pseudopotentials to intense laser-matter interactions"
  Phys. Rev. A 92, 043422 (2015).

- Martin Schultze, Krupa Ramasesha, C. D. Pemmaraju, S. A. Sato, D. Whitmore, A. Gandman, James S. Prell, L. J. Borja, D. Prendergast, K. Yabana, Daniel M. Neumark, and Stephen R. Leone
  "Attosecond band-gap dynamics in silicon"
  Science 346, 1348 (2014).

- Shunsuke A. Sato, Kazuhiro Yabana
  "Efficient basis expansion for describing linear and nonlinear electron dynamics in crystalline solids"
  Phys. Rev. B 89, 224305 (2014).

- Georg Wachter, Christoph Lemell, Joachim Burgdörfer, Shunsuke A. Sato, Xiao-Min Tong, Kazuhiro Yabana
  "Ab-initio simulation of electrical currents induced by ultrafast laser excitation of dielectric materials"
  Phys. Rev. Lett. 113, 087401 (2014).

- Kyung-Min Lee, Chul Min Kim, Shunsuke A. Sato, Tomohito Otobe, Yasushi Shinohara, Kazuhiro Yabana, Tae Moon Jeong
  "First-principles simulation of the optical response of bulk and thin-film $\alpha$-quartz irradiated with an ultrashort intense laser pulse"
  J. Appl. Phys. 115, 053519 (2014).

- Y. Shinohara, S. A. Sato, K. Yabana, J.-I. Iwata, T. Otobe, G. F. Bertsch
  "Nonadiabatic generation of cohrent phonons"
  J. Chem. Phys. 137, 22A527 (2012).

# Acknowledgement

I have been supported by many people for completing my Ph.D. If it were not for their support, I could not have done this work. Here I'd like to express my appreciation to them.

First of all, I'd like to thank my Ph.D. supervisor Prof. Kazuhiro Yabana for all his help and advice. Discussion with him is always helpful for me. I have learned a lot of things from the discussion. He has also supported me in various aspects. Thanks to his support, I have had many experiences that would be important and valuable to spend my life in scientific fields in the future. I'd like to thank again him for taking time for me despite being ultra-busy.

I would also like to thank Prof. George Bertsch for fruitful discussion. His suggestions based on his extensive knowledge and deep insight are always significant. I'm honored to work with such a talented expert.

I am grateful to Dr. Yasushi Shinohara for his advice as well as valuable discussion. He gave me a lot of advice on various things, such as trip, computers, daily life as well as science. Furthermore, his careful consideration in scientific discussion often helped me with proceeding with science.

I am also grateful to Dr. Tomohito Otobe and Dr. Yasutaka Taniguchi for helpful advice and useful discussion as colleagues.

I would like to express my appreciation to Prof. Joachim Burgdörfer, Prof. Christoph Lemell, Dr. Georg Wachter, Isabella Floss, and Wolfgang Moser from Vienna and Prof. Xiao-Min Tong from Tsukuba for valuable collaborations. They are experts in "light-matter interactions". Discussion with them is fruitful and educative for me. It is a great honor to work with such an experienced team. Furthermore, I would like to thank them for taking care of my stay in Vienna. I have spent meaningful time and had an amazing experience in Vienna.

I would also like to express my appreciation to Dr. Martin Schultze and Dr. Annkatrin Sommer from Munich for valuable collaboration. I am really excited their fresh experimental results, *real-time observation of nonlinear polarization*, and am grateful to them for fruitful discussion and valuable suggestions. Chapter 6 would be impossible without them. I am also grateful to them for providing the experimental data in Chap. 6.

I would like to thank very much the Nuclear Theory Group of the University of Tsukuba. Since I joined the group in April 2011, I have had a lot of valuable experiences. It was a great pleasure to work in this group. Especially, I am grateful to Prof. Takashi Nakatsukasa, Dr. Yukio Hashimoto, and Dr. Kouhei Washiyama for their valuable advice and kind support. Although I am not a *Nuclear Physicist*, I have enjoyed their researches and learned insight of physics of quantum many-body systems. I am also grateful to Dr. Kazuyuki Sekizawa and Dr. Kai Wen who are cheerful and kind colleagues. Thanks to them, I have enjoyed these days. Furthermore, I have learned their experience of working abroad after getting Ph.D. The advice based on their experiences is really helpful to consider my future career.

Last but not least, I would like to express my deepest appreciation to my parents and grandparents for their warm support.

<div align="right">Shunsuke A. Sato</div>